IRAQI JOURNAL OF APPLIED PHYSICS

The *Iraqi Journal of Applied Physics (IJAP)* is a peer reviewed journal of high quality devoted to the publication of original research papers from applied physics and their broad range of applications. IJAP publishes quality original research papers, comprehensive review articles, survey articles, book reviews, dissertation abstracts in physics and its applications in the broadest sense. It is intended that the journal may act as an interdisciplinary forum for Physics and its applications. Innovative applications and material that brings together diverse areas of Physics are particularly welcome. Review articles in selected areas are published from time to time. It aims to disseminate knowledge; provide a learned reference in the field; and establish channels of communication between academic and research experts, policy makers and executives in industry, commerce and investment institutions. IJAP is a quarterly specialized periodical dedicated to publishing original papers, letters and reviews in: Applied & Nonlinear Optics, Applied Mechanics & Thermodynamics, Digital & Optical Communications, Electronic Materials & Devices, Laser Physics & Applications, Plasma Physics & Applications, Quantum Physics & Spectroscopy, Semiconductors & Optoelectronics, Solid State Physics & Applications, Alternative & Renewable Energy, and Environmental Science & Technology.

ISSN (Print): 1813-2065, ISSN (Online): 2309-1673

Editorial Office:
P. O. Box 88052, Baghdad 12631, IRAQ
Website: www.iraqiphysicsjournal.com
Emails: info@iraqiphysicsjournal.com, editor_ijap@yahoo.co.uk, ijap.editor@gmail.com,

SPONSORED AND PUBLISHED BY
AMERICAN QUALITY FOR SCIENTIFIC PUBLISHING INC.
1479 South De Gaulle Ct, Aurora, CO 80018, United States

IRAQI JOURNAL OF APPLIED PHYSICS

ISSN (Print): 1813-2065, ISSN (Online): 2309-1673

INSTRUCTIONS TO AUTHORS

CONTRIBUTIONS

Contributions to be published in this journal should be original research works, i.e., those not already published or submitted for publication elsewhere, individual papers or letters to editor.
Manuscripts should be submitted to the editor at the mailing address:
Iraqi Journal of Applied Physics, Editorial Board, P. O. Box 88052, Baghdad 12311, IRAQ
Website: www.iraqiphysicsjournal.com
Email: info@iraqiphysicsjournal.com, editor_ijap@yahoo.co.uk, ijap.editor@gmail.com

MANUSCRIPTS

Two hard copies with soft Word copy on a CD or DVD should be submitted to Editor in the following configuration:

- **One-column** Double-spaced one-side A4 size with 2.5 cm margins of all sides
- Times New Roman font (16pt bold for title, 14pt bold for names, 12pt bold for headings, 12pt regular for text)
- Manuscripts presented in English only are accepted.
- English abstract not exceed 150 words
- 4 keywords (at least) should be maintained on (PACS preferred)
- Author(s) should express all quantities in SI units
- Equations should be written in equation form (*italic* and symbolic) NOT in plain text
- Tables and Figures should be separated from text and placed in new pages after the references
- Charts should be indicated by the software used for generating them (e.g., Excel, MATLAB, Grapher, etc.)
- Figures and diagrams can be submitted in original colored forms for assessment and they will be returned to authors after provide printable copies
- Only original or high-resolution scanner photos are accepted
- For electronic submission, articles should be formatted with MS-Word software.

AUTHOR NAMES AND AFFILIATIONS

It is IJAP policy that all those who have participated significantly in the technical aspects of a paper be recognized as co-authors or cited in the acknowledgments. In the case of a paper with more than one author, correspondence concerning the paper will be sent to the first author unless staff is advised otherwise.
Author name should consist of first name, middle initial, last name. The author affiliation should consist of the following, as applicable, in the order noted:
- Company or college (with department name or company division), Postal address, City, Governorate or State, zip code, Country name, contacting telephone number, and e-mail

REFERENCES

The references should be brought at the end of the article, and numbered in the order of their appearance in the paper. The reference list should be cited in accordance with the following examples:
[1] X. Ning, R. Benford and M.R. Lovell, "On the Sliding Friction Characteristics of Unidirectional Continuous FRP Composites", *J. Tribol. Func. Mater.*, 124(1) (2002) 5-13.
[2] M. Barnes, "Stresses in Solenoids", *J. Appl. Phys.*, 48(5) (2001) 2000–2008.
[3] J. Jones, **"Contact Mechanics"**, Cambridge University Press (Cambridge, UK) (2000), Ch.6, p.56.
[4] Y. Lee, S.A. Korpela and R. Horne, "Structure of Multi-Cellular Natural Convection in a Tall Vertical Annulus", Proceedings of 7th International Heat Transfer Conference, U. Grigul et al., eds., Hemisphere (Washington DC), 2 (1982) 221–226.
[5] M. Hashish, "Waterjet Technology Development", High Pressure Technology, PVP-Vol. 406 (2000) 135-140.
[6] D.W. Watson, "Thermodynamic Analysis", ASME Paper No. 97-GT-288 (1997).
[7] C.Y. Tung, "Evaporative Heat Transfer in the Contact Line of a Mixture", Ph.D. thesis, Rensselaer Polytechnic Institute, Troy, NY (1982).

PROOFS

Authors will receive proofs of papers and are requested to return one corrected copy as a WORD file on a compact disc (CD) or by email. New materials inserted in the original text without Editor's permission may cause rejection of paper unless the handling editor is informed.

COPYRIGHT FORM

Author(s) will be asked to sign the IJAP Copyright Form and hence transfer copyrights of the article to the Journal soon after acceptance of it. This will ensure the widest possible dissemination of information.

OFFPRINTS

Authors will receive electronic offprint free of charge and any additional reprints can be ordered.

SUBSCRIPTION AND ORDERS

Annual fees (4 issues per year) of subscription are:
50 US$ for individuals inside Iraq; **200** US$ for institutions inside Iraq;
100 US$ for individuals abroad; **300** US$ for institutions abroad.

IRAQI JOURNAL OF APPLIED PHYSICS
Volume 19, Issue 2, April-June 2023, 3-8

Proceedings of the 3rd International Scientific Conference and 5th Scientific Conference, organized by College of Science, University of Tikrit, Tikrit, Iraq (28-29 December 2022)

Physical Characterization and Antibacterial Activity Evaluation of Nanoparticles Manufactured from Zinc Plate by Pulsed Laser Ablation

Sahar N. Rashid[1]
Awatif S. Jasim[1]
Kadhim A. Aadim[2]
Marwa A. Alwan[1]

[1] *Department of Physics, College of Science, University of Tikrit, Tikrit, IRAQ*
[2] *Department of Physics, College of Science, University of Baghdad, Baghdad, IRAQ*

One of the physical methods for manufacturing nanoparticles that adopts a top-down approach is the laser ablation method, which is characterized by ease, speed, and low cost. In this work, we resorted to using this method to fabricate nanoparticles from zinc by ablation with Q-switched Nd:YAG laser in ethanol, with the repetition rate of pulses (6 Hz), wavelength (355 nm), and the energy (500 mJ), to obtain five colloidal samples where we applied five different numbers of pulses. Then characterized the resulting particles by physical analysis using UV-Vis, XRD, FE-SEM, and EDX techniques. The results showed both zinc and zinc oxide were formed with nanoscale sizes, where the average size was about (34 nm), and the energy gap of nano-zinc oxide increased with the increase in the number of pulses. It was also found that the prepared nanoparticles have good activity in inhibiting the growth of Staphylococcus aureus bacteria isolated from the oral cavity.

Keywords: Zinc oxide; Nanoparticles; Plasmon resonance; Laser ablation; Antibacterial activity
Received: 13 October 2022; **Revised:** 01 November 2022; **Accepted:** 04 November 2022

1. Introduction

Nanoparticles (NPs) can be synthesized in a myriad of ways, including an organometallic precursor method, solvothermal and hydrothermal methods, sol–gel methods, electrochemical reduction, chemical reduction, bio-mechanochemical, and physical vapor deposition. In general, most of these conventional techniques are complex to perform, require expensive costs, and can have a negative impact on the environment, with limited control of size uniformity and particle size [1,2]. It is clear from the studies conducted that ablation of solids in solution using pulsed laser is a flexible and effective technique for manufacturing high-purity NPs from different materials [1-5] without using any surfactant and counter-ion [4], and without surface contamination by residual anions, as well as without the need for reducing agents or catalysts [1]. Several reports in the literature have also shown that this technique can be adapted in such a way that the resulting particle size, concentration, and shape can be controlled accurately and efficiently [6-9]. It uses a short pulse to ablate NPs from a bulk target. This material moves in the form of a plasma plume at the ablation environment, where it intensify and redistributes to produce NPs [6]. Metal and metal oxide NPs have attracted significant attention recently, because of the wide applications they have in various fields [10-13]. Among these NPs both of ZnNPs and ZnO NPs were very attractive due to their novel optical properties such as the tenability of plasmonic resonance [14-19]. *Staphylococcus aureus* (*S. aureus*) is the essential causative factor of many infections. The antibiotics prevalent usage causes an increase in bacterial resistance and mutations. So, a high *S. aureus* resistance to antibiotics is observed among the patients [20-22]. That is the necessary reason to improve new generations of antibiotics to put down microbial infections. In this state, nanotechnology can backing the medical industry [20]. Previous literature reports recorded that, in addition to the wide applications of NPs fabricated from Zn, they have an antibacterial activity that lays them to be a successful alternative to antibiotics [10,20]. The antibacterial activity of NPs is proportional to the surface area and size, where the smaller particles show greater antibacterial activity. The efficacy of the smaller size particles is due to their high surface area to volume ratio, this feature allows for effective bonding with the bacterial surface. Surface plasmon resonance (SPR) is formed by NPs' lower intrinsic loss of plasmonic energy at visible frequencies [23-25]. Currently, manufacturing NPs with laser ablation technique has a highly empirical approach. Controlling the morphology, size, structure, and aggregation of NPs by laser energy, wavelength, pulses, and laser ablation media are some advantages of laser ablation technique [6]. In the current study, NPs were prepared from Zn target using the laser ablation method where we have

demonstrated the effect of laser pulses in NPs prepared, and then they were characterized by physical techniques and evaluation of their antibacterial activity.

2. Experimental Part

A high purity Zn plate with dimensions (1 cm, 1 cm, and 2 mm) was irradiated using Q-switched Nd: YAG laser in (5 mL) of absolute ethanol with (99.99%) of purity to ablate NPs from target surface. The high of liquid above the target was 5 cm, repetition rate of pulses was (6 Hz), the pulse duration (9 ns), wavelength (355 nm), and the energy (500 mJ). We obtained five colloidal samples where we applied five different number of pulses (500, 600, 700, 800, and 900 pulse) where the number of pulses was experimentally selected depending on the response of the solution to the laser effect and the start of color variation. The schematic illustration of the experimental set-up of laser ablation method is shown in Fig. (1).

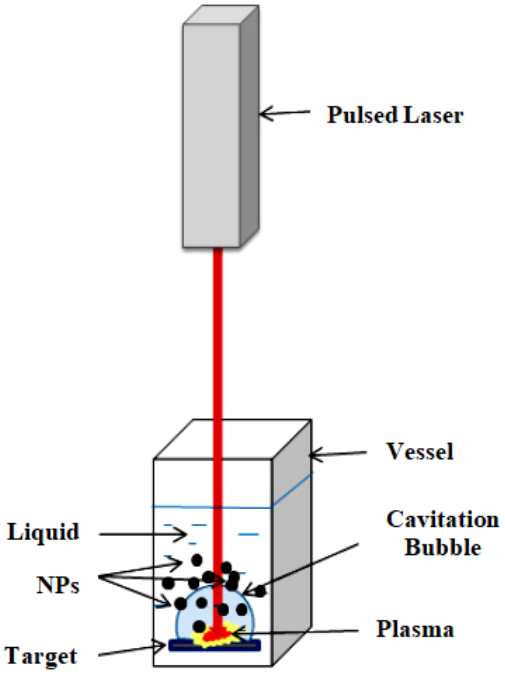

Fig. (1) Schematic illustration of the experimental set-up of laser ablation method

The prepared samples were characterized using diagnostic techniques. Double beam UV-Vis spectrophotometer device was utilized to investigate the optical properties of prepared NPs. X-ray diffraction (XRD) was utilized to diagnose the crystalline nature of NPs, the diffraction pattern at a range of angles 20°-80° represents (2θ), for target with wavelength of 1.5418 Å, voltage of 35kV and current of 30mA. Field-emission scanning electron microscopy (FESEM) was utilized to diagnose the structure properties, morphology, shape and size of NPs. FESEM system used has enabled the energy-dispersive x-ray (EDX) spectroscopy to know the type of chemical elements present in the prepared samples. The structural analyses (XRD and FESEM) were doing to the sample which were prepared at the highest number of pulses, such was determined based on the fact that it gave the best biological activity in this study.

To evaluate its antibacterial activity, this was done by testing its effectiveness against a Gram-positive bacterial species, which is *S. aureus* which was isolated and diagnosed by biologists, so that the prepared NPs were applied directly on them via well diffusion method was used, the bacterial suspension was spread on Muller Hinton agar medium in Petri dish using the swab and then left for (5 min), then (6 holes) were made in the dish, one of these holes is considered the control in which the liquid was placed, and all the remaining holes are for the solutions containing (50 µL) of the prepared NPs were placed for each number of laser pulses, it was placed in the incubator for (24 hours) at a temperature of (37 °C). NPs activity was determined by measuring the diameter of the inhibition zone.

Then comparing this activity with the activity of (15) types of commonly used antibiotics, which are each of Amikacin (AK), Amoxicillin (AX), Ampicillin (AM), Azithromycin (AZM), Cefotaxime (CTX), Cefixime (CFM), Ciprofloxacin (CIP), Erythromycin (E), Gentamicin (CN), Imipenem (IPE), Levofloxacin (LEV), Meropenem (MEM), Nitrofurantoin (F), Streptomycin (S), and Trimethoprim/Sulfamethoxazole (Cotrimoxazole) (TS). The concentrations and the group to which the antibiotic belongs are shown in table (1).

Table (1) Antibiotic disk used in this work

No.	Antibiotic	Symbol	Concentration µg/disk	Group to which the Antibiotic belongs
1	Amikacin	AK	30	Aminoglycosides
2	Amoxicillin	AX	25	Penicillin
3	Ampicillin	AM	10	Penicillin
4	Azithromycin	AZM	15	Macrolide
5	Cefotaxime	CTX	30	Cephalosporin 3rd generation
6	Cefixime	CFM	5	Cephalosporin 3rd generation
7	Ciprofloxacin	CIP	5	Fluoroquinolones
8	Erythromycin	E	15	Macrolide
9	Gentamicin	CN	30	Aminoglycosides
10	Imipenem	IPE	10	Carbapenem
11	Levofloxacin	LEV	5	Fluoroquinolones
12	Meropenem	MEM	10	Carbapenem
13	Nitrofurantoin	F	100	Fluoroquinolone
14	Streptomycin	S	30	Aminoglycosides
15	Trimethoprim Sulfamethoxazole (Cotrimoxazole)	TS	25	Sulfonamides

3. Results and Discussion

The XRD pattern resulting from the analysis of the colloidal solution produced by the ablation of the zinc target in the liquid which was prepared with the highest number of laser pulses (900 Pulse) showed that, in addition to the formation of Zn NPs, ZnO NPs were formed. Where the proportion of Zn NPs is (57%) and the proportion of ZnO NPs is (43%) and the crystal structure of the resulted NPs is hexagonal as shown in Fig. (2). The fitted XRD pattern of Zn

 ISSN 1813-2065 (print) 2309-1673 (online)

NPs and ZnO NPs were compared to (COD Card Number [96-901-1600]) and (COD Card Number [96-101-1260]) the standard pattern, respectively. The exposure of the metal to the high temperature resulting from the laser leads to the spread of heat to the area adjacent to the area of direct impact and oxidation of the affected metal area, and this occurs as a result of chemical changes to the surface of the metal, where a rapid increase in the oxygen content occurs, as stated in [26].

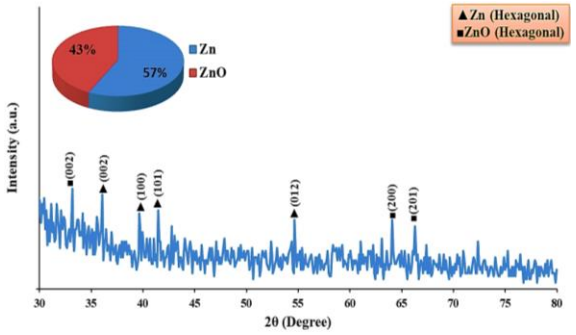

Fig. (2) XRD pattern of the sample prepared in this work

Some previous literature confirmed that the nanoparticles of oxides resulted from the metal atoms interaction with radicals or atoms of oxygen during dissolution in the liquid depending on the partial pressure of oxygen and temperature, as in [27]. The average size of prepared NPs (D) was calculated and its value was about (41 nm), according to Shearer's equation [27]:

$$D = \frac{K\lambda}{\beta Cos\theta} \qquad (1)$$

where K is shape factor constant and its value (0.9), λ is the X-ray wavelength, β is the full width at half maximum (FWHM) of the X-ray peak, and the angle θ denotes the reference peak width which represent the diffraction angle.

Figure (3), which represents the FE-SEM analysis of the prepared particles, shows that they have nanospherical shapes. This figure represents an image on the two scales (200 and 500 nm) of the manufactured samples at the number of pulses (900 pulse) and it indicated that the average distribution rate of each manufactured NPs was about (34 nm). The sample prepared with this number of pulses was chosen because it produced the highest concentration of the prepared NPs and produced the highest and most broad peak, which represents the surface plasmon resonance, it also gave a high inhibition of bacteria as shown by the results. The sizes determined by FE-SEM were smaller than that of XRD, where XRD measures the grains size into the sample through penetrate inside a sample in addition to the fact the XRD measuring, is the consequence of the prevalent levels of higher intensity without the residual and this else has an influence on the value of the size.

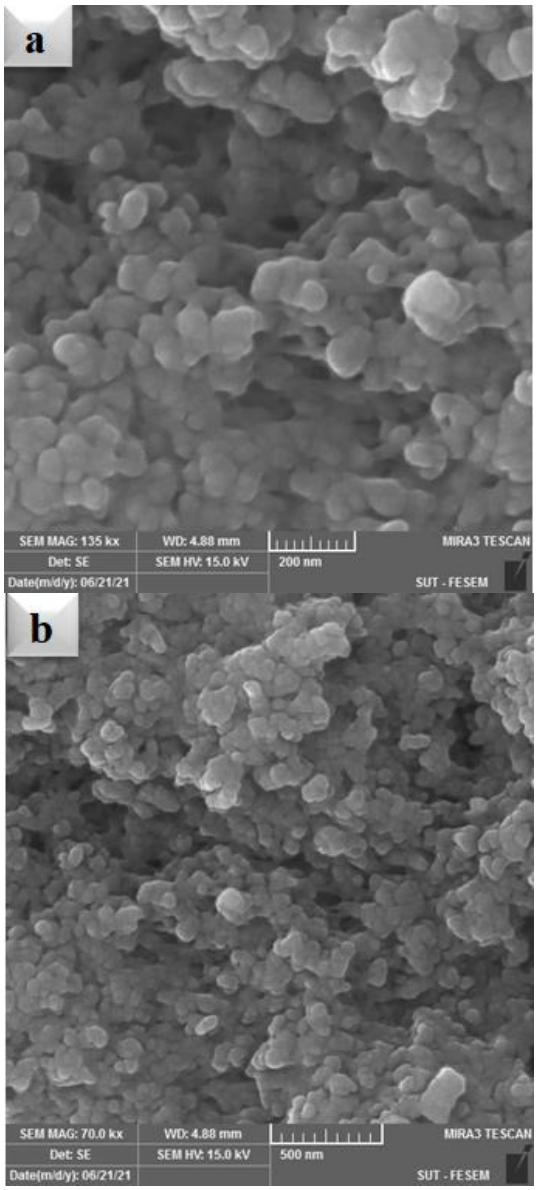

Fig. (3) FESEM image with scales (a) 200 nm, and (b) 500 nm

EDX analysis is suitable for chemical tests of the primer residual particles which is represents in Fig. (4). The values calculated by the EDX analysis are not absolute measures of element mass, but rather relative measures of atomic percent of the element. The reason of the gold (Au) element appearance in the results of the analysis is that the surface that is used for the analysis process must be flat, free of contamination, so, it is coated with gold. The reason for the decrease in the percentages of the prepared metal NPs is the increase in the percentage of oxygen, which may be the result of the high number of laser pulses that led to the oxidation of these particles, as shown in the results of XRD.

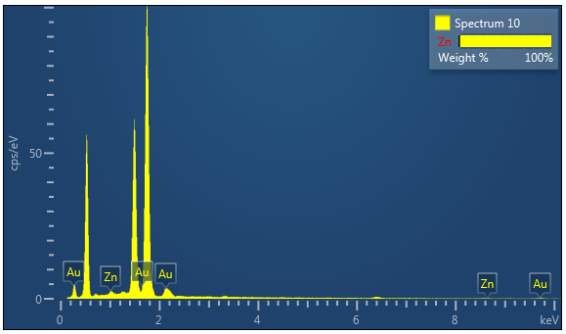

Fig. (4) Elemental analysis of the sample prepared in this work

The first visible evidence of the formation of NPs is the color change of colloidal solutions of Zn, which were colorless and then turned to yellowish-brown color and its gradations according to the number of pulses used to form the nanoscale particles. After obtaining these solutions, their optical description was doing using analysis of UV-visible spectrophotometer. It was observed from Fig. (5) that the maximum absorption ranged between (295-297nm). Increasing the pulses caused a broadening and uniformity of absorption peaks width, and a higher SPR peak with increasing pulses number is caused of a more efficient NPs redistribution due to the longer exposure time and effective electrical accumulation around the NPs, as in ref. [27-29].

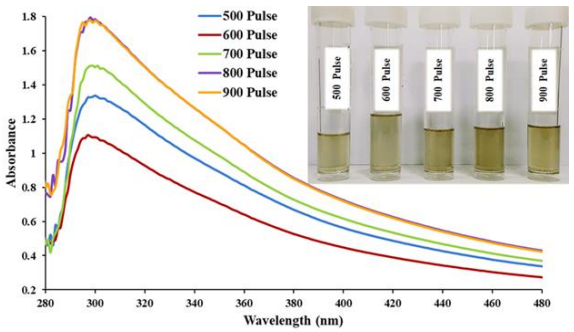

Fig. (5) UV-visible absorption spectra and prepared colloidal solutions

Figure (6) shows the transmittance spectra of the NPs manufactured by ablated Zn target. It shows an opposite behavior to the absorbance spectra, where we find that its values are directly proportional to the wavelength, and the laser pulses increase in the preparation caused a gradual decrease of their values, as the increase in the ablation percentage caused an increase of the energy-absorbing particles number.

Figure (7) represents the NPs absorption coefficient (α) curves calculated as in equation (2) as a function of the photon energy (hυ), where h represents Planck's constant and υ is the photon frequency. It was found that the values of these curves, which represent the absorption coefficient through a sample whose thickness (t) rises with the height of the photon energy, that is, they are similar to the absorption (A) curves. The highest value of the absorption coefficient was when preparing with a higher number of laser pulses [30-32]

$$\alpha = 2.303\frac{A}{t} \qquad (2)$$

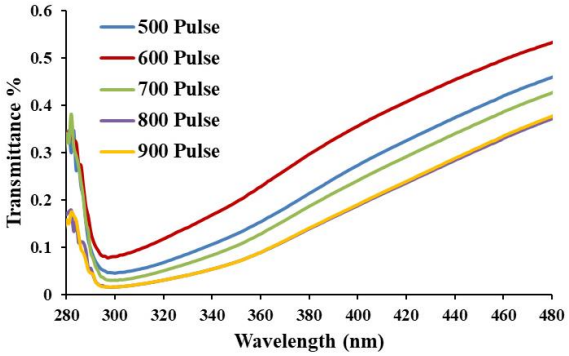

Fig. (6) UV-visible transmission spectra

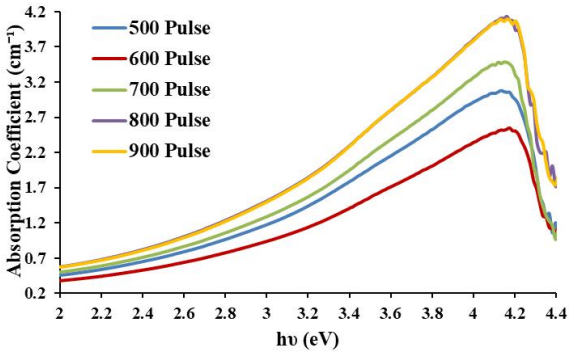

Fig. (7) Variation of absorption coefficient of ZnO NPs with photon energy for different numbers of pulses

XRD pattern analysis recorded the formation of ZnO NPs besides the Zn NPs themselves, so there was a need to determine the energy gap (E_g), as in Eq. (3). Figure (8) represents $(\alpha h\upsilon)^2$ as a function of the photon energy to find the energy gap of ZnO NPs in the prepared samples, and from it we find that the energy gap values range between 3.15 and 3.35 eV and that the increase of the pulses number led to higher energy gap values. Whereas, the increase in the energy-absorbing nanoparticles, which led to a higher absorbance, led to an increase in the energy gap values [17]

$$\alpha h\upsilon = B(h\upsilon - E_g)^{\frac{1}{2}} \qquad (3)$$

where B is a constant that depends on the type of material.

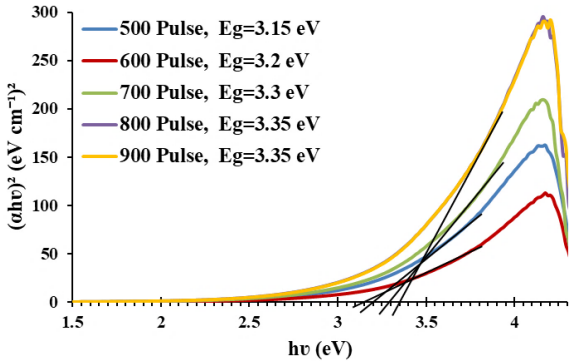

Fig. (8) Determination of energy band gap of ZnO NPs for different numbers of pulses

 ISSN 1813-2065 (print) 2309-1673 (online)

The results showed that NPs fabricated from ablated Zn target have significant inhibiting activity on *S. aureus* bacteria and at all prepared samples as in Fig. (9). One of the mechanisms maybe caused by NPs interaction with the cell wall of *S. aureus* and the simultaneous penetration of the metal and metal oxide ions into *S. aureus* cells. Where NPs antibacterial activity depends on the electrostatically attraction of the bacterial cell surfaces negative charge and NPs positive charge. NPs cause mitochondrial and DNA damage, and then the cell death. The extreme of reactive oxygen species (ROS) production by NPs causes damage of DNA, thus induced necrosis and apoptosis. *S. aureus* is sensitive to the fabricated NPs and resistant to the used antibiotics as shown in Fig. (10). This can be because of increased resistance of bacteria proven by antibiotic sensitivity experience. The behavior against the antibiotics requires the use of metal NPs and metal oxides NPs as alternatives.

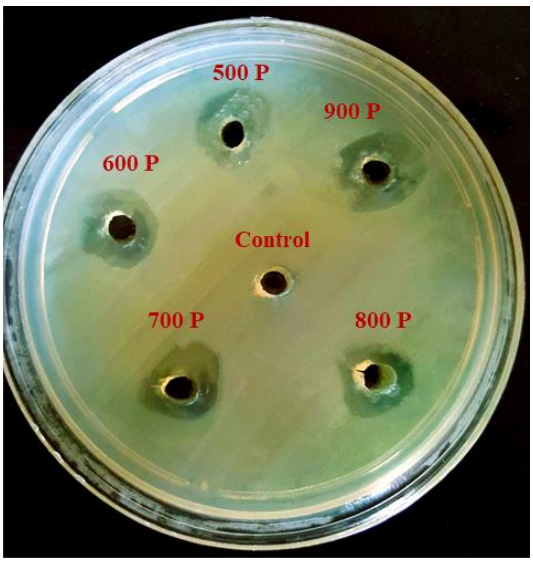

Fig. (9) Antibacterial activity of ZnO NPs

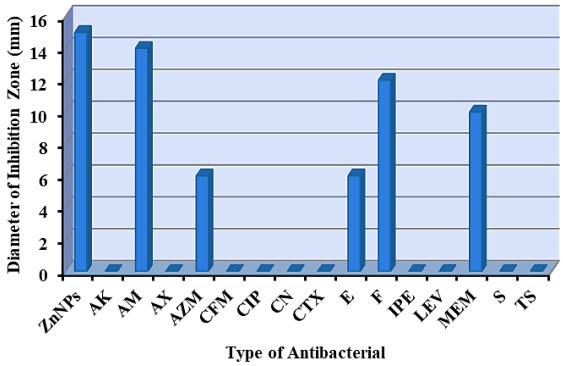

Fig. (10) Comparison of antibacterial activity of ZnO NPs versus antibiotics

4. Conclusion

In a summary of this work, it was found that the laser ablation technique is characterized by its ease, speed, and low cost, in addition to its production of NPs of purity. The particles produced in this way from the ablation of the zinc target were of nanoscale, hexagonal structure and nanospherical as described by the XRD and SEM techniques. It was also optical analyzed by UV-Vis spectrophotometer to find its absorption and transmittance spectra and its absorption coefficient curves as well as to calculate the energy gap of ZnO NPs that were formed beside to Zn NPs. It was found from the absorption spectrum that the intensity of the absorption of the resulting particles increases with the increase in the number of laser pulses used in the preparation of the samples, as these peaks represent the surface plasmon resonance of nanoparticles, and the increase in intensity and width of the peak shows the increase in the concentration of the resulting particles with the increase in the number of laser pulses. On the other hand, the transmittance spectra are opposite in their behavior to the absorbance spectra, as their values increase towards higher wavelengths. The absorption coefficient curves are similar to the absorbance curves as their values depend on the absorbance values. The results agreed with the previous literature. Zn NPs as well as ZnO NPs can be used as a good alternative to antibiotics in inhibiting the growth and killing of *S. aureus*. In any case, and benefiting from the results of this work and other similar works, it is possible to develop work using different laser parameters in preparing Zn NPs, improve it, and monitor the results accurately, as Zn NPs can be used in toothpastes or mouthwashes because the applied bacteria are isolated from the oral cavity.

References

[1] R. Zamiri et al., "Aqueous Starch as a Stabilizer in Zinc Oxide Nanoparticle Synthesis via Laser Ablation", *J. Alloys Comp.*, 516 (2012) 41-48.

[2] M.Z. Alhamid, B.S. Hadi and A. Khumaeni, "Synthesis of Silver Nanoparticles Using Laser Ablation Method Utilizing Nd: YAG Laser", AIP Conf. Proc., 2202(1) (2019) 020013.

[3] K.S. Khashan et al., "Antibacterial Activity of TiO_2 Nanoparticles Prepared by One-Step Laser Ablation in Liquid", *Appl. Sci.*, 11(10) (2021) 4623.

[4] S. Dadashi, R. Poursalehi and H. Delavari, "Structural and Optical Properties of Pure Iron and Iron Oxide Nanoparticles Prepared via Pulsed Nd:YAG Laser Ablation in Liquid", *Procedia Mater. Sci.*, 11 (2015) 722-726.

[5] R. Jorfi, "Preparation of zinc oxide nanoparticles by laser ablation in various liquid media", MSc. thesis, University Purta Malaysia (2014).

[6] M. Moradi et al., "Effect of Aqueous Ablation Environment on the Characteristics of ZnO Nanoparticles Produced by Laser Ablation", *J. Cluster Sci.*, 27(1) (2016) 127-138.

[7] A. Al-Sharqi et al., "Enhancement of the Antibacterial Efficiency of Silver Nanoparticles Against Gram-Positive and Gram-Negative Bacteria Using Blue Laser Light", *Int. J.*

Photoenergy, (2019) article ID 2528490.

[8] D. Samson, T. Adeeko and E. Makama, "Synthesis and Optical Characterization of Silver Nanoparticles (Ag-NPs) Thin Films (TFs) Prepared by Silar Technique", *Int. J. Curr. Res. Acad. Rev*., 5(12) (2017) 15-24.

[9] V. Manikandan et al., "Green Synthesis of Silver Oxide Nanoparticles and Its Antibacterial Activity Against Dental Pathogens", *3 Biotech*, 7(72) (2017) 1-9.

[10] A. Mehrani, D. Dorranian and E. Solati, "Properties of Au/ZnO Nanocomposite Prepared by Laser Irradiation of the Mixture of Individual Colloids", *J. Cluster Sci*., 26(5) (2015) 1743-1754.

[11] L.S. Arias et al., "Iron Oxide Nanoparticles for Biomedical Applications: A Perspective on Synthesis, Drugs, Antimicrobial Activity, and Toxicity", *Antibiotics*, 7(46) (2018) 7020046.

[12] L.S. Ganapathe et al., "Magnetite (Fe_3O_4) Nanoparticles in Biomedical Application: From Synthesis to Surface Functionalisation", *Magnetochem.*, 6(68) (2020) (35 pages).

[13] R. Kalaivani et al., "Synthesis of Chitosan Mediated Silver Nanoparticles (Ag NPs) For Potential Antimicrobial Applications", *Front. in Lab. Med.*, 2 (2018) 30-35.

[14] A.G.M. Haldar et al., "Natural Extracts-mediated Biosynthesis of Zinc Oxide Nanoparticles and Their Multiple Pharmacotherapeutic Perspectives", *Jordan J. Phys.*, 15(1) (2022) 67-79.

[15] D.M. Cruz et al., "Green Nanotechnology-Based Zinc Oxide (ZnO) Nanomaterials for Biomedical Applications: A Review", *J. Phys.: Materials*, 3 (2020) 034005.

[16] A.M. Mostafa and E.A. Mwafy, "Synthesis of ZnO and Au@ ZnO Core/Shell Nano-catalysts by Pulsed Laser Ablation in Different Liquid Media", *J. Mater. Res. Technol.*, 9(3) (2020) 3241-3248.

[17] J.A. Tanna et al., "Histidine-capped ZnO Nanoparticles: An Efficient Synthesis, Spectral Characterization and Effective Antibacterial Activity", *BioNanoSci.*, 5 (2015) 123-134.

[18] A.H. Hammadi et al., "Synthesis, Characterization and Biological Activity of Zinc Oxide Nanoparticles (ZnO NPs)", *Syst. Rev. in Pharm.*, 11(5) (2020) 431-439.

[19] A.M. Hamad and Q.M. Atiyea, "*in vitro* Study of the Effect of Zinc Oxide Nanoparticles on *Streptococcus mutans* Isolated from Human Dental Caries", *IOP J. Phys.: Conf. Ser.*, 1879(2) (2021) 022041.

[20] D. Goncharova et al., "Antibacterial Activity of Zinc Oxide Nanoparticles Obtained by Pulsed Laser Ablation in Water and Air", *MATEC Web Conf.*, EDP Sciences, 243 (2018) 00017.

[21] S. Juwita et al., "Genetic Relationship of *Staphylococcus aureus* Isolated From Humans, Animals, Environment, and Dangke Products in Dairy Farms of South Sulawesi Province, Indonesia", *Veter. World*, 15 (2022) 558-564.

[22] J.W. Hommes and B.G. Surewaard, "Intracellular Habitation of *Staphylococcus aureus*: Molecular Mechanisms and Prospects for Antimicrobial Therapy", *Biomed.*, 10 (2022) 1804.

[23] S.N. Rashid, K.A. Aadim and A.S. Jasim, "Silver Nanoparticles Synthesized by Nd:YAG Laser Ablation Technique: Characterization and Antibacterial Activity", *Karbala Int. J. Mod. Sci.*, 8(1) (2022) 71-82.

[24] S.N. Rashid et al., "Synthesized Zinc Nanoparticles via Pulsed Laser Ablation: Characterization and Antibacterial Activity", *Karbala Int. J. Mod. Sci.*, 8(3) (2022) 462-476.

[25] S.N. Rashid, A.S. Jasim and K.A. Aadim, "Influence of Number of Pulses on Characterization of Nanoparticles of Copper and its Oxides Synthesized by Nd:YAG Laser Ablation Technique and its Antibacterial Activity", *NeuroQuantol.*, 20(3) (2022) 150-159.

[26] R. Li et al., "Giant Enhancement of Nonlinear Optical Response in Nd:YAG Single Crystals by Embedded Silver Nanoparticles", *Acs Omega*, 2 (2017) 1279-1286.

[27] N. Korkamaz and A. Karadag, "Microwave Assisted Green Synthesis of Ag, Ag_2O, and Ag_2O_3 Nanoparticles", *J. Turkish Chem. Soc. Sec. A: Chem.*, 8(2) (2021) 585-592.

[28] O.A. Hammadi, "Magnetically-Supported Electrically-Induced Formation of Silicon Carbide Nanostructures on Silicon Substrate for Optoelectronics Applications", *Opt. Quantum Electron.*, 54(7) (2022) 427.

[29] K.S. Khashan et al., "Synthesis, Characterization and Evaluation of Anti-Bacterial, Anti-Parasitic and Anti-Cancer activities of Aluminum-Doped Zinc Oxide Nanoparticles", *J. Inorg. Organomet. Pol. Mater.*, 30(9) (2020) 3677-3693.

[30] A.S. Jasim, K.I. Mohammed and S.N. Rashid, "Effect of Annealing by CO_2 Laser on Structural and Optical Properties of Zinc Oxide Thin Films Prepared by Sol–Gel Method", *Tikrit J. Pure Sci.*, 21(4) (2016) 112-121.

[31] S.N. Rashid and S.M. Fayyadh, "Effect of Beta Ray on the Optical Properties of CuO Thin Films", *Diyala J. Pure Sci.*, 14(4) (2018) 40-52.

[32] A.A. Mahmood, H.M. Mikhlif and O.A. Hammadi, "Fluorescence Characteristics of Highly-Pure Nanoparticles Embedded in Dye Complexes for Random Laser Design", *Iraqi J. Appl. Phys.*, 18(2) (2022) 27-32.

 ISSN 1813-2065 (print) 2309-1673 (online) PRINTED IN IRAQ

IRAQI JOURNAL OF APPLIED PHYSICS
Volume 19, Issue 2, April-June 2023, 9-14

Proceedings of the 3rd International Scientific Conference and 5th Scientific Conference, organized by College of Science, University of Tikrit, Tikrit, Iraq (28-29 December 2022)

Rasha F. Hasan[1]
Raad A. Rassol[2]

[1] *Department of Education in Mosul, Ministry of Education, Mosul, IRAQ*
[2] *Department of Physics, Education College of Pure Science, University of Mosul, Mosul, IRAQ*

Analysis the Performance of ZnO/CdS/SnS Solar Cell Using Software Program SCAPS-1D

Photovoltaic solar cells were analyzed numerically to ascertain whether or not the proposed physical structure was feasible. In this study, the effectiveness of a solar cell made of a CdS window and an SnS absorber was determined. ZnO was incorporated as a transparent conductive oxide (TCO). All of the ZnO, CdS and SnS-related programming settings were entered into SCAPS-1D before it was used. The ideal thickness of the SnS absorption layer in a solar cell was determined to be 2 m. The effect of the energy gap on the behaviour of the absorbing layer was studied. Maximum light absorption by solar cells is achieved when their energy gaps are in the sweet spot of the average solar spectrum (about 1.5 MG). Capacitance-voltage (C-V) characteristics and solar cell performance were also studied to see how they changed with temperature.

Keywords: Solar cells; Photovoltaics; Transparent conducting oxide; SCAPS-1D
Received: 25 November 2022; **Revised:** 29 November 2022; **Accepted:** 05 December 2022

1. Introduction

A solar cell, also known as a photovoltaic cell, is an electrical device that uses the photovoltaic effect (a physical and chemical phenomenon) to transform the energy of light into electricity [1]. Different photovoltaic technologies are at varying points in their evolution towards this goal, with solar cells at 100% radiatively efficient representing the maximum feasible photovoltaic performance. There are now two main methods for creating photovoltaic cells (crystalline and monocrystalline, and thin film cells) [2]. However, the production cost of crystal cells is quite high compared to other structures [3], so in this technological era, researchers have focused heavily on the advancement of thin films. As one of the greatest obstacles to renewable energy, solar cell production poses the greatest difficulty for these applications [4]. The growth of solar cells necessitates a change in the materials used in their production, therefore the uses of thin films, which are a part of materials science, have been deemed useful in the recovery of solar cells [4]. The goal of this paper was to study and simulate photovoltaic solar cells that use tin sulfide (SnS) as an absorption layer. This is because of the unique properties of this material, which is a semiconductor and is found in the periodic table (IV-VI). This substance is also safe and can be found in nature. Additionally, a Windows layer made of cadmium sulfide (CdS) and a transparent conducting oxide (TCO) layer made of zinc oxide (ZnO) were employed. A simulation program called SCAPS-1D [1] for developing one-dimensional solar cell structures was used to perform a numerical analysis of the proposed solar cell. This program was produced at the Department of Electronics and Systems Information, the University of Gent in Belgium, where a group of researchers used an SnS layer as an absorption layer when designing solar cells. The ZnS/SnS absorption layer and heterogeneous window layer models were among those investigated by Xu et al. [5]. The ZnS/SnS model had the highest conversion efficiency (16.26%). This was achieved by making the ZnS window layer thinner and the SnS absorption layer thicker. Basak et al. [6] used the thermal evaporation method to prepare SnS thin films on glass substrates at different temperatures. They got the best crystal surface change at 300°C compared to 450°C because sulphur (S) losses at this permeability temperature and the refractive index as a result of the gap reduction with temperature. Since this technique can provide anti-reflection coating as a window layer on the surface of the solar cell to trap as much of the incident light on the cell and reduce reflection, Minbashi et al. [4,7] also constructed and simulated a solar cell using SCAPS-1D.

In this work, the photoelectric parameters of the prepared solar cell were determined. The optimum thickness of the absorption layer (p-SnS) was 2μm that of the window layer (n-CdS) was 30μm in order to measure the arrival of light (photons) from the transmission layer (TCO) to the absorption layer.

2. Materials and Research Methods

The simulation program SCAPS-1D is used to optimize the design of solar cells with a one-dimensional capacity. This program assists in obtaining internal details of solar cells. The principle of this program is to simulate the electrical properties of solar cells by solving basic semiconductor

equations in one dimension represented by Poisson's equation [8,9]

$$\frac{\partial \hat{E}}{\partial x} = P + N_D^+ - n - N_A^- \quad (1)$$

The equations that describe the transport of the total current are represented by the diffusion and drift processes of electrons and holes, respectively [9].

$$J_n = qn\mu_n E + qD_n \frac{dn}{dx} \quad (2)$$

$$Jp = qp\mu_p E + qD_p \frac{dp}{dx} \quad (3)$$

The recombination process through fusion centers in the mean levels is also described by the continuity equation [8,9], which describes both the diffusion and drift processes for charge carriers

$$\frac{\partial n}{\partial t} = \frac{1}{q}\frac{\partial J_n}{\partial x} + (G_n - U_n) \quad (4)$$

$$\frac{\partial p}{\partial t} = \frac{1}{q}\frac{\partial J_p}{\partial x} + (G_P - U_P) \quad (5)$$

Output parameters, such as short-circuit current density (J_{SC}) and maximum current produced by a solar cell (MPSC) when the edges of the solar cell are in contact with each other, are the most essential elements that describe the performance of the solar cells.

The maximum voltage that a cell may generate when its terminals are disconnected from one another (known as "open-circuit voltage" or V_{OC}) is given as [10]

$$V_{OC} = \frac{k_B T}{q} \ln\left(\frac{I_L}{I_0} + 1\right) \quad (6)$$

where I_L represents the photo-generated current, I_0 represents the saturation current of diode (p-n), k_B is Boltzmann's constant, T is the temperature and q is the electrical charge

The fill factor (FF) represents the ratio between the maximum power (product of maximum voltage and maximum current density) that a solar cell can produce to the product of open-circuit voltage and short-circuit current as [10]:

$$FF = \frac{V_{mp} \times I_{mp}}{V_{OC} I_{SC}} = \frac{P_{max}}{V_{OC} I_{SC}} \quad (7)$$

The efficiency of a solar cell (η), which represents the ratio between maximum power generated by the solar cell to the incident power, can be calculated from the following equation [10]:

$$\eta = \frac{P_{max}}{P_{in}} = \frac{I_{SC}\, V_{OC}\, FF}{P_{in}} \times 100\% \quad (8)$$

The design of the proposed solar cell is illustrated in Fig. (1). As the p-SnS layer is used as a basic material for solar cell design due to its low band gap energy (1.13-1.43eV), the SnS layer is the main substrate of the cell due to its ability to absorb the maximum amount of incident light to excite the electron to highest energy states as well as its ability to transport those excited electrons from a solar cell in external circuit [4]. With the chemically stable and heterogeneous (pn) junction formed by the n-CdS "windows" layer, the electrons emitted from the absorption layer can be efficiently collected and transferred to special contacts with minimal losses [11]. This is possible because of the direct and wide energy gap possessed by the SnS layer, which is 2.42eV. Since the TCO layer has a high transmittance of 90-95% [10,11], most of the visible sun radiation can pass through to the basic SnS layer when ZnO is used as the TCO. Parameters in the layers are based on the constants and data of both materials collected from experiments. The most critical design cell parameters are listed in Table (1).

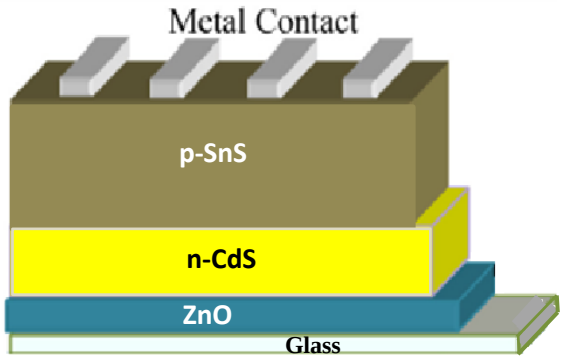

Fig. (1) Schematic diagram of designing solar cell

3. Results and Discussion

The effects of thickness of absorption layer (p-SnS) and window layer (n-CdS) on the electrical properties (V_{OC}, J_{SC} and FF) as well as the effect of absorption layer (p-SnS) thickness on capacitance-voltage (C-V) characteristics have been examined. The effects of energy band gap of the absorption layer as well as of temperature on solar cell performance have also been studied.

The SnS is distinguished from other materials by its high absorption coefficient of 10^5 cm^{-1} [12], which gives SnS the ability to absorb the greatest number of incident photons on the cell and convert them into electron-hole pairs, allowing for high efficiency at a low cost. Figure (2) shows the solar cell output parameters, which remain constant after a thickness of 2μm of p-SnS, as the influence of p-SnS thickness is evaluated by checking all the parameters steadily in Table (1) with the stability ratio of impurity of the absorption layer at shallow uniform acceptor density (N_A=10^{15} cm^{-1}), and vice versa. As the rate at which an electron-hole pair is generated from incident photons on a solar cell grows with increasing thickness of the p-SnS layer, the efficiency of the solar cell is enhanced as well; however, at η=13.79%, the optimal thickness of the absorption layer is 2 μm.

The n-CdS layer, the ideal companion for the SnS layer, serves as the window layer and its wide and direct energy gap of 2.45 eV allows for the transmission of a large portion of the solar radiation. Furthermore, raising the distortion ratio of the shallow uniform donor density (N_D=10^{19} cm^{-1}) in this layer lowers the effect of straight resistance [13]. In this study, the thickness of the p-SnS absorption layer was maintained at 2 μm.

The optimum thickness of n-CdS was determined by evaluating values between 10 and 100 nm, as illustrated in Fig. (1). Due to a linear relationship between optical current and open-circuit voltage

 ISSN 1813-2065 (print) 2309-1673 (online)

(V_{OC}) drops with increasing layer thickness. The creation of trapping centers, which deplete the minority charge carriers, and the recombination processes at larger thickness are also seen to reduce the value of short-circuit current density (J_{SC}) [14].

As for fill factor (FF), its value decreases as the thickness of this layer is increased because of an increase in the resistance of the series [10] leading to a corresponding decrease in efficiency as a result of preventing the arrival of the photons in the absorption layer. The optimal thickness for an n-CdS layer is 30µm; however, in practice, the thickness of n-CdS layers are typically lower than that of p-SnS layer to allow photons (light) from the outside passing through to the absorber.

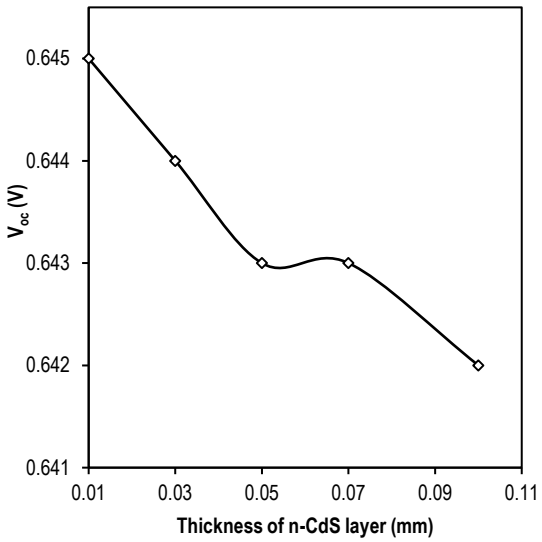

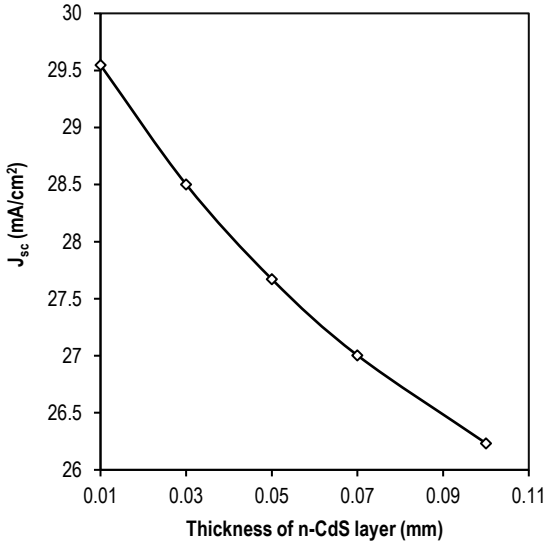

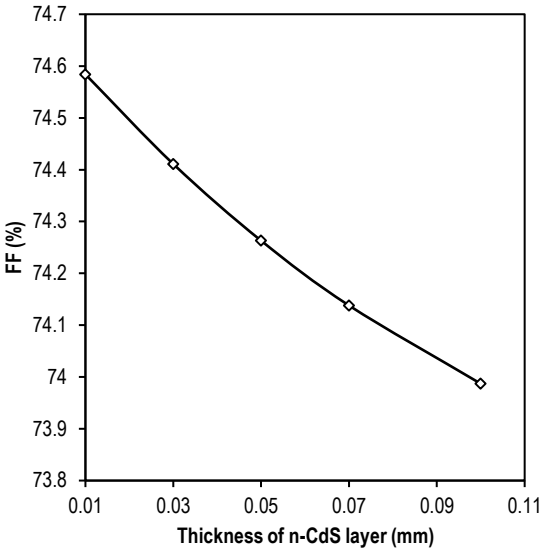

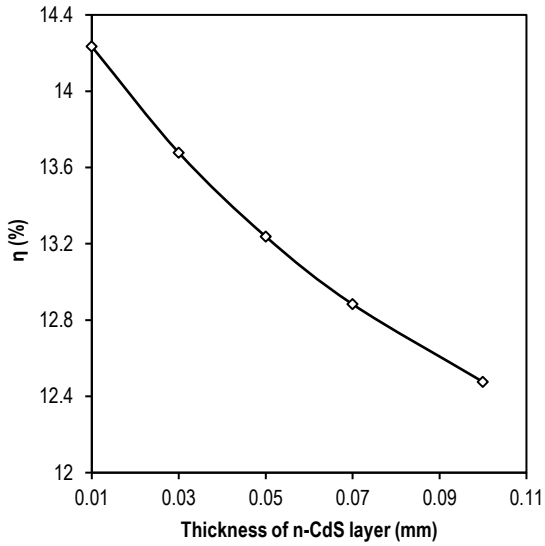

Fig. (2) Effect of n-CdS layer thickness on output parameters

The capacitance of a solar cell decreases as the thickness of the p-SnS absorption layer is increased [15], because more photoelectrons mean a higher internal voltage (V_{bi}) and a larger depletion area. As shown in Fig. (3), there are two distinct regions, the lower of which has a voltage constraint of about (-0.8 to 0.6V). The second region is also voltage-limited, falling between 0.6 and 0.8V. The diode operates in forward bias within this range, with the depletion layer's thickness at its minimum and capacitance at its maximum [15].

There are two distinct phases inside the depletion region, as shown in Fig. (4); the first is independent of voltage and signals that the depletion region has reached its maximum thickness and stability due to the presence of an electric field created by the presence of non-neutral ions (positive charges in the n-type side and negative charges in the p-type side, respectively) that work to prevent the movement of electrons and holes. In the second part, both the voltage barrier and the size of depletion region are

found to decrease when the diode is biased in the forward direction [10,16].

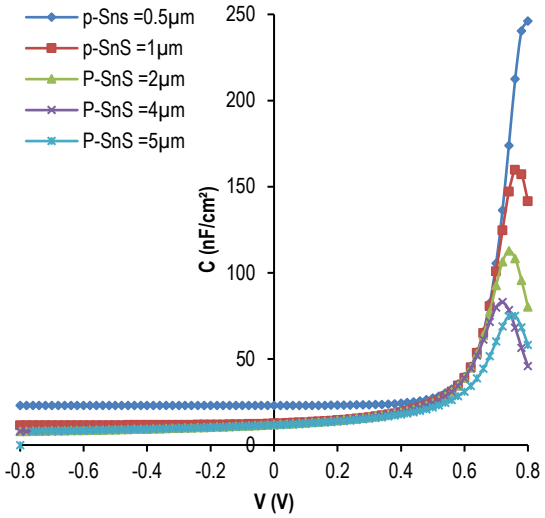

Fig. (3) Effect of p-SnS layer thickness on the C-V characteristics of the proposed solar cell

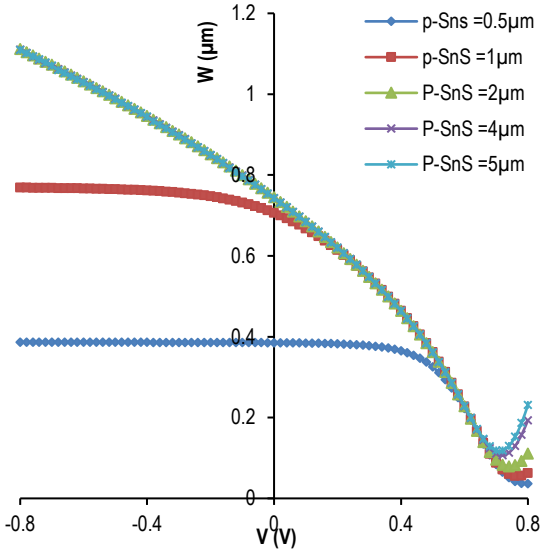

Fig. (4) Effect of p-SnS layer thickness on the width of depletion region (W-V)

The change in the energy gap of the p-SnS layer from 1.13 to 1.43 eV was tested to introduce its effect on the efficiency of the solar cell. Figure (5) depicts the impact of the energy gap on the characteristics of the I-V curve; as the energy gap approaches the optimal energy gap range, the absorption of incident light photons increases, which excites the electrons from the valence band to the conduction band region, leading to a rise in the curve. This absorption of most solar radiation also contributes to the cell's efficiency [3] as the highest efficiency was achieved at an energy gap of 1.43 eV.

The influence of temperature on the operation of the proposed solar cell was studied within the range 300-360K, after fixing the thickness of each layer of the cell, as the thickness of the absorption layer p-SnS is 2µm and that of window layer n-CdS is 30µm in addition to fixing the thickness of TCO layer ZnO at 100µm, as shown in Fig. (6) and hence lowering the I-V curve as the temperature is varied. When the temperature is increased, the absorption of incident light increases due to the decrease in the energy gap [10-12], and the value of V_{OC} drops due to an increase in the reverse saturation current (I_S), which increases when the diffusion length of charge carriers decreases and the lifetime of the minority carriers decreases, and hence diminishing the efficiency of the solar cell. This layout was tested at different temperatures and found to be thermally stable.

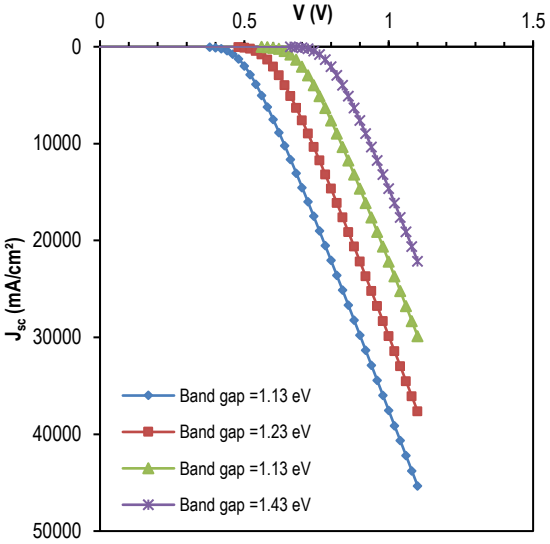

Fig. (5) Effect of energy gap on the I-V characteristics

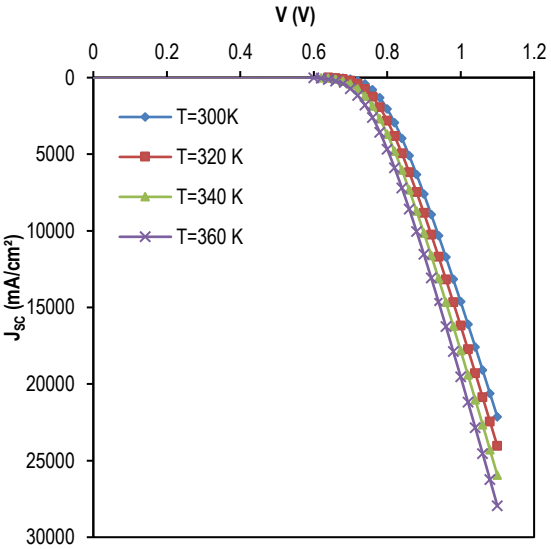

Fig. (6) Effect of the temperatures on the I-V characteristics

Internal voltage (V_{bi}), charge carrier concentration (N), depletion region width (W), and charge distribution in the hybrid dispersion may all be determined using the C-V curve, which is one of the considerable electrical measurements [17,18]. Higher temperatures sped up the depletion process in that

 ISSN 1813-2065 (print) 2309-1673 (online)

region because they narrowed the energy gap, bringing the Fermi level closer to the valence and conduction bands. As the temperature was increased, the value of V_{OC} decreased, which meant that the capacitance of the solar cell decreased too. This is because the charge density in both bands (conduction and valance) depends on the difference in energy between the two bands and the Fermi level [19], as shown in figures (7) and (8).

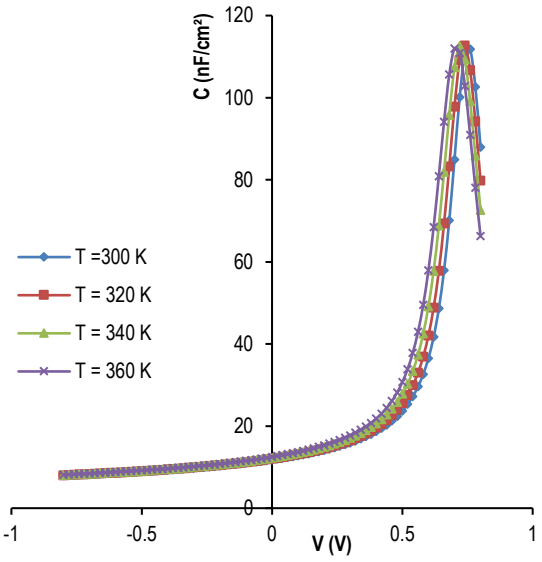

Fig. (7) Effect of temperatures on the C-V characteristics

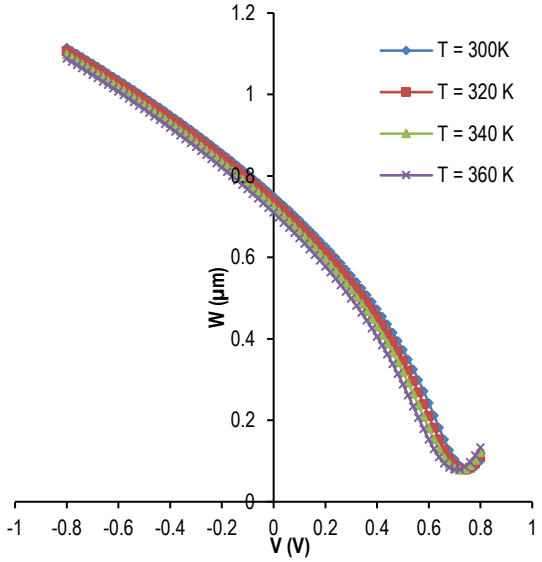

Fig. (8) Effect of temperatures on the width of depletion region (W)

4. Conclusions

Optimal values of layer thickness in a proposed design of solar cell were determined to be 2 µm for the absorption layer (p-SnS) and 30 µm for the window layer (n-Cds), with higher efficiency achieved by increased light transmission through the thinner absorption layer. By examining the properties of the C-V curve, it was shown that an increase in the thickness of the absorption layer causes an increase in the internal (built-in) voltage (V_{bi}) as well as an increase in the width of the depletion region (W), both of which result in a decrease in capacitance. This design of the solar cell also demonstrated thermal stability with changes in temperature within the range of 300-360 K, with the following values V_{OC} of 0.6544V, J_{SC} of 28.308mA/cm^2, FF of 74.39%, and η of 13.79%.

References

[1] R. Garain, A. Basak and U.P. Singh, "Study of thickness and temperature dependence on the performance of SnS based solar cell by SCAPS-1D", *Materials Today: Proc.*, 39(5) (2020) 1833-1837.

[2] H. Zerfaoui et al., "Study by simulation of the SnO_2 and ZnO anti-reflection layers in n-SiC/p-SiC solar cells", *AIP Conf. Proc.*, 1758(1) (2016) 030029.

[3] F. Baig, "Numerical analysis for efficiency enhancement of thin film solar cells", PhD thesis, University of Valencia (2019).

[4] M. Minbashi et al., "Simulation of high efficiency SnS-based solar cells with SCAPS", *Solar Energy*, 176 (2018) 520-525.

[5] J. Xu Y. and Yuanzheng, "Study on the performances of SnS heterojunctions by numerical analysis", *Energy Conv. Manage.*, 78 (2014) 260-265.

[6] A. Basak, A. Mondal and U.P. Singh, "Impact of substrate temperature on the structural، optical and electrical properties of thermally evaporated SnS thin films", *Mater. Sci. Semicond. Process.*, 56 (2016) 381-385.

[7] O.A. Hamadi, B.A.M. Bader and A.K. Yousif, "Electrical Characteristics of Silicon p-n Junction Solar Cells Produced by Plasma-Assisted Matrix Etching Technique", *Eng. Technol. J.*, 26(8) (2008) 995-1001.

[8] J-P. Colinge and C.A. Colinge, **"Physics of Semiconductor Devices"**, 2nd ed., Kluwer Academic Pub. (NY, 2002).

[9] F. Baig, S. Bernabé María and H.K. Yousaf, "Effect of Band Offset and Temperature on the Performance of $Zn_xCd_{1-x}S$/SnS Solar Cell", in *6th Int. Renew. Sustain. Energy Conf. (IRSEC, IEEE)* (2018) 1-4.

[10] S.S. Chetan, **"Solar Photovoltaic Fundamentals, Technologies and Applications"**, 2nd ed., PHI Learning Private Ltd. (Delhi, 2013) 110092.

[11] A. Verma and A. Pallavi, "Modeling of thin film solar photovoltaic based on ZnO/SnS oxide-absorber substrate configuration", *Int. J. Eng. Appl.*, 4(6) (2014) 14-18.

[12] M.A. Green, "Solar Cells: Operating Principles, Technology and System Applications", University of New South Wales (1986) 165.

[13] R.A. Rassol et al., "Numerical Analysis of SnO_2/Zn_2SnO_4/n-CdS/p-CdTe Solar Cell Using

the SCAPS-1D Simulation Software", *Iraqi J. Sci.*, 62(2) (2021) 505-516.
[14] R. Scheer and S. Hans-Werner, "Chalcogenide Photovoltaics: Physics, Technologies, and Thin Film Devices", Wiley-VCH Verlag GmbH (Weinheim, 2011) Ch. 2, 63.
[15] F. Anwar et al., "Simulation and performance study of nanowire CdS/CdTe solar cell", *Int. J. Renew. Energy Res.*, 7(2) (2017) 885-893.
[16] A.A. Mouhammed and A.N. Saleh, "Simulation Effect of Ga_2O_3 layer Thickness on CdTe solar cell by SCAPS-1D", *Tikrit J. Pure Sci.*, 24(6) (2019) 110-118.
[17] S.M. Sze and K.K. Ng, **"Physics of Semiconductor Devices"**, 3rd ed., John Wiley & Sons Inc. (NJ, 2006), Ch. 2, 124.
[18] M.T. Al-Azawi, H.K. Al-Lamy and R.A. Al-Ansari, "Structural Properties and IV, CV Characteristic for a-Ge: In/c-Si Heterojunction", *J. Electron. Dev.*, 20 (2014) 1711-1717.
[19] A.S. Grove, **"Physics and Technology of Semiconductor Device"**, Wiley & Sons Inc. (1967).

Table (1) The most important parameters used in the designed cell

Parameters	n-ZnO	n-CdS	p-SnS
Thickness (µm)	0.1	0.03	2
Band gap (eV)	3.35	2.42	1.43
Electron affinity(eV)	4.5	4.5	4
Dielectric permittivity (relative)	9	9	13
CB effective density of states ($1/cm^3$)	2.2×10^{18}	2.2×10^{18}	1.18×10^{18}
VB effective density of states ($1/cm^3$)	1.8×10^{19}	1.7×10^{19}	4.76×10^{19}
Electron thermal velocity (cm/s)	1×10^{7}	1×10^{7}	1×10^{7}
Hole thermal velocity (cm/s)	1×10^{7}	1×10^{7}	1×10^{7}
Electron Mobility (cm^2/Vs)	320	450	150
Hole Mobility (cm^2/Vs)	3	50	100
Shallow uniform donor density, N_D ($1/cm^3$)	1×10^{19}	1×10^{19}	0
Shallow uniform acceptor density N_A ($1/cm^3$)	0	0	1×10^{15}

 ISSN 1813-2065 (print) 2309-1673 (online)

IRAQI JOURNAL OF APPLIED PHYSICS
Volume 19, Issue 2, April-June 2023, 15-20

Proceedings of the 3rd International Scientific Conference and 5th Scientific Conference, organized by
College of Science, University of Tikrit, Tikrit, Iraq (28-29 December 2022)

Calculations of Nuclear Two-Component State Density in Non-Equidistant Spacing Model with Modified Williams' Formula

Hanan M. Saleh[1]
Ahmed A. Selman[2]

[1] *Department of Physics, College of Education for Women, University of Kirkuk, Kirkuk, IRAQ*
[2] *Department of Astronomy and Space, College of Science, University of Baghdad, Baghdad, IRAQ*

The level density of the nuclear states represents the core parameter in the calculations of the pre-equilibrium reactions. In a previous study, the fundamental analytical formula was derived. An attempt was made in this work to develop a solution the previous one in order to include the pairing energy correction. When pairing correction was implemented, it was shown that the current non-ESM state density calculation formula would produce the best results when compared to the conventional approach. A further suggestion is to incorporate the effects of Fermi and binding energies for particles and holes, respectively. And the analytical solution was found, which shows how hard it can be to get a formula to behave in a way that makes more reasonable treatment.

Keywords: Exciton model; Pre-equilibrium reactions; Level density; Non-ESM
Received: 22 November 2022; **Revised:** 26 November 2022; **Accepted:** 30 November 2022

1. Introduction

Nuclear reactions are classified as low, medium, or high energy depending on the energy of the incident particle. The pre-equilibrium (PE) region is a stage in nuclear reactions in which the excitation energy is not distributed evenly among the nucleons of the excited nucleus [1]. The partial level density (PLD) in pre-equilibrium reactions (it represents the level density of excitation of some nucleons in nuclei) is used from exciton model that was suggested by J.J. Griffin in 1966 [4]. The level density for excited nuclei is not easily measurable parameter. The lack of full understanding of the nuclear structure made the theoretical description of this quantity to be a complicated task. Therefore, physicists tried to overcome such complication by adopting many simplifications and approximations when describing the level density of the excited nucleus. In order to obtain more accurate description with better results, the approximate description is reconsidered in the theoretical frame. [3-4]. The exciton model proposes that when the bombarding particle collides with the target nucleus, it begins to share its energy with the first particle that collides with it, and then the nuclear emission occurs through successive nucleon-nucleon interactions in a series of stages before attending to the complete interactions (equilibrium). Each contact generates a particle-hole (p-h) pair, and the sum of these particles and holes is known as an Exciton. [5]. The mechanism of exciton formation explains energy sharing and nucleon emission, which is quantified as the ratio of residual state density to that of the first excited state. This model has rapidly evolved over the past decades, and it is now represented as a family of models aimed at explaining nuclear reactions responsible for continuum emission. Pre-equilibrium emission (PE) describes nuclear reactions of various projectile-ejectile types at intermediate energies well. [6-7], and for very large values of E, we have the sum of ω as:

$$\omega_1(E) = \sum_{p=h} \omega(n, E) \qquad (1)$$

The sum of the partial state densities in Eq. (1) for all permitted pairs of p-h number in two-component system with an average total single-particle state density is,

$$\omega_2(E) = \sum_{p_\pi=h_\pi, p_\upsilon=h_\upsilon} \omega(p_\pi, p_\upsilon, h_\pi, h_\upsilon, E) \quad (2)$$

Important nuclear properties including Pauli [8], finite depth and bound state correction [9], pairing [10-11], the back shift correction [10], surface effect [12-13], the parity correction [9-14], charge effect [5], linear and angular momentum [9-15], isospin [16-18] and the two-component formalism extension [14] (when the neutron and proton particle-hole distinction is maintained throughout the reaction chain), have all been modified into this model. The derivation approach was properly discussed theoretically and, in the literature, before in first paper [19], therefore the theoretical modification presented below tries to expand on that earlier work. In this study, we compare

the modified pairing component of the earlier treatment with the modified Williams' formula of two-component.

2. The Modified Williams Formula in Two-Component System

Because a statistical approach is employed to describe level density in pre-equilibrium reactions. Statistically, a pairing effect is also introduced to the pre-equilibrium processes (and not quantum mechanical one). This is due to the fact that the level density in pre-equilibrium reactions is primarily suggested and discovered from a statistical standpoint, in accordance with the basic idea of pre-equilibrium reactions, and as we know, Griffin's idea was founded on such a statistical approach. The "Fermi Gas Model" (FGM) serves as the general theoretical framework for this pairing correction treatment. [2-10]. Pairing energy also affects the level density, because the amount of energy added to the excitation energy will highly influence the excitation process and exciton formation, thus level density of the excited nucleus. In experiments dealing with level density calculations, it is very useful to add the pairing energy as a leading parameter [20]. The effects of particle pairing are taken into account in this formula. The state density calculation can be significantly corrected by pairing [1,6]. This influence is taken into account in a way that the excitation energy is adjusted by further deducting the energy $P(\Delta)$, which takes paring as a function of the energy gap (Δ) into account. Only the fundamental equations are included here because Avrigeanu et al. and Harangozo et al. [2,21] provided a thorough description of the treatment. Since Pauli principle implies no two excitons in the same energy state, the state density must modify to be consistent with the pairing interaction between couples of particles as a correction, $P(\Delta)$, that required energy taken from the excitation energy, so the two-component state density formula for this approach is $\omega(n,E,P)$, where $P_2(\Delta)$ is the pairing energy given by: [21,22]

$$\omega(n,E,P) = \frac{g^n\left(E-P_2(\Delta)-B_{p_\pi,h_\pi,p_\upsilon,h_\upsilon}\right)^{n-1}}{p_\pi!p_\upsilon!h_\pi!h_\upsilon!(n-1)!}\,\Theta\left(E-P_2(\Delta)-B_{p_\pi,h_\pi,p_\upsilon,h_\upsilon}\right) \quad (3)$$

In above equation, it is better to have the Heaviside step function of the following form, $\Theta(E-P_2(\Delta)-Bp_\pi,h_\pi,p_\upsilon,h_\upsilon)$ in its structure. This is because at small values of energy (less than ~10MeV), the relation curve for $\omega(n,E,P)$ with energy suffers from a sudden drop .This is due to the fact that $[P_2(\Delta)+Bp_\pi,h_\pi,p_\upsilon,h_\upsilon]$ might be larger than E at such low energy, where B is the modified Pauli correction that comes after the unmodified factor, Williams term A, [10,22]:

$$B_{p_\pi,h_\pi,p_\upsilon,h_\upsilon} = A_{p_\pi,h_\pi,p_\upsilon,h_\upsilon}\left[1+(2g\Delta/n)^2\right]^{1/2} \quad (4)$$

where

$$A_{p_\pi,h_\pi,p_\upsilon,h_\upsilon} = \left[\frac{p_\pi(p_\pi+1)+h_\pi(h_\pi-3)}{4g_\pi}+\frac{p_\upsilon(p_\upsilon+1)+h_\upsilon(h_\upsilon-3)}{4g_\upsilon}\right] \quad (5)$$

and the pairing correction term $P_2(\Delta)$ for two components

$$P_2(\Delta) = 2P_1(\Delta) \quad (6)$$

$$P_2(\Delta) = \frac{1}{4}g(\Delta_0^2-\Delta^2) \quad (7)$$

is determined by the ground state gap Δ_0 and excited state gap $\Delta(p,h,E)$, Δ is the energy gap of excited state that is obtained from the curve fitting. The former is related to the condensation energy $C = g\Delta_0^2/4$. The relation between Δ and Δ_0 that is obtained by Fu [10]:

$$\frac{\Delta}{\Delta_0} = 0.996-1.76(n/n_c)^{1.60}(E/C)^{-0.68} \quad if\ E \geq E_{phase}$$

$$\frac{\Delta}{\Delta_0} = 0 \quad if\ E < E_{phase} \quad (8)$$

where $n_c = 0.792g\Delta_0$ is the critical number of excitons and E_{phase} is the pairing phase transition energy given by

$$E_{phase} = C\left[o.716+2.44\left(\frac{n}{n_c}\right)^{2.17}\right] \quad if\ \frac{n}{n_c} \geq 0.446 \quad (9)$$

$$E_{phase} = 0 \quad if\ \frac{n}{n_c} < 0.446$$

The value of Δ_0 can be found from curve fitting to almost all known nuclei. This is done by relation known as Gilbert- Cameron formula.

$$\Delta_0 = \Delta_{0\pi}-\Delta_{0\upsilon} \quad (10)$$

where $\Delta_{0\pi}$ and $\Delta_{0\upsilon}$ are the energy gaps states of proton's particle and ground state of neutron's particle, respectively [1].

$$\Delta_{0\pi} = 1.654-9.58Z\times10^{-3} \quad (11)$$

$$\Delta_{0\upsilon} = 1.374-5.16N\times10^{-3} \quad (12)$$

The neutron and proton numbers are N and Z, respectively.

3. Modified Williams' Formula in non-ESM

The most important defect in the ESM is that it ignores the considerable shift in the energy levels due to nucleon-nucleon interaction. This shift of energy is not essentially included in the idea of the ESM, so one needs to add some correction factor that deals with energy shift due to nucleon-nucleon interaction [4]

$$\omega^{\text{non-ESM}}(n,E) = \frac{g_0^n}{2^{n-1}\pi^{n/2}p_\pi!h_\pi!p_\upsilon!h_\upsilon!}\,\Xi\frac{E^{N-1}}{F^{N-n}(N-1)!} \quad (13)$$

As Ahmed et al. [4] did, pairing modifications are applied by inspection to formula (13) in this paper. This will result in the corrected formula (14) at the end of the article:

Table (1) The parameters used in the present numerical study of level density calculations

Target nucleus under investigation	$^{54}_{26}Fe_{28}$
Mass number, A	24
Atomic number, Z	26
Maximum excitation energy, E	40 and 100 MeV
Exciton number	3,5,7
Exciton number configurations	two-component: [=$p\pi$, $h\pi$, pv, hv] (2,1,0,0),(2,1,1,1),(3,2,1,1)
Single particle density, g	A/13 (MeV-1)
Nucleon's binding energy	Proton: 8 (MeV) Neuron: 10 (MeV)
Finite depth of the nuclear potential well (this equals to the Fermi Energy)	Proton:38 (MeV) Neutron: 40 MeV

 ISSN 1813-2065 (print) 2309-1673 (online)

4. Exact method using Taylor expansion and inclusion of Fermi and Binding energies

The Heaviside step function will be ignored when B and F have very large bounds because the integrals will extend from zero to infinity without limitations. Inspection-based modifications to Eq. (13) term yielded the results reported so far. However, equations should employ more precise summation indices (13 and 14). The original formula, eq. (13), was derived using a method that considered these indices. This is a non-ESM state density calculation development idea. Reference [19] determines how to include Fermi and binding energies. Using this precise definition, the functions $P_\pi(k)$, $H_\pi(k)$, $P_\nu(k)$, and $H_\nu(k)$ are found to be identical to compare equations (36-39), respectively of Ref. [19]

$$P_\pi(k) = g_o \sum_{m=0}^{\infty} \frac{C_m^{p_\pi}}{F^m (ik)^{m+1}} \left(1 - \exp(-ikB) \sum_{s=0}^{m} \frac{(ikB)^s}{s!}\right) \tag{17}$$

$$H_\pi(k) = g_o \sum_{m=0}^{\infty} \frac{C_m^{h_\pi}}{F^m (ik)^{m+1}} \left(1 - \exp(-ikF) \sum_{s=0}^{m} \frac{(ikF)^s}{s!}\right) \tag{18}$$

$$P_\nu(k) = g_o \sum_{m=0}^{\infty} \frac{C_m^{p_\nu}}{F^m (ik)^{m+1}} \left(1 - \exp(-ikB) \sum_{s=0}^{m} \frac{(ikB)^s}{s!}\right) \tag{19}$$

$$H_\nu(k) = g_o \sum_{m=0}^{\infty} \frac{C_m^{h_\nu}}{F^m (ik)^{m+1}} \left(1 - \exp(-ikF) \sum_{s=0}^{m} \frac{(ikF)^s}{s!}\right) \tag{20}$$

From the equations above (17-20), we find that including (F and B) energies of Fermi and binding, respectively. This results in the subsequent with

$$\omega(n, E) = \frac{2g_0^n}{p_\pi! h_\pi! p_\nu! h_\nu!}$$

(see Eq. 21 at the end of the article)

This represents our final and exact solution to the state density equation for non-ESM dependency on B and F, where we have defined Ξ as in the index at the end of the article.

The preceding equations (21 and 22) clearly demonstrate how complex a formula would be if the exact dependence was required. In addition to the need for numerical computations of Eq. (21), Pauli blocking and pairing terms should also be included. These tasks will be further examined.

5. Results and Discussion

The non-ESM approach gains its importance from comparisons with the regular ESM approach because then one can see exactly what had happened after going through all these complications of the non-ESM theory. Therefore, below we use the ratio between the non-ESM results and those of the ESM. In this paper the selected comparisons will be focused on with modified Williams' formula that includes pair effect.

Figures (1a), (1b), (2a), (2b), (3a) and (3b) show that the ratio between the equation's state density (14) and modified Williams' formula in non-ESM, Eq. (13), for different configurations, (2,1,0,0) and (2,1,1,1), is always smaller than one, this mean that Eq. (14) always yields a lower state density than Eq. (13).

From figures (1a) and (1b) for the same configuration (2,1,0,0), it can be shown that changing the values of F has an effect on the state density, and that increasing the number of iterations makes the state density results more accurate and consistent at higher energies. The same is true for the other configurations in figures (2a), (2b) and (3).

Figures (4a), (4b), (5a), (5b), (5c) and (6) show the importance of the current treatment, which in turn improved the state density results through the possibility of increasing the number of terms, followed by the addition of the modified Williams' correction, which made the results match perfectly when compared with the results of a standard ESN formula (3) and for different configurations as well as for different numbers of iterations.

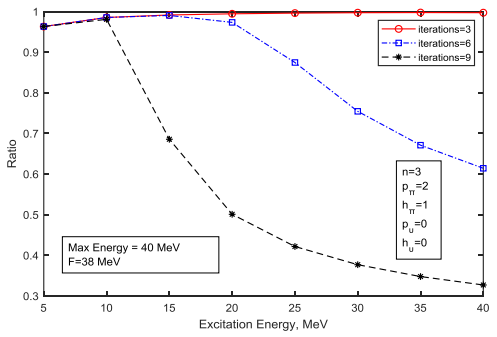

(a)

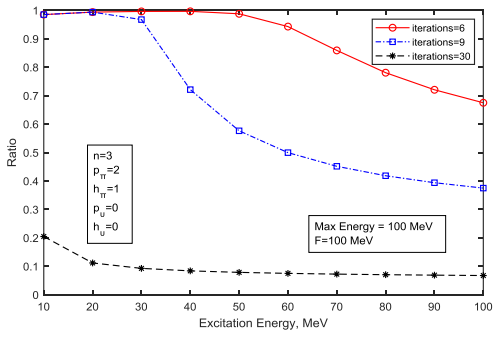

(b)

Fig. (1) Result of the ratio of Eq. (13) to modified Williams' formula in non-ESM, Eq. (14) for configuration (2,1,0,0). In both cases (a) and (b), d=13, g=A/d and for each example, the number of program iterations is shown, representing the maximum number of iterations before the computation program stops

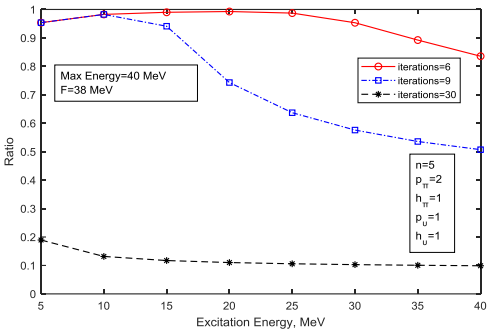

(a)

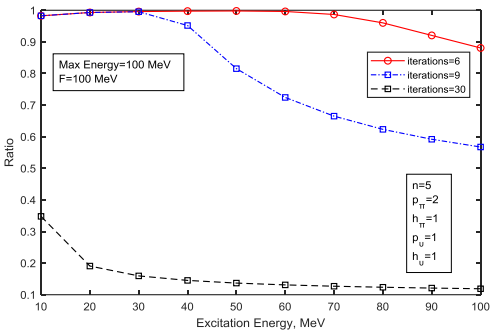

(b)

Fig. (2) Analogous to Fig. (1) but shows the configuration (2,1,1,1) instead

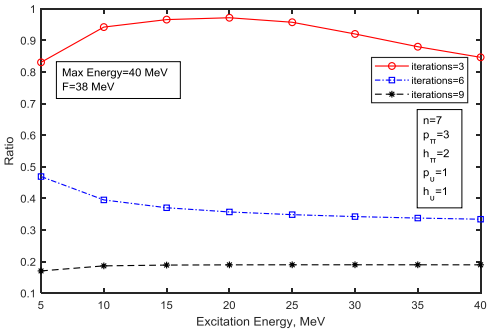

Fig. (3) Analogous to Fig. (1a) but shows the configuration (3,2,1,1) instead

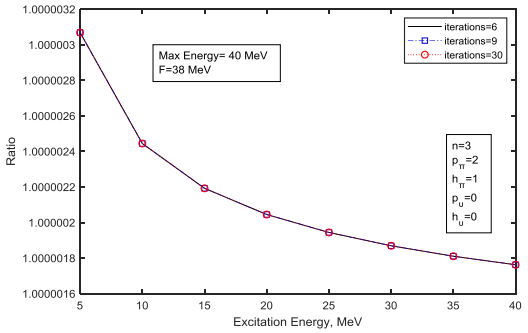

(a)

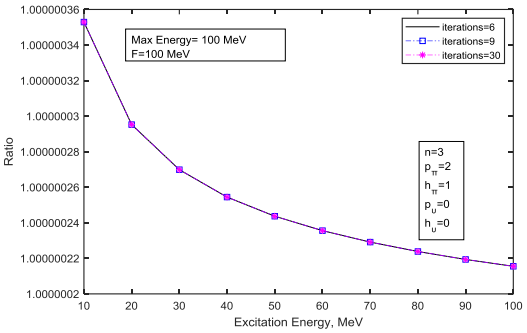

(b)

Fig. (4) Result of the ratio of Eq. (14), modified Williams' formula in non-ESM, to Eq. (3), modified Williams' formula in ESM, for configuration (2,1,0,0). In both cases (a) and (b), d=13, g=A/d and for each example, the number of program iterations is shown, representing the maximum number of iterations before the computation program stops

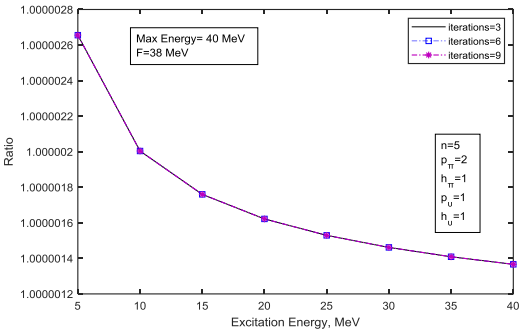

(a)

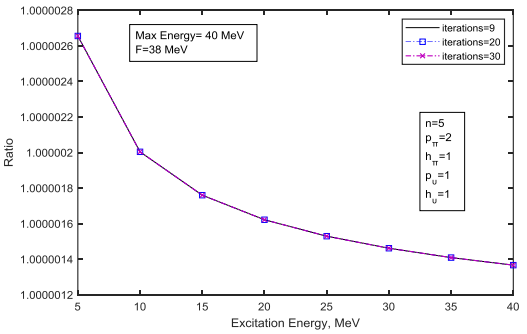

(b)

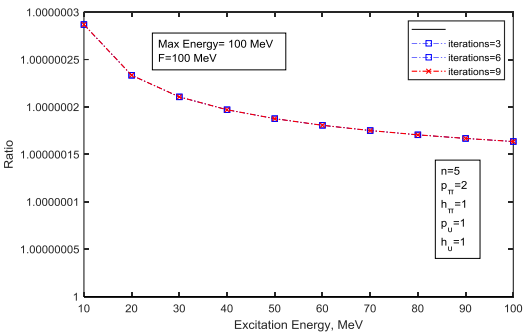

(c)

Fig. (5) Result of the ratio of Eq. (14), modified Williams' formula in non-ESM, to Eq. (3), modified Williams' formula in ESM, for configuration (2,1,1,1). In all cases (a), (b) and (c), d=13, g=A/d and for each example, the number of program iterations is shown, representing the maximum number of iterations before the computation program stops

 ISSN 1813-2065 (print) 2309-1673 (online)

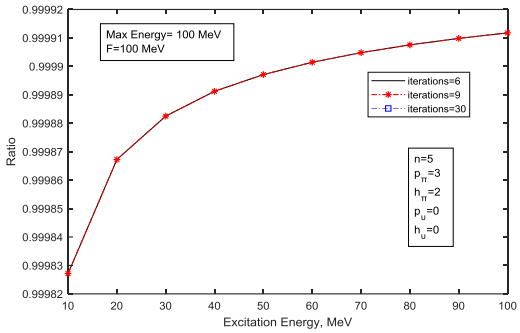

Fig. (6) Result of the ratio of Eq. (14), modified Williams' formula in non-ESM, to Eq. (3), modified Williams' formula in ESM, for configuration (3,2,0,0). In case F=100 MeV, d=13, g=A/d and for each example, the number of program iterations is shown, representing the maximum number of iterations before the computation program stops

6. Conclusion

It's important to point out how important this treatment is, since increasing the number of terms is a very important improvement for the State density calculation. By increasing the number of iterations, the state density results in the non-ESM approach were more precise and compatible with the results computed in the ESM approach. When pairing correction was implemented, it was discovered that the current non-ESM state density calculation formula would produce the best results when compared to the conventional approach. A further suggestion is to incorporate the effects of Fermi and binding energies for particles and holes, respectively. The analytical solution was found in Eq. (21), which shows how hard it can be to get a formula to behave in a way that makes more reasonable treatment. This suggests that non-ESM can be solved to improve system description, but it requires more calculation time and effort.

References

[1] S.S. Shakir and A.D. Salloum, "Investigation of the Appropriate Partial Level Density Formula for Pre-Equilibrium Nuclear Exciton Model", *J. Appl. Math. Phys.*, 1(3) (2013) 47.

[2] G.J. James, "Statistical Model of Intermediate Structure", *Phys. Rev. Lett.*, 17(9) (1966) 478.

[3] M. Avrigeanu and V. Avrigeanu, "Partial Level Densities for Nuclear Data Calculations", *Comp. Phys. Commun.*, 112(2-3) (1998) 191-226.

[4] S.A. Abdul-Razzaq, "Particle-Hole State Density Calculations with Non-Equidistant Spacing Model: I. Basic Derivation", *Iraqi J. Phys.*, 8(13) (2010) 53-64.

[5] E. Betak and P.E. Hodgson, "Particle-Hole State Densities in Pre-Equilibrium Nuclear Reaction Models", *Rep. Prog. Phys.*, 61(5) (1998) 483.

[6] B. Marshall, "Importance of the Nuclear Density Distribution on Pre-Equilibrium Decay", *Phys. Rev. Lett.*, 28(12) (1972) 757.

[7] B. Marshall, "Preequilibrium Decay", *Ann. Rev. Nucl. Sci.*, 25(1) (1975) 123-66.

[8] J. Williams and C. Frederick, "Particle-Hole State Density in the Uniform Spacing Model." *Nucl. Phys. A*, 166(2) (1971) 231-40.

[9] P. Obložinský, "Particle-Hole State Densities for Statistical Multi-Step Compound Reactions", *Nucl. Phys. A*, 453(1) (1986) 127-40.

[10] C.Y. Fu, "Implementation of on Advanced Pairing Correction for Particle-Hole State Densities in Precompound Nuclear Reaction Theory", *Nucl. Sci. Eng.*, 86(4) (1984) 344-54.

[11] C. Kalbach, "Improved Implementation of Pairing Corrections in Exciton Model Particle-Hole State Densities", *Nucl. Sci. Eng.*, 95(1) (1987) 70-78.

[12] C. Kalbach, "Surface Effects in Preequilibrium Reactions of Incident Neutrons", *Phys. Rev. C*, 69(1) (2004) 14605.

[13] C. Kalbach, "Surface Effects in the Exciton Model of Preequilibrium Nuclear Reactions", *Phys. Rev. C*, 32(4) (1985) 1157.

[14] C. Kalbach, "Two-Component Exciton Model: Basic Formalism Away from Shell Closures." *Phys. Rev. C*, 33(3) (1986) 818.

[15] E. Torleif, "The Statistical Model and Nuclear Level Densities", *Adv. in Phys.*, 9(36) (1960) 425-511.

[16] C. Kalbach, "Particle-Hole State Densities with Good Isospin", *Phys. Rev. C*, 47(2) (1993) 587.

[17] C. Kalbach, "Missing Final States and the Spectral Endpoint in Exciton Model Calculations", *Phys. Rev. C*, 73(2) (2006) 24614.

[18] G. Cecilia et al., "Inelastic Neutron Scattering from Carbon, Iron, Yttrium and Lead", *3rd Int. Workshop on Compound Nuclear Reactions and Related Topics, EPJ Web Conf.*, 21 (2012) 3004.

[19] H.M. Saleh and A.A. Selman, "Derivation a New Nuclear State Density Equation in a Two-Component Pre-Equilibrium Exciton Model with Non-Equidistant Spacing Model", submitted to *Solid State Phen.* (2022).

[20] A. Harangozo et al., "Particle-Hole State Densities with Nonequidistant Single-Particle Levels", *Phys. Rev. C*, 58(1) (1998) 295.

[21] A.S. Ahmed, "Neutron Induced Preequilibrium Nuclear Reactions Using the Exciton Model", Ph.D. thesis, University of Baghdad, Baghdad (Iraq, 2009).

7. Index

$$\omega^{\text{non-ESM}}(n,E)=\frac{g_0^n}{2^{n-1}\,\pi^{n/2}p_\pi!h_\pi!p_\upsilon!h_\upsilon!}\,\Xi\frac{(E-P_2(\Delta)-B_{p_\pi,h_\pi,p_\upsilon,h_\upsilon})^{N-1}}{F^{N-n}\,(N-1)!}\times\Theta\left(E-P_2(\Delta)-B_{p_\pi,h_\pi,p_\upsilon,h_\upsilon}\right)\quad(14)$$

where

$$\Xi=\sum_{a_1=0}^{\infty}\sum_{a_2=0}^{\infty}\cdots\sum_{a_{p_\pi}=0}^{\infty}\sum_{b_1=0}^{\infty}\sum_{b_2=0}^{\infty}\cdots\sum_{b_{h_\pi}=0}^{\infty}\quad\cdots$$

$$\sum_{c_1=0}^{\infty}\sum_{c_2=0}^{\infty}\cdots\sum_{c_{p_\nu}=0}^{\infty}\sum_{d_1=0}^{\infty}\sum_{d_2=0}^{\infty}\cdots\sum_{d_{h_\nu}=0}^{\infty}\prod_{k=1}^{p_\pi}C_{a_k}^{p_\pi}\prod_{j=1}^{h_\pi}C_{b_j}^{h_\pi}\times\prod_{\lambda=1}^{p_\nu}C_{c_\lambda}^{p_\nu}\times\prod_{\theta=1}^{h_\nu}C_{d_\theta}^{h_\nu}\quad(15)$$

and,

$$N=n+a_1+a_2+\cdots+a_{p_\pi}+b_1+b_2+\cdots+b_{h_\pi}+c_1+c_2+\cdots+c_{p_\nu}+d_1+d_2+\cdots+d_{h_\nu}$$

where $=p_\pi+h_\pi+p_\upsilon+h_\upsilon$, so

$$\therefore N=n+\sum_{i=1}^{p_\pi}a_i+\sum_{j=1}^{h_\pi}b_j+\sum_{k=1}^{p_\nu}c_k+\sum_{l=1}^{h_\nu}d_l\quad(16)$$

where $C_{m_i}^{p_\pi}, C_{m_j}^{h_\pi}, C_{m_k}^{p_\nu}, and\ C_{m_l}^{h_\nu}$ are coefficients of integrating the spatial functions of $P_\pi(k)$, $H_\pi(k), P_\nu(k)$, and $H_\nu(k)$, respectively, and $P_\pi(k)$, $H_\pi(k), P_\nu(k)$, and $H_\nu(k)$ Functions that represent part of the state density integration.

$$\sum_{a_1=0}^{\infty}\sum_{a_2=0}^{\infty}\cdots\sum_{a_{p_\pi}=0}^{\infty}\sum_{s_1=0}^{a_1}\sum_{s_2=0}^{a_2}\cdots\sum_{s_{p_\pi}=0}^{a_{p_\pi}}\sum_{b_1=0}^{\infty}\sum_{b_2=0}^{\infty}\cdots\sum_{b_{h_\pi}=0}^{\infty}\sum_{q_1=0}^{b_1}\sum_{q_2=0}^{b_2}\cdots$$

$$\sum_{q_{h_\pi}=0}^{b_{h_\pi}}\sum_{c_1=0}^{\infty}\sum_{c_2=0}^{\infty}\cdots\sum_{c_{p_\nu}=0}^{\infty}\sum_{u_1=0}^{c_1}\sum_{u_2=0}^{c_2}\cdots\sum_{u_{p_\nu}=0}^{c_{p_\nu}}\sum_{d_1=0}^{\infty}\sum_{d_2=0}^{\infty}\cdots\sum_{d_{h_\nu}=0}^{\infty}\sum_{v_1=0}^{d_1}\sum_{v_2=0}^{d_2}\cdots\sum_{v_{h_\nu}=0}^{d_{h_\nu}}\prod_{j=1}^{p_\pi}C_{a_j}^{p_\pi}$$

$$\prod_{\lambda=1}^{h_\pi}C_{b_\lambda}^{h_\pi}\times\prod_{\theta=1}^{p_\nu}C_{c_\theta}^{p_\nu}\times\prod_{y=1}^{h_\nu}C_{d_y}^{h_\nu}$$

$$\sum_{\ell=0}^{p_\pi}\sum_{r=0}^{h_\pi}\sum_{t=0}^{p_\nu}\sum_{m=0}^{h_\nu}(-1)^{l+r+t+m}\binom{p_\pi}{\ell}\binom{h_\pi}{r}\binom{p_\nu}{t}\binom{h_\nu}{m}$$

$$\frac{(B)^{\sum_{j=1}^{p_\pi}\ell s_j-\sum_{\theta=1}^{p_\nu}tu_\theta}\,(F)^{\sum_{\lambda=1}^{h_\pi}r\,c_\lambda-\sum_{j=1}^{p_\pi}a_j-\sum_{\lambda=1}^{h_\pi}b_\lambda+\sum_{\theta=1}^{p_\nu}c_\theta-\sum_{y=1}^{h_\nu}d_y+mv_y}}{\left[\prod_{j=1}^{p_\pi}(s_j)!\right]^{\ell}\left[\prod_{\lambda=1}^{h_\pi}(q_\lambda)!\right]^{r}\left[\prod_{\theta=1}^{p_\nu}(u_\theta)!\right]^{t}\left[\prod_{y=1}^{h_\nu}(v_y)!\right]^{m}}\times\frac{(E-\ell B-rF-tB-mF)^{N-1}}{(N-1)!}\quad(21)$$

$$\Xi=\sum_{a_1=0}^{\infty}\sum_{a_2=0}^{\infty}\cdots\sum_{a_{p_\pi}=0}^{\infty}\sum_{s_1=0}^{a_1}\sum_{s_2=0}^{a_2}\cdots\sum_{s_{p_\pi}=0}^{a_{p_\pi}}\sum_{b_1=0}^{\infty}\sum_{b_2=0}^{\infty}\cdots\sum_{b_{h_\pi}=0}^{\infty}\sum_{q_1=0}^{b_1}\sum_{q_2=0}^{b_2}\cdots$$

$$\sum_{q_{h_\pi}=0}^{b_{h_\pi}}\sum_{c_1=0}^{\infty}\sum_{c_2=0}^{\infty}\cdots\sum_{c_{p_\nu}=0}^{\infty}\sum_{u_1=0}^{c_1}\sum_{u_2=0}^{c_2}\cdots\sum_{u_{p_\nu}=0}^{c_{p_\nu}}\sum_{d_1=0}^{\infty}\sum_{d_2=0}^{\infty}\cdots\sum_{d_{h_\nu}=0}^{\infty}\sum_{v_1=0}^{d_1}\sum_{v_2=0}^{d_2}\cdots\sum_{v_{h_\nu}=0}^{d_{h_\nu}}\prod_{j=1}^{p_\pi}C_{a_j}^{p_\pi}$$

$$\prod_{\lambda=1}^{h_\pi}C_{b_\lambda}^{h_\pi}\times\prod_{\theta=1}^{p_\nu}C_{c_\theta}^{p_\nu}\times\prod_{y=1}^{h_\nu}C_{d_y}^{h_\nu}\sum_{\ell=0}^{p_\pi}\sum_{r=0}^{h_\pi}\sum_{t=0}^{p_\nu}\sum_{m=0}^{h_\nu}(-1)^{l+r+t+m}\quad(22)$$

and

$$\therefore N=n+\sum_{j=1}^{p_\pi}(a_j-\ell s_j)+\sum_{\lambda=1}^{h_\pi}(b_\lambda-rq_\lambda)+\sum_{\theta=1}^{p_\nu}(c_\theta-tu_\theta)+\sum_{y=1}^{h_\nu}(d_y-mv_y)\quad(23)$$

 ISSN 1813-2065 (print) 2309-1673 (online)

IRAQI JOURNAL OF APPLIED PHYSICS
Volume 19, Issue 2, April-June 2023, 21-26

Proceedings of the 3rd International Scientific Conference and 5th Scientific Conference, organized by
College of Science, University of Tikrit, Tikrit, Iraq (28-29 December 2022)

Effect of Plasma Exposure Time on Structural Characteristics of Copper Acetyl-acetonite Films Prepared by Thermal Evaporation

Abdulqader M. Mahmoud[1]
Shareef F.S. Al-tikrity[1]
Mohammad K. Khalaf[2]

[1] *Department of Physics, College of Science, University of Tikrit, Tikrit, IRAQ*
[2] *Ministry of Science And Technology, Baghdad, IRAQ*

In this paper, the effect of exposure to oxygen plasma on the structural and morphological properties of copper(II) acetyl-acetonite thin films deposited by thermal evaporation technique was studied. Where thin films of thickness (200 nm) were exposed to oxygen plasma for different periods (10, 20 and 30 minutes). The structural characteristics of the samples and the effect of plasma exposure on structure and roughness were measured by XRD and AFM. As a result of treating the thin films with plasma, the crystalline size changed from 5.3 to 10.84 nm. The FE-SEM and EDX results, showing larger particles size range from 101.27 to 76.89 nm, and there is a decrease in particle size with increasing plasma exposure. A good improvement in surface roughness was obtained when the sample was treated with plasma for 10 min, but for longer exposure time, deformation occurs in the film surface as a result of etching effect on the surface.

Keywords: Metal composites; $C_{10}H_{14}CuO_4$; Thermal evaporation; Electrical properties
Received: 25 November 2022; **Revised:** 29 November 2022; **Accepted:** 05 December 2022

1. Introduction

The study of thin films is one of the most important topics that caught the attention of many scientists because of that its importance in many fields in the manufacture of electronic, optical devices and solar cells [1]. The interest of researchers in developing or finding new methods for preparing these films has increased, such as (evaporation, chemical decomposition, sputtering technology, and others) [2]. Organic materials have received grow attention during the past few years because of their various applications in the field of microelectronics, integrated circuits and optoelectronic devices [3]. These materials interact effectively under light due to a high oscillatory strength, and these optical properties may be significantly modified by their environment [1]. Acetyl-acetonite is one of the organic materials used in optoelectronics as it is a promising class of the β-diketones family because such compounds are important components for a wide range of electronic applications such as perovskite solar cells, polymer solar cells, integrated circuits, and microelectronics technology [4-8].

There are several techniques for treating the surface of organic films to become more effective in electronic applications, such as chemical etching, electron beam, ion beam and plasma treatments [9-13]. Plasma treatment is one of the most effective methods for surface modification and is used to fabricate a wide range of materials that can be considered as good candidates for the next generation of high-efficiency solar cells [14]. Also, to manufacture these thin films of organic materials requires techniques, including the thermal evaporation technique used in this study, and these techniques are not without defects, as it was found that one of the most defects of this mechanism are the presence a various defect and a roughness on exterior surface of sample [15,16]. But recently surface treatment technology has made progress in the field of material processing by modifying surface properties, control its energy and improve adhesion to the surface [17-24].

The aim of this research is to use oxygen plasma to modify the surface of copper(II) acetyl-acetonite ($Cu(acac)_2$) films and to investigate the effect of plasma treatment on the structural properties and surface morphology of the films prepared at different time periods. This work also aims to determine the optimum treatment time and to improve the structural properties of the sample surface throughout studying their structural and surface properties before and after treatment with plasma.

from the evaporation source, which was the optimum distance. After the pressure inside the evaporation chamber reaches $3x10^{-5}$ mbar, the material is evaporated with a deposition time of 172s. Then, after completing the deposition process, the samples are left in the evaporation chamber until their temperature reaches room temperature in order to ensure the completion of the crystallization process and to prevent the prepared samples from cracking or cracks as a result of sudden cooling. In this work, films were deposited on borosilicate glass substrates with a thickness of 1 mm and dimensions of 2.6x7.6cm. They were cut into four equal pieces to deposit the films on them.

2- The film thickness was measured in this work using optical interferometry using a 632.8nm He-Ne laser, using the following formula [26,27]:

$$t = \frac{\lambda}{2}\frac{\Delta x}{x} \qquad (2)$$

where t is the film thickness, Δx is the distance between consecutive sides, and λ is the laser wavelength

Modification of $Cu(acac)_2$ thin film surfaces is achieved by treating it with dc glow-discharge plasma with O_2 gas. The $Cu(acac)_2$ samples were cut into small slices with dimensions of 2x1cm for plasma treatment. The samples were then placed inside a chamber while maintaining a vacuum of 0.01 mbar using a rotary pump. Samples were placed on a glass substrates and placed at a distance of 2.5cm from the cathode. The plasma treatment time was changed within 10-30 min.

3. Results and Discussion

The structural characteristics of the prepared samples were determined by the XRD patterns to measure their crystalline structure under standard atmospheric conditions. The XRD patterns were obtained using a SHIMADZU-6000 XRD instrument with Cu-kα radiation (1.54056Å) and 40kV operation voltage.

Experimental data of XRD showed that the prepared $Cu(acac)_2$ films were of triclinic crystal structure and no unknown phase was found. The characteristic predominant orientation was in the directions (310) for all prepared films of the same thickness and for all plasma treatment times, as in Fig. (2). This is consistent with reference [27]. When comparing the results obtained from the interlayer distance (d_{hkl}) and the crystal diffraction angles corresponding to the locations of the characteristic peaks of the prepared films, as stated by the values in the ASTM card no. 13395-16-9 [28], where it showed a high degree of crystallization with a change in crystallite size from 5.3 to 10.84nm as a result of treating the thin film with plasma at different periods of time. The crystallite size of a 200nm-thick film was 10.84nm and began to decrease gradually after increasing the plasma treatment time. The crystallite size (D) was studied by using the Debye-Scherrer equation as follows:

2. Experimental Part

Thin films were prepared from $Cu(acac)_2$, which has a molecular weight of 263.78 g/mol, purity of 97%, and chemical composition of $C_{10}H_{14}CuO_4$, as shown in Fig. (1). $Cu(acac)_2$ is a bright blue solid that is soluble in water. The single crystals of this compound show the unusual property of being highly flexible, which allows the formation of knots. The flexibility is attributed to the nature of the forces between the molecules. Whereas, the transition-metal $Cu(acac)_2$ complexes are important components for many devices like solar cells, optoelectronics and integrated circuits [7,27]. The $Cu(acac)_2$ thin films were deposited on glass substrates by thermal evaporation in vacuum, which is considered one of the best methods to prepare such samples because it has own advantages over other deposition methods and techniques as no possibility of chemical contamination inside deposition chamber. This is a consequence of the relatively high degree of vacuum ($3x10^{-5}$ to $1.1x10^{-5}$ mbar) during the deposition process. The evaporation chamber was evacuated from dust particles and oxygen gas in order to prevent oxidation of the interacting materials [25-27].

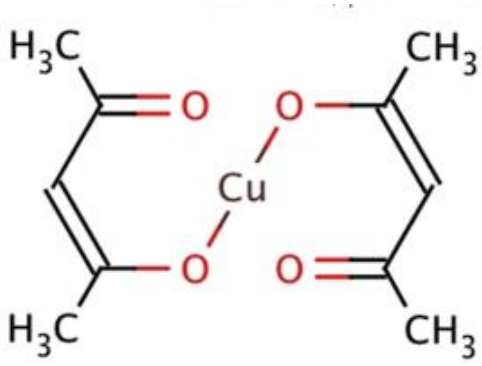

Figure (1) The chemical structure of $Cu(acac)_2$

The $Cu(acac)_2$ thin films were prepared via two main stages:

1- Calculating the weight of the material using a Precisa electronic balance with a very sensitive range (10^{-4} mg) to determine the amount to be deposited to obtain the weight equivalent to the required thickness of the film (200nm) using the following mathematical formula [26,27]:

$$d = \frac{m}{2\pi R^2 \rho} \qquad (1)$$

where d is the film thickness, m is the mass of material, R is the distance between the vaporizer and sample holder, and ρ is the density of the substance, which is 0.721 g/cm^3

Then the weight of each thickness was placed in a pot of tungsten metal at a depth of 3mm. As the pots were fixed in the sample holder, and after several attempts to change the vertical distance between the evaporation source and sample holder to obtain greater adhesion force and better homogeneity of the formed thin film, the holder was also installed at a vertical distance of 30cm away

 ISSN 1813-2065 (print) 2309-1673 (online)

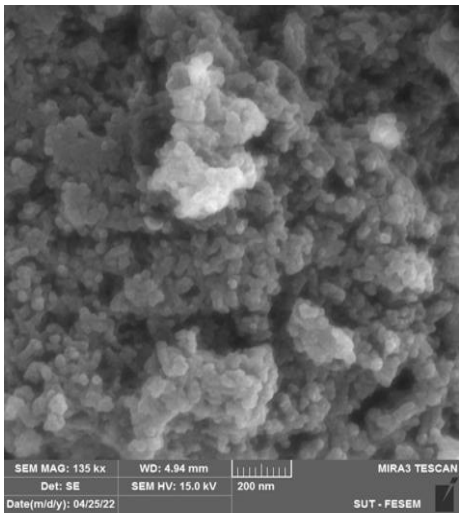

(a)

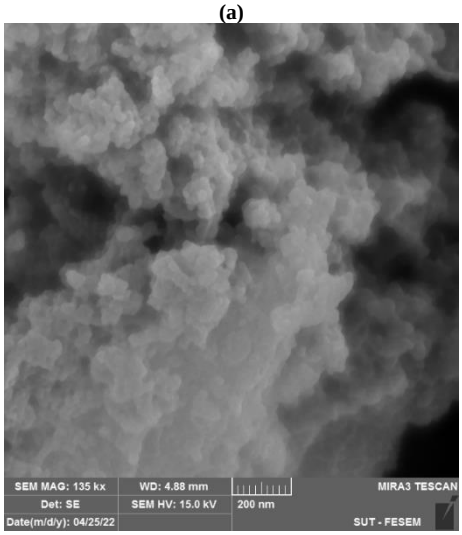

(b)

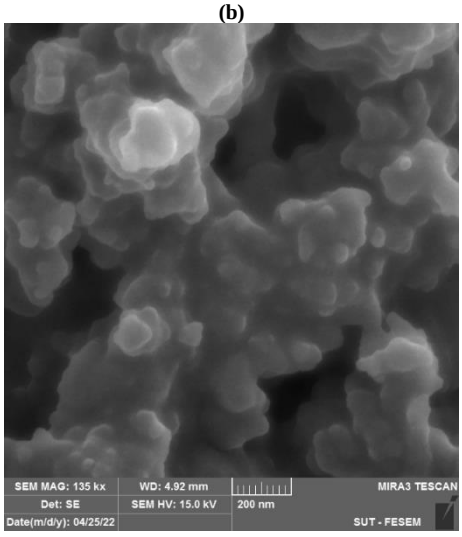

(c)

$$D = \frac{K\lambda}{\beta cos\theta} \quad (3)$$

where β is the full-width at half maximum (FWHM), λ is the x-ray wavelength (1.5406Å), θ is Bragg's angle

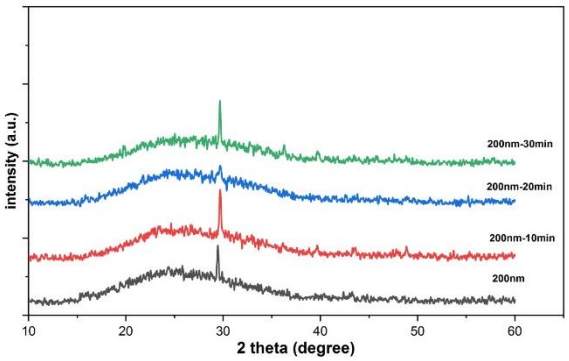

Fig. (2). XRD patterns of $Cu(acac)_2$ thin films (a) before plasma treatment, (b) after 10 min plasma exposure, (c) after 20 min and (d) after 30 min

The microscopic strain (ε) of the samples was also measured by Eq. (4) [26,27,29] and a gradual change was observed, where the maximum value of the strain at 200nm thickness was 7.058nm and it started to decrease to reach 5.721nm at the same thickness, but with a time period of 30min:

$$\varepsilon = \frac{\beta}{4tan\theta} \quad (4)$$

Table (1) shows the most important results obtained from the analysis and interpretation of XRD patterns for 200nm-thick $Cu(acac)_2$ films treated with plasma for different periods.

Table (1) Results obtained from XRD patterns of $Cu(acac)_2$ films of the same thickness and treated with plasma for different periods

Sample	2θ (deg)	FWHM (deg)	d (Å)	Crystallite Size C.S. (nm)	Microstrain (ε)	Grain Size G.S. (nm)
200nm	21.751	4.447	4.133	10.84	7.058	101.27
200nm/10min	24.751	3.843	4.117	8.67	6.800	94.39
200nm/20min	28.387	3.336	3.248	6.87	6.222	83.54
200nm/30min	31.840	2.715	2.795	5.3	5.721	76.89

As shown in this part, a TESCAN FE-SEM instrument was used to provide much more accurate information about the surface shape and chemical composition of the sample. By analyzing the FE-SEM images of the film deposited on quartz glass substrate, as shown in Fig. (3), larger particles ranging within 101.27-76.89nm are observed. A decrease in the particle size is observed with increasing the plasma processing time, as this is consistent with the measurements of XRD and AFM, so the particle size is larger than the crystallite size.

prepared films. Figure (5b) shows the 3D topography of the $Cu(acac)_2$ thin film surface. A decrease in particle size is observed when the thin film is exposed to plasma for 10 min, while increasing the exposure time for longer than 10 min leads to the transformation of the thin film surface from crystalline form to amorphous, as shown in Fig. (5c). This result agrees to the result of XRD.

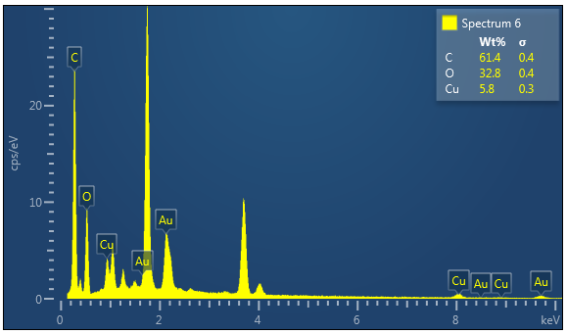

Element	Line Type	Wt.%	Wt.% Sigma	Atomic %
C	K series	64.31	0.47	72.67
O	K series	31.05	0.42	26.34
Cu	L series	4.65	0.38	0.99
Total:		100.00		100.00

(a)

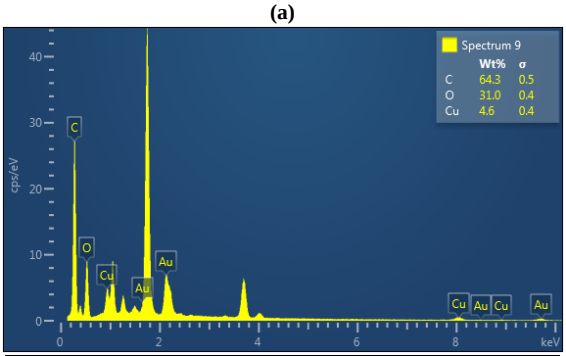

Element	Line Type	Wt.%	Wt.% Sigma	Atomic %
C	K series	61.40	0.44	70.47
O	K series	32.82	0.40	28.28
Cu	L series	5.79	0.34	1.26
Total:		100.00		100.00

(b)

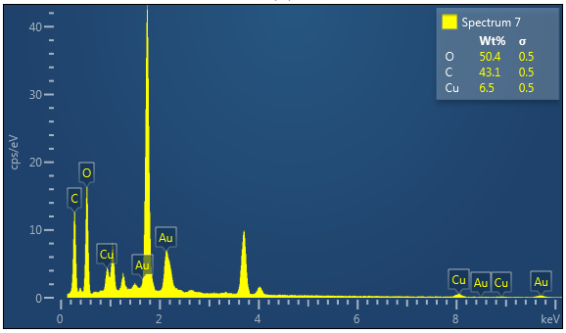

Element	Line Type	Wt.%	Wt.% Sigma	Atomic %
C	K series	43.07	0.49	52.44
O	K series	50.40	0.50	46.06
Cu	L series	6.53	0.48	1.50
Total:		100.00		100.00

(c)

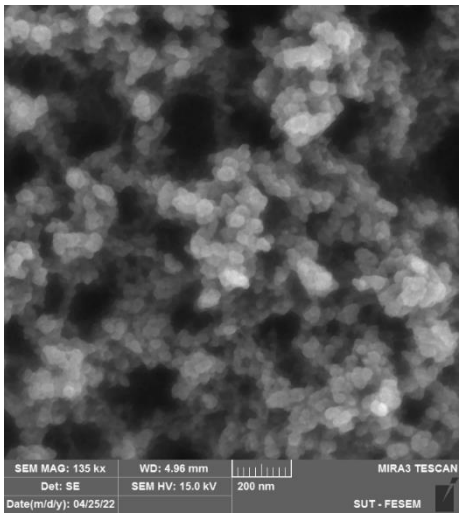

(d)

Fig. (3) FE-SEM images of $Cu(acac)_2$ (a) 200nm-thick thin film, (b) 200nm-thick film after 10min treatment, (c) 200nm-thick film after 20min treatment, and (d) 200nm-thick film after 30min treatment

Energy-dispersive x-ray (EDS) spectroscopy is employed to provide the elemental analysis of the prepared samples, which includes the composition of the deposited film and fractional amounts of the constituents, as well as to explore deformations in the produced sample. The chemical composition ($C_{10}H_{14}CuO_4$) of the prepared samples was confirmed as shown in Fig. (4). The molecular weight percentages of the oxygen (O), carbon (C), and copper (Cu) can be seen on the EDX spectra. For the 200nm-thick thin film, the amount of O, C and Cu were 31.05, 64.31 and 4.65%, respectively, while for the sample of the same thickness but treated with plasma for 10min, the values were 32.82, 61.40 and 5.79%, respectively. A significant increase in the oxygen and carbon contents can be observed while the content of copper is decreased. For the film treated with plasma for 20min, the values were 50.40, 43.07 and 6.53%, respectively. When increasing the plasma exposure time to 30min, it was noted that the values of the elements were 31.74, 61.07 and 7.18%. From these results, an increase in copper content and a decrease in carbon content were concluded as a result of the reaction between the oxygen-plasma and film surface. This is consistent with the AFM results showing slight surface roughness with a densely packed microstructure devoid of cracks. Thus, the surface roughness decreases with smoothing causing an increase in the exposure time and the surface becomes smoother.

Atomic force microscopy (AFM) is one of the most widely used and effective tools for determining surface shape, roughness, thickness and topography. The main advantage of the atomic force microscope is its sub-nanometer resolution and ability to provide an accurate image of the real surface space. An Angstrom AA3000 SPM, NSC35/AIBS tip instrument was used to preform the AFM for the

 ISSN 1813-2065 (print) 2309-1673 (online)

A good improvement in surface roughness was also obtained when the film surface is exposed to plasma for 10 min due to re-crystallization of the $Cu(acac)_2$ compound or removing some surface layers [30]. Thin-film surface density increases with decreasing crystal size, and thus the thin-film surface becomes smoother [31-33]. A little growth of more roughness parameter values was also noted when exposure time reached 30 min, which means that long exposure time would cause erosion to the thin film surface. These results suggest that when the film surface is exposed to oxygen plasma for a period of time between 0 and 20 min, the etching process prevails, but when the exposure time is increased to 30 min, the etching process is dominated as aresult of the decomposition, as shown in Fig. (5d). The roughness was decreased from 25 to 10nm when the exposure time is increased to 30 min. Finally, it can be assumed that the film surface was dominated by the crystalline structure before treatment with plasma, but when it was exposed to the plasma for a time period ranging in 10-20 min, this surface turns into amorphous with some improvements that occur on the thin film. With further increase in exposure time, the film surface will be deformed due to etching process occurring on this surface.

4. Conclusions

Copper acetyl-acetone nanostructured thin films were successfully synthesized by thermal evaporation technique. As these films were exposed to oxygen plasma for different periods, they showed clear changes in their structural characteristics. There was an improvement in the crystalline structure of the thin film as well as decrease in the crystallite size. The surface roughness of the thin film was reduced when exposed to plasma for longer times and this leads to change the crystalline structure into amorphous. An obvious decrease in the surface roughness of the deposited thin films was observed when these films were exposed to plasma for longer periods after which etching prevails on the surface. These results can be used in many electronic applications, optoelectronics and solar cells.

References

[1] J.R. Tischler et al., "Solid state cavity QED: Strong coupling in organic thin films", Org. Electron., 8(2-3) (2007) 94-113.

[2] H.H. Wang et al., "Improving the TiO_2 electron transport layer in perovskite solar cells using acetylacetonate-based additives", J. Mater. Chem. A, 3(17) (2015) 9108-9115.

[3] A.R. bin Mohd Yusoff, M.A.M. Teridi and J. Jang, "Null current hysteresis for acetylacetonate electron extraction layer in perovskite solar cells", Nanoscale, 8(12) (2016) 6328-6334.

[4] W. Chen et al., "Metal acetylacetonate series in interface engineering for full low-temperature-processed, high-performance, and stable planar perovskite solar cells with conversion efficiency over

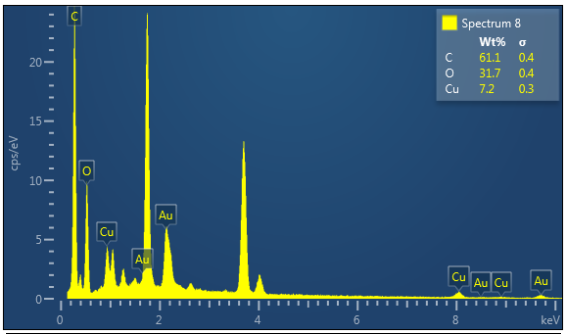

Element	Line Type	Wt.%	Wt.% Sigma	Atomic %
C	K series	61.07	0.41	70.80
O	K series	31.74	0.38	27.63
Cu	L series	7.18	0.31	1.57
Total:		100.00		100.00

(d)

Fig. (4) EDX spectra of $Cu(acac)_2$ (a) 200nm-thick thin film, (b) 200nm-thick film after 10min treatment, (c) 200nm-thick film after 20min treatment, and (d) 200nm-thick film after 30min treatment

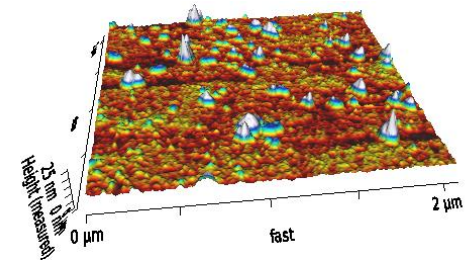

(a)

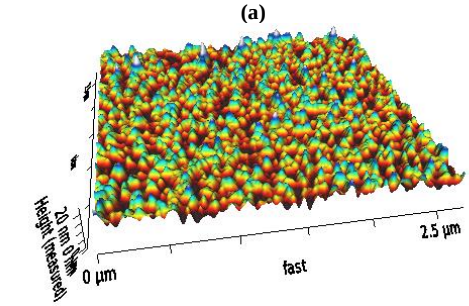

(b)

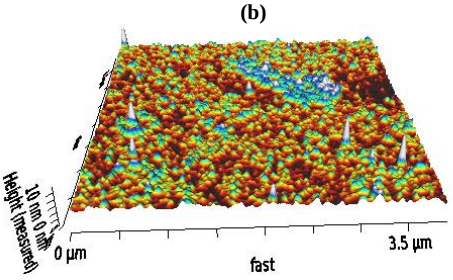

(c)

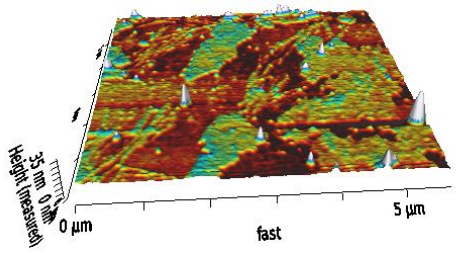

(d)

Fig. (5) AFM images of $Cu(acac)_2$ (a) 200nm-thick film, (b) 200nm-thick film after 10min treatment, (c) 200nm-thick film after 20min treatment, and (d) 200nm-thick film after 30min treatment

[19] C.V. Ramana et al., "Enhanced optical constants of nanocrystalline yttrium oxide thin films", Appl. Phys. Lett., 98(3) (2011) 031905.
[20] V.H. Mudavakkat et al., "Structure, morphology and optical properties of nanocrystalline yttrium oxide (Y_2O_3) thin films" Opt. Mater., 34(5) (2012) 893-900.
[21] B.A. Park et al., "MWIR HgCdTe Photodiodes based on high-density plasma-induced type conversion", Semicond. Sci. Technol., 23(9) (2008) 095027.
[22] S.G. Wang et al., "Performance improvement of polycrystalline diamond ultraviolet photodetectors by room-temperature plasma treatment", Appl. Phys. Lett., 86(9) (2005) 093503.
[23] Q. Liu et al., "Oxygen Plasma Surface Activation of Electron-Depleted ZnO Nanoparticle Films for Performance-Enhanced Ultraviolet Photodetectors", phys. stat. sol. (a), 214(11) (2017) 1700176.
[24] S. Ikeda, E. Higurashi and T. Suga, "Influence of atmospheric-pressure plasma treatment on surface and electrical properties of photodiode chips", in 2015 Int. Conf. Electron. Pack. and iMAPS All Asia Conf. (ICEP-IAAC) (2015) 666-669.
[25] P. Joseph, C. Charles and J. Igor, **"Pump Handbook"**, 3rd ed., McGraw-Hill (NY, 2001).
[26] R.R. Jawad, "Studying the optical and structural properties of cadmium oxide (CdO) prepared by thermal evaporation method", MSc thesis, Tikrit University (2019).
[27] H. Abdel-Khalek, M.I. El-Samahi and A.M. El-Mahalawy, "Influence of post-deposition annealing on structural, morphological and optical properties of copper (II) acetylacetonate thin films", Spectrochimica Acta Pt. A: Mol. Biomol. Spectro., 202 (2018) 389-400.
[28] A.M. Vernice et al., **"Annual Book of ASTM Standards"**, ASTM Int. (2014), ISBN 978-1-6220-4661-4.
[29] K.K. Nagaraja et al., "Effect of annealing on the structural and nonlinear optical properties of ZnO thin films under cw regime", J. Phys. D: Appl. Phys., 46(5) (2013) 055106.
[30] K.N. Pandiyaraj et al., "Effect of cold atmospheric pressure plasma gas composition on the surface and cyto-compatible properties of low density polyethylene (LDPE) films", Curr. Appl. Phys., 16(7) (2016) 784-792.
[31] T.S. Tripathi et al., "Atomic layer deposition of copper metal films from $Cu(acac)_2$ and hydroquinone reductant", Adv. Eng. Mater., 23(10) (2021) 2100446.
[32] S. Chopra et al., "Effect of annealing temperature on microstructure of chemically deposited calcium modified lead titanate thin films", Appl. Surf. Sci., 230(1-4) (2004) 207-214.
[33] C.T. Chen and B.S. Chiou, "The effects of surface-plasma treatment of thin-film hydrogen silesquioxane low k dielectric", J. Mater. Sci.: Materials in Electronics, 15(3) (2004) 139-143.
16% on 1 cm^2 scale", Adv. Mater., 29(16) (2017) 1603923.
[5] W. Chen et al., "Ruthenium acetylacetonate in interface engineering for high performance planar hybrid perovskite solar cells", Opt. Exp., 25(8) (2017) A253-A263.
[6] W. Sun et al., "High-performance inverted planar heterojunction perovskite solar cells based on a solution-processed CuO_x hole transport layer", Nanoscale, 8(20) (2016) 10806-10813.
[7] B. Mustafa et al., "Solution processed nickel oxide anodes for organic photovoltaic devices", Appl. Phys. Lett., 104(6) (2014) 29-1.
[8] A.A. Dakhel and A.Y. Ali-Mohamed, "Dielectric properties of bis (2, 4 pentanedionato) copper (II) crystalline films grown on Si substrate for low-k applications", J. Non-cryst. Solids, 355(22-23) (2009) 1264-1268.
[9] J. Abenojar et al., "Surface modifications of polycarbonate (PC) and acrylonitrile butadiene styrene (ABS) copolymer by treatment with atmospheric plasma", Surf. Coat. Technol., 203(16) (2009) 2173-2180.
[10] N. Encinas et al., "Extreme durability of wettability changes on polyolefin surfaces by atmospheric pressure plasma torch", Surf. Coat. Technol., 205(2) (2010) 396-402.
[11] Y. Martin, D. Boutin and P. Vermette, "Study of the effect of process parameters for n-heptylamine plasma polymerization on final layer properties", Thin solid films, 515(17) (2007) 6844-6852.
[12] H. Kaczmarek, "Surface modification of thin polymeric films by air-plasma or UV-irradiation", Surf. Sci., 507 (2002) 883-888.
[13] J.S. Kim, Y.K. Kim and K.H. Lee, "Effects of atmospheric plasma treatment on the interfacial characteristics of ethylene–vinyl acetate/polyurethane composites", J. Colloid Interface Sci., 271(1) (2004) 187-191.
[14] P.S. Arinda et al., "The characteristics of surface morphology on the polystyrene thin film using DC-bias oxygen plasma treatment", in AIP Conf. Proc., 2391(1) (2022) 070015.
[15] M.A. Lieberman and A.J. Lichtenberg, **"Principles of Plasma Discharges and Materials Processing"**. John-Wiley & Sons (2005) ISBN 0-471-72001-1.
[16] H.J. Ramos, J.L.C. Monasterial and G.Q. Blantocas, "Effect of low energy ion beam irradiation on wettability of narra (Pterocarpus indicus) wood chips", Nucl. Instrum. Meth. in Phys. Res. Sec. B: Beam Interactions with Materials and Atoms, 242(1-2) (2006) 41-44.
[17] C.V. Ramana et al., "Structure and chemical properties of molybdenum oxide thin films", J. Vac. Sci. Technol. A: Vac. Surf. Films, 25(4) (2007) 1166-1171.
[18] V.V. Atuchin et al., "Surface crystallography and electronic structure of potassium yttrium tungstate", J. Appl. Phys., 104(3) (2008) 033518.

 ISSN 1813-2065 (print) 2309-1673 (online)

IRAQI JOURNAL OF APPLIED PHYSICS
Volume 19, Issue 2, April-June 2023, 27-32

Proceedings of the 3rd International Scientific Conference and 5th Scientific Conference, organized by College of Science, University of Tikrit, Tikrit, Iraq (28-29 December 2022)

Study of Thermal Effect on Physical Properties of PEG8000/TiO_2 Composite Using Positron Annihilation Lifetime Spectroscopy

Rana Yasin
Saygin Kuzeci

Department of Physics, College of Education for Pure Science, Kirkuk University, Kirkuk, IRAQ

In this study, organic-inorganic mixtures were investigated by positron annihilation lifetime spectroscopy (PALS). This study aims to determine the physical properties and glass transition temperatures of TiO_2/PEG8000 composites, where TiO_2 is used as a filler with weight contents of 0-5%. After mixing the homogeneous PEG8000 and PEG8000/TiO_2 composites well, they were kept under 10 bar pressure for 5 minutes and prepared as a capsule-shaped tablets to measure the free volume as a function of temperature. On the other hand, by using Simha-Somcynsky (SS) lattice hole theory, free volume and free volume fraction were obtained at the temperatures up to 473K as used in the experimental study. The ortho-positronium lifetime and ortho-positronium intensity play an important role in PALS technique and the constant C of $(5.2\pm0.2)\times10^{-3}$ Å^{-3} was found by plotting the free volume values obtained from experimental and theoretical studies. The glass transition temperatures obtained by the PALS study are compatible with differential scanning calorimetry (DSC).

Keywords: Macromolecules; Composites; Positron annihilation; Titanium dioxide
Received: 25 November 2022; **Revised:** 14 December 2022; **Accepted:** 15 December 2022

1. Introduction

The inorganic-organic composite materials, consisting of mixtures, represent a widely researched area [1]. It is important to extract the properties of these composite materials, such as the flexibility of the polymer, the processability, high thermal, glassy temperature, and local stability about the polymer structure and composites. The polyethylene glycol studied in this study has a wide and widespread usage area. Polyethyleneglycol is a moderately resistant material with amorphous structure and thermoplastic properties. The polymer matrix generally has low refractive indices. In order to improve and increase the refractive indices, titanium dioxide (TiO_2) has been used as an inorganic filling material [2] to synthesize PEG8000/TiO_2 composites by using different amounts of TiO_2 [1-9].

As an inorganic filler, TiO_2 can cause a change in the free volume and free volume fraction or hole fraction of the polymer matrix [10]. Therefore, it is important to determine the free volume and hole fraction in the polymer matrix. The free volume theory, which examines the polymer material structure, was put forward by Simha-Somcynsky. It gives information about viscosity, phase transition, glass transition temperature and thermodynamic properties. Bamford et al. [11] and Cohen et al. [12] have interpreted the structural and dislocation defects of amorphous polymers materials due to free volume. As another unique technique, positron annihilation lifetime spectroscopy (PALS) system is a unique tool used to probe the holes and measure the defects in polymer matrix [13]. The sizes of free volume and hole fraction are measured by ortho-positronium (o-Ps) lifetime (τ_3) and ortho-positronium intensity (I_3), which is very sensitive to free volume and hole fraction sizes and densities. PALS measures free volume and hole fraction with matter disturbances and causes no damage to the polymer structure, so, it is a unique non-destructive examination technique.

In this study, PEG8000/TiO_2 composites were prepared by mixing 1g of PEG8000 with different weight amounts (10, 25 and 50 mg) of TiO_2. They were mixed thoroughly and encapsulated under 10 bar pressure. The aim of this study is to extract the structural free volume size and physical properties of the prepared PEG8000/TiO_2 composites by using the PALS techniques. These composite samples with different weights of TiO_2 were examined by PALS system to obtain information about the change profile between the holes fraction and free volume sizes. The Schrödinger equation has been used in polar spherical coordinates to obtain the ortho-positronium wave function and then extracted the relationship between

ortho-positronium annihilation velocity rate and free volume radius by ortho-positronium wave function as in below

$$\lambda_{pick-off}(ns^{-1}) = 2\left[1-\frac{R}{R_o}+\frac{1}{2\pi}\sin\left(\frac{2\pi R}{R_o}\right)\right] \quad (1)$$

The inverse of the ortho-positronium annihilation velocity rate is given by the ortho-positronium lifetime as

$$\tau_3(o-Ps) = \frac{1}{2}\left[1-\frac{R}{R_o}+\frac{1}{2\pi}\sin\left(\frac{2\pi R}{R_o}\right)\right]^{-1} \quad (2)$$

Ortho-positronium lifetime spectroscopy is relative to the radius (R) of the free volume as shown in the last equation above. So, the free volume could be obtain from the following formula

$$<\upsilon_f(\tau_3)>= 4\pi R^3/3 \quad (3)$$

where $<\upsilon_f(\tau_3)>$ is the average free volume size

The mean free volume size is extracted by ortho-positronium lifetime spectroscopy when multiplied by the ortho-positronium intensity to get the free volume fraction ratio as follows

$$f_v = CI_3\upsilon_f(\tau_3) \quad (4)$$

Here *C* is a constant. In order to obtain the value of *C*, the theoretical free volume fraction was obtained by using the SS theory and the experimental free volume fraction has been obtained by using the ortho-positronium technique in the PALS system. Then the value of *C* is obtained by fitting the graphs of theoretical free volume fraction data with experimental free volume fraction data.

2. Experimental Part

The measurements of the PALS technique were related to the experimental details of the positron technique. The positron source was prepared by dropping 25 μCi of ^{22}NaCl (in solution) onto the foil consisting of a very thin aluminum layer (5μm in thickness). The sample under examination placed on both sides of the positron source was prepared. Thickness of each sample should not be smaller than 2mm. A 1274 keV gamma ray is emitted (as initial signal) accompanied by positron birth, resulting in 1022 keV gamma rays when the emitted positron is annihilated by the electron in the sample (positron death or termination). This was performed using a fast-fast conventional study measuring the time interval of two gamma rays.

Two plastic scintillators (used for gamma detection, birth signal and death signal) are brought into contact with the photomultiplier tube (operates with 2050 base volts). The plastic scintillator is set to 1274 and 511 keV at two constant windows fraction differential discriminator separators (CFDD), which are used for timing signals. It is a multi-channel analysis system with a time converter (TAC) of incoming signals. Spectroscopic data obtained from MCA were used with the code LT-Polymer [14]. The resolution of the system is 350 ps and each run (at any temperature) is based on one million positron counts.

Kobayashi has determined the most important parameters in the positron technique, namely ortho-positronium atom lifetime and intensity spectroscopy. Since the ortho-positronium lifetime is long in the PALS system, it gives information about the free volume, free volume fraction and the size of the holes in the material structure.

2.1 The Simha-Somcynsky (SS) Theory and Hole Fraction (Theoretical part)

The SS theory describes the cell structure assuming that molecules and holes are for the same lattice in order to increase disorder in the polymer structure [15]. The occupied site fraction (y) is

$$y = 1-h = \frac{Ns}{N_h+Ns} \quad (5)$$

The partition function configuration expressing the occupied site and free volume fraction is given as [16,17]

$$Z_{conf} = g(N,y)\left[\upsilon_f(\tilde{V},y)\right]^{cN}\exp\left[-\frac{E_0(\tilde{V},\tilde{T},y)}{kT}\right] \quad (6)$$

By applying the lattice total energy, free volumes, and combinatorial factor values, the helmhotz free energy expression is obtained. Since the occupancy rate does not change in the equilibrium state of the system, its derivative is equal to zero according to the occupancy rate

$$\left(\frac{\partial F}{\partial y}\right)_{\tilde{V},\tilde{T},c/s} = 0 \quad (7)$$

$$\frac{s}{3c}\left[\frac{s-1}{s}+\frac{\ln(1-y)}{y}\right]-\frac{\eta-\frac{1}{3}}{1-\eta}-\frac{y}{6\tilde{T}}\left(y\tilde{V}\right)^{-2}\left[2.409-3.033\left(y\tilde{V}\right)^{-2}\right]=0$$

$$\eta = 2^{-1/6}y\left(y\tilde{V}\right)^{-1/3}$$

The equation of state of the polymer system is obtained from the derivative of the Helmholtz free energy with respect to volume at constant temperature in order to calculate the scaled values of P^*, V^* and T^*, as follows

$$P = -\left(\frac{\partial F}{\partial V}\right)_T = P\left[\tilde{V},\tilde{T}\right] = P\left[\tilde{V},\tilde{T};y\left(\tilde{V},\tilde{V}\right)\right]$$

$$\frac{\tilde{P}\tilde{V}}{\tilde{T}} = \frac{1}{1-\eta}+\frac{2y}{\tilde{T}}\left(y\tilde{V}\right)^{-2}\left[1.011\left(y\tilde{V}\right)^{-2}-1.2045\right] \quad (8)$$

The reduced PVT variables that establih the relation between Eq. (7) and Eq. (8) quantities as

$$\tilde{P} = \frac{P}{P^*}, \qquad \tilde{V} = \frac{V}{V^*}, \qquad \tilde{T} = \frac{T}{T^*} \quad (9)$$

The characteristic parameters, P^*, V^* and T^*, shown in Eq. (9) are

$$P^* = \frac{cT^*R}{mV^*}, \qquad V^* = \frac{\upsilon^* s}{m}, \qquad T^* = \frac{q_z\varepsilon^*}{c} \quad (10)$$

For the detailed information on SS theory, see Saygin Nuri et.al. [18].

The minimum and maximum deviation in specific volume are given by

 ISSN 1813-2065 (print) 2309-1673 (online) PRINTED IN IRAQ

$$\Delta V_{average} = \frac{100}{N}\frac{\left|V_{ith} - V_{iexp}\right|}{V_{iexp}} \qquad (11)$$

$$\Delta V_{\max} = \max(\Delta V_i)$$

3. Results and Discussion

The longest-lived atom in the PALS system is the ortho-positronium o-Ps component. Ortho-positronium lifetime (τ_3) and ortho-positronium intensity (I_3) are very sensitive to the volume and size of the defects in the material structure, which makes this system successful. In Table (2), the para-positonium p-Ps lifetime (τ_2) and intensity (I_2), the ortho-positonium lifetime and intensity, the radius of the free volume and the free volume fraction as the system parameters, are given as functions of temperature for different weights of TiO_2 (0, 10, 25 and 50mg).

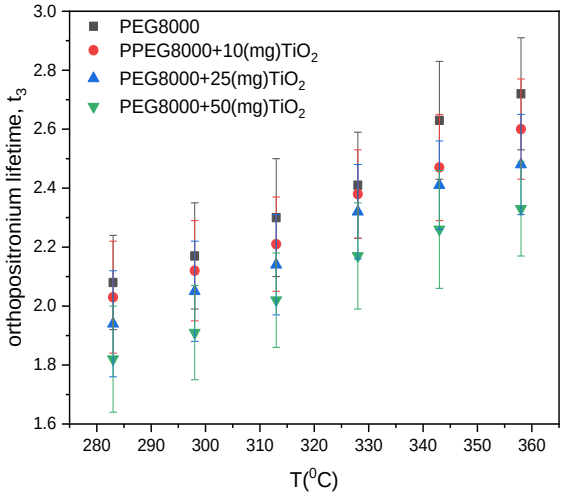

Fig. (1) The o-Ps lifetime versus temperature

Figure (1) shows the orthopositronium lifetime as a function of temperature for pure PEG8000 and PEG8000/TiO_2 composite samples with different weights of TiO_2 (10, 25 and 40mg) as additive. The linear increase in ortho-positronium lifetime is due to the increase in free volume as a function of temperature. There is a jump in ortho-positronium lifetime around 340K in pure PEG8000. Also, it is observed that there is a significant increase in the ortho-positronium lifetime between 325-330K in composites prepared with different weights of TiO_2 (10, 25 and 50mg) as addetive.

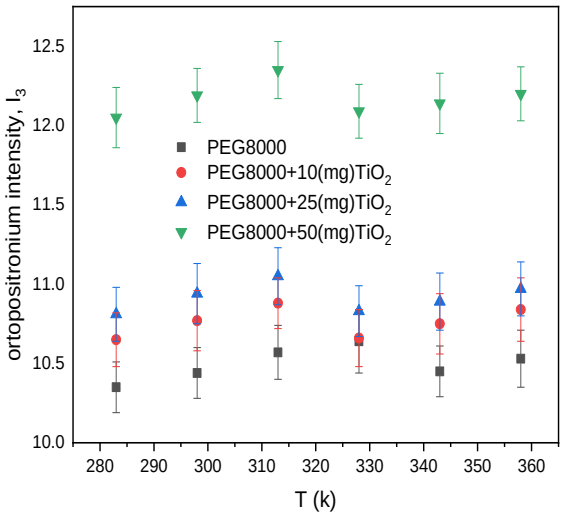

Fig. (2) The o-Ps inensity versus temperature

Figure (2) shows the orthopositronium intensity as a function of temperature for pure PEG8000 and PEG8000/TiO_2 composite samples with different weights of TiO_2 (10, 25 and 40mg) as addetive.

The Ortho-positronium intensity for pure PEG8000 increases as the temperature is increased up to 328K and above, then suddenly decreases at 340K. This indicates that the phase is changed in pure PEG8000 to glass transition state, then the orthopositronium intensity increases slightly. On the other hand, PEG8000/TiO_2 composite samples prepared with different weights of TiO_2 (10, 25 and 50mg) show a significant decrease in ortho-positronium intensity in the temperature range of 325-330K. As the amount of TiO_2 is increased, the ortho-positronium intensity increased due to the decrease in the free volume size.

For pure PEG8000, the ortho-positronium lifetime suddenly jumps and the ortho-positronium intensity suddenly decreases. This indicates that pure PEG8000 material has passed or entered to glassy transition temperature around 340K.

The aggregation between TiO_2 particles caused an increase in the free volume at the interface and created incompatibility between the these particles and the polymer chain in the structure of the composite. These increase and incompatibility caused electronic polarization, then the decrease in the dielectric constant leads to a decrease by few K in the glass transition temperature (T_g) of the composites with increasing the amount of TiO_2. The glass transition temperature (T_g) obtained for pure polymer as well as for composites, shows high degree of compatibility between the results of PALS and differential scanning calorimetry (DSC) analysis.

As shown in Fig. (3), o-Ps lifetime spectroscopy is plotted versus the weight of TiO_2 (0, 10, 25 and 50mg) in the PEG8000/TiO_2 composites at certain temperatures (10, 40, 70 and 85°C). As the weight of TiO_2 is increased, the o-Ps lifetime interval decreases due to a decrease in the free volume, especially for

the weight of 50mg TiO_2, as there is a significant decrease in the o-Ps lifetime.

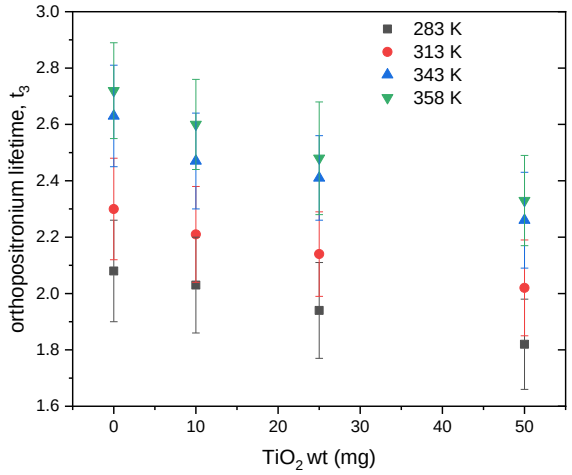

Fig. (3) The o-Ps lifetime versus temperature for different weights of TiO_2 (0, 10, 25 and 50mg) in the composite samples

In Fig. (4), o-Ps intensity spectroscopy is plotted versus the weight of TiO_2 (0, 10, 25 and 50mg) in the PEG8000/TiO_2 composites at certain temperatures (10, 40, 70 and 85°C). As the weight of TiO_2 is increased, the o-Ps lifetime interval decreases due to a decrease in the free volume, especially for the weight of 50mg TiO_2, as there is a significant decrease in the o-Ps lifetime.

Figures (5) and (6) show the variation of free volume fraction and free volume fraction, respectively, with neat PEG8000 and TiO_2 (10, 25 and 50mg). It has been determined that increasing TiO_2 ratio leads to the decrease free volume fracion slightly. It was determined by PALS spectroscopy that the intercellular free volume increases as the temperature is increased. When the weight of TiO_2 is increased, there was a decrease in free volume compared to pure PEG8000.

Equation (4) determines the free volume fraction, which has linear relation with the intensity of o-Ps and the hole free volume fraction, C' is the constant of PEG8000. Figure (7) shows that the experimental data of PALS are in agreement with theoretical data of SS. Using PALS technique, the o-Ps intensity and free volume were calculated at temperatures of 10, 25, 40, 55, 70 and 85°C, then the free volume fractions were calculated at the same temperatures by using theoretical SS theory. Experimental data and theoretical free volume fractions data were equalized in Eq. (4) and the values of the constant $C=(5.2\pm0.2)\times10^{-3}$ $Å^{-3}$ were found. Then, the free volume fractions for pure PEG8000 and PEG8000/TiO_2 composites were calculated with the C constant value.

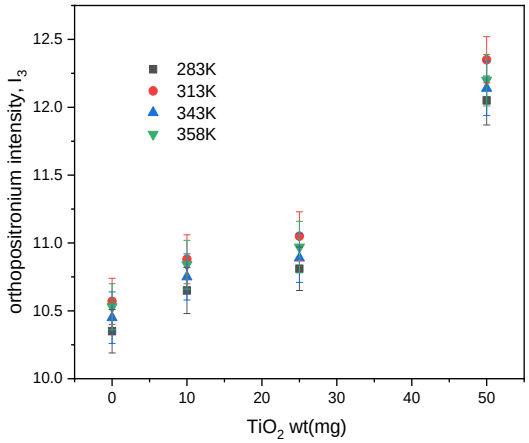

Fig. (4) The o-Ps intensity versus temperature for different weights of TiO_2 (0, 10, 25 and 50mg) in the composite samples

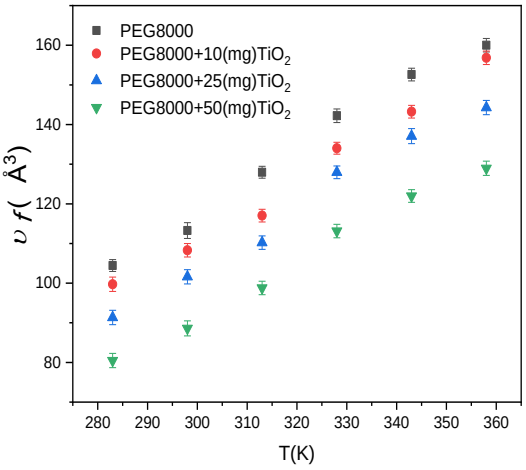

Fig. (5) The free volume versus temperature for different weights of TiO_2 (0, 10, 25 and 50mg) in the composite samples

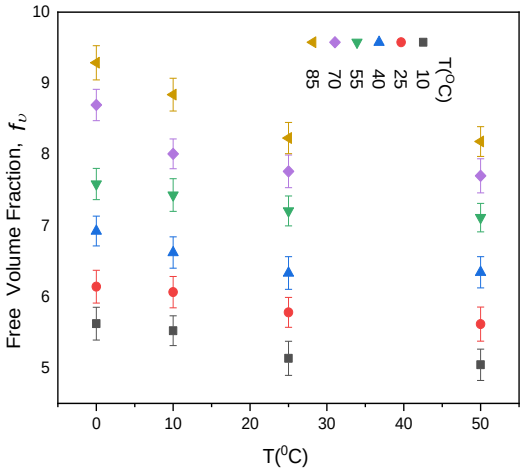

Fig. (6) The free volume fraction versus temperature for different weights of TiO_2 (0, 10, 25 and 50mg) in the composite samples

 ISSN 1813-2065 (print) 2309-1673 (online)

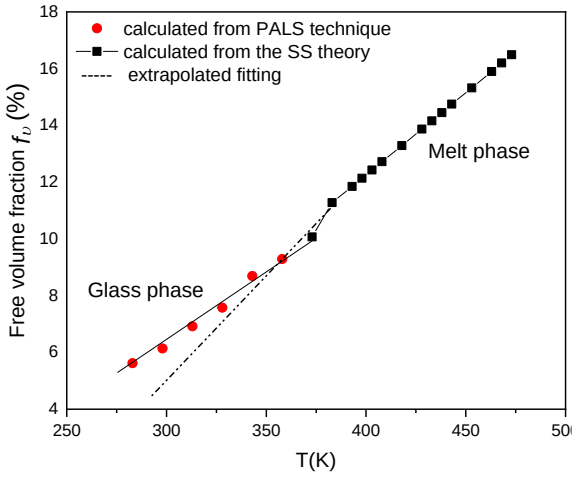

Fig. (7) The free volume fraction of PEG8000 versus temperature. The black dots are calculated from SS theory and red dots are calculated from PALS technique data (Eq. 4)

4. Conclusions

The PALS technique was used to examine the free volume size in prepared samples, pure polyethylene glycol and polyethylene glycol/titanium dioxde composites. The physical properties of both types of prepared samples were compared. With weight percentage of 5% of TiO_2 in the composite, a 20% reduction in free volume and more than 1% reduction in free volume fraction were observed. It can be concluded that the reduction in free volume and free volume fraction increases the durability and toughness of the polymer material.

References

[1] S. Gross et al., "PMMA: a key macromolecular component for dielectric low-k hybrid inorganic–organic polymer films", *Euro. Poly. J.* 43 (2007) 673-696.
[2] A. Covertino et al., "Poly(methyl methacrylate) nanocomposites based on TiO_2 nanocrystals: tailoring material properties towards sensing", *Thin Solid Films*, 519 (2011) 3931-3938.
[3] T. Asai, W. Sakamoto and T. Yogo, "*in situ* synthesis of transparent TiO_2 nanoparticle/polymer hybrid", *J. Mater. Sci.*, 48 (2013) 7503-7509.
[4] A. Antonello et al., "Nanocomposites of titania and hybrid matrix with high refractive index", *J. Nanopart. Res.*, 13 (2011) 1697-1708.
[5] A. Chatterjee, "Properties improvement of PMMA using nano TiO_2", *J. Appl. Polym. Sci*., 118 (2010) 2890-2897.
[6] D. Morselli, M. Messori and F. Bondioli, "Poly(methylmethacrylate)-TiO_2 nanocomposite obtained by non-hydrolytic sol–gel synthesis", *J. Mater. Sci.*, 46 (2011) 6609-6617.
[7] N.N. Hafizah et al., "Thermal degradation of nanocomposited PMMA/TiO_2 nanocomposites", *Mater. Sci. Eng*., 46 (2013) 012045.
[8] Y. Yang et al., "Preparation, characterization, and infrared emissivity property of optically active polyurethane/ TiO_2/SiO_2 multilayered microspheres", *J. Solid Stat. Chem.*, 184 (2011) 2617-2622.
[9] L. Zhou et al., "A novel electrospun PVDF/PMMA gel polymer electrolyte with in situ TiO_2 for Li-ion batteries", *Solid State Ionics*, 249 (2013) 93-97.
[10] I. Bodurov, T. Yovcheva and S. Sainov, "PMMA films refractive index modulation via TiO_2 nanoparticle inclusions and corona poling", Colloid Polym. Sci., 292(11) (2014) 3045-3048.
[11] D. Bamford et al., "The local free volume, glass transition, and ionic conductivity in a polymer electrolyte: A positron lifetime study", *J. Chem. Phys.*, 115(15) (2001) 7260-????.
[12] M.H. Cohen and D. Turnbull, *J. Chem. Phys.*, 31(5) (1959) 1164.
[13] Y.C. Jean et al., **"Principles and Applications of Positron & Positronium Chemistry**", Word Scientific (Singapore, 2003) 1-12.
[14] C.S. Chua et al., "Effect of annealing temperature on microstructure and UV light photocatalytic activity of TiO_2 films grown by atmospheric pressure CVD", *Chem. Vapor Depos.*, 20 (2014) 44-50.
[15] R.K. Jain and R. Simha, "On the Statistical Thermodynamics of Multicomponent Fluids – Equation of State", *Macromol.*, 13(6) (1980) 1501-1508.
[16] C.I. Poser and I.C. Sanchez, "Colloid interface", *Sci. J. Chem. Phys*., 69 (1989) 1307-1312.
[17] L.H. Sperling, **"Handbook of Introduction to Physical Polymer Science"**, 4th ed., John-Wiley & Sons, Inc. (NJ, 2006) 512-523.
[18] S.M. Nuri, "Extracting the Density Gradient Profile of Polyethylene Glycol from Bulk to Surface", *Kirkuk Univ. J. Sci. Stud.*, 12(4) (2017) 338-351.

Table (1) shows the characteristic parameters of PEG8000 that obtained by using SS theory

Polymer	*s*	*c*	P^* (MPa)	V^* (cc/g)	T^* (K)	$v^* 10^6$ (cc/g)	ε^* (K)	Min. Error	Max. Error
PEG8000	222	98	1064.23	0.86423	9030.7	31.148	398.35	0.0523	0.174

Table (2) PALS parameters as lifetimes and intensities in terms of temperature. τ_1 is taken as 125 ps as fixed in all calculation. The intensities are normalized as $I_1 + I_2 + I_3 = 1$

	T (°C)	τ_2 (ns) (±0.003)	I_2 (%) (±0.75)	τ_3 (ns) (±0.02)	I_3 (%) (±0.25)	R (Å) (±0.015)	f_v (%) (±015)
PEG8000	10	0.372	79.56	2.08	10.35	2.921	5.62
	25	0.379	78.82	2.17	10.44	3.000	6.14
	40	0.381	80.02	2.30	10.57	3.109	6.92
	55	0.359	79.41	2.41	10.64	3.198	7.58
	70	0.387	78.93	2.63	10.45	3.368	8.69
	85	0.384	79.74	2..72	10.53	3.434	9.29
PEG8000+10 (mg) TiO_2	10	0.381	78.44	2.03	10.65	2.876	5.22
	25	0.380	77.97	2.12	10.77	2.957	6.06
	40	0.377	77.21	2.21	10.88	3.034	6.62
	55	0.389	76.85	2.38	10.66	3.174	7.43
	70	0.383	77.71	2.47	10.75	3.246	8.01
	85	0.385	78.95	2.60	10.84	3.334	8.84

	T (°C)	τ_2 (ns) (±0.003)	I_2 (%) (±0.75)	τ_3 (ns) (±0.02)	I_3 (%) (±0.25)	R (Å) (±0.015)	f_v (%) (±015)
PEG8000+25 (mg) TiO_2	10	0.386	79.65	1.94	10.81	2.793	5.13
	25	0.395	78.03	2.05	10.94	2.895	5.78
	40	0.380	78.34	2.14	11.05	2.974	6.33
	55	0.373	77.90	2.32	10.83	3.126	7.21
	70	0.389	76.59	2.41	10.89	3.198	7.76
	85	0.402	77.91	2.48	10.97	3.253	8.23
PEG8000+50 (mg) TiO_2	10	0.397	77.44	1.82	12.05	2.678	5.04
	25	0.412	76.97	1.91	12.19	2.765	5.62
	40	0.421	77.21	2.02	12.35	2.867	6.34
	55	0.369	76.85	2.17	12.09	3.000	7.11
	70	0.384	76.71	2.26	12.14	3.076	7.67
	85	0.394	77.95	2.33	12.20	3.134	8.18

 ISSN 1813-2065 (print) 2309-1673 (online)

IRAQI JOURNAL OF APPLIED PHYSICS
Volume 19, Issue 2, April-June 2023, 33-37

Proceedings of the 3rd International Scientific Conference and 5th Scientific Conference, organized by College of Science, University of Tikrit, Tikrit, Iraq (28-29 December 2022)

Evaluation of Laser Influence on Optical Properties of Magnesium Oxide Thin Films Prepared by Drop Casting Method

Sahar N. Rashid[1]
Maha M. Ibrahim[1]
Faleh L. Mater[1]
Arshad M. Hamad[2]

[1]*Department of Physics, College of Science, University of Tikrit, Tikrit, IRAQ*
[2]*Department of Biology, College of Science, University of Tikrit, Tikrit, IRAQ*

In this work, the effect of laser irradiation on the optical properties of magnesium oxide thin films was investigated and evaluated. Thin films of magnesium oxide were prepared at a concentration of 0.2 M by depositing them on glass slides by drop casting method at temperature of 30-40 °C, then irradiating these films with a 5mW diode laser radiation (650nm) at different irradiation times (2, 4, 6 and 8 min). The distance between the sample to be irradiated and the laser source was 10 cm. Then, the UV-visible spectrophotometry was utilized to investigate the optical properties of the prepared thin films before and after laser irradiation.

Keywords: Drop casting; Laser irradiation; Magnesium oxide; Optical conductivity
Received: 13 October 2022; **Revised:** 29 October 2022; **Accepted:** 30 October 2022

1. Introduction

The irradiation of materials process is one of the important industrial applications of laser, as there are many studies which research in this regard and are still in continuous development [1-4]. Most of the laser energy is absorbed by the material irradiated by this laser, leaving little or no thermal damage to the surrounding area. The mechanism of laser interaction with matter is explained by the absorption of laser radiation by materials, which leads to the conversion of electromagnetic energy into electronic excitation, and this in turn turns into thermal, chemical and mechanical energies [5-8]. To reach a clear view of many physical and chemical properties of materials, one of the easiest ways is to study them in the form of thin films, as this technique has added a lot of facilities in the study of semiconductors [9-12]. The first physical properties that are studied for materials when interacted with a laser are optical properties [6], When the laser interacts with the material, the optical processes observed in the material can be categorized as reflection, refraction, absorption and transmission [5,6]. The optical properties of materials are determined using a number of parameters such as refractive index, absorption, and extinction coefficients [13-15]. Among the other optical parameters, the optical conductivity is one of the important parameters, which depends on the coefficients of both refraction and absorption, and is used to study the electronic states of the material [12]. To study and evaluate these parameters, UV-visible spectrophotometry is used and the general equation of UV-visible absorbance (A) as a function of wavelength (λ) can be given as:

$$A = G\lambda^{-s} \quad (1)$$

where G is a material-dependent constant and s is an exponent that varies between 0 and 4 [16]

Magnesium ions are of great importance in various fields in our lives, as they have many advantages such as non-toxicity, an abundance of its constituents, and chemical and physical stability. These properties recommend them for a wide range of applications in which it's antibacterial, antimicrobial, and photo-catalytic properties, and can be used for photovoltaic devices and gas sensor applications [17-20]. In biological field, they are an important factor in both the growth and maintenance of living cells and plays a central role in cellular function and to strongly influence the cardiovascular and neuromuscular excitability [21]. Magnesium oxide (MgO) is an inorganic material. It consists of hybridizing the s-orbitals of the magnesium (Mg) atom with the p-orbitals of the oxygen (O) atom. It has good chemical and thermal stabilities. MgO thin films are useful that has been widely used for industrial applications such as medicine biomaterials, refractory materials, heating apparatus, and infrared optics [18,19]. In this work, the effect of laser radiation on the optical properties of magnesium oxide was studied after being deposited as thin films by drop casting method.

2. Experimental Part

A solution contains of magnesium oxide at a concentration (0.2 M) was prepared by dissolving (0.952 gm) of magnesium chloride in (50 mL) of distilled water on a magnetic stirrer hotplate at a temperature (60-70 °C) for an hour. The deposition

process was carried out by drop casting method, which is summarized by adding drops of the prepared solution on the glass slide (which is placed on the hotplate at a temperature (30-40 °C)) and leaving it for about (5 min) for the liquid to evaporate, then adding drops again and repeating the process several times until a layer of the required substance is formed in a precipitate on the glass slide thus obtaining a thin film as in Fig. (1). Then the resulting thin films were irradiated with a 650nm diode laser with power of 5 mW and time periods of 2, 4, 6 and 8 min, noting that the distance between the sample to be irradiated and the laser was 10 cm. Double-beam UV-visible spectrophotometer device was utilized to investigate the optical properties of the thin films before and after laser irradiation.

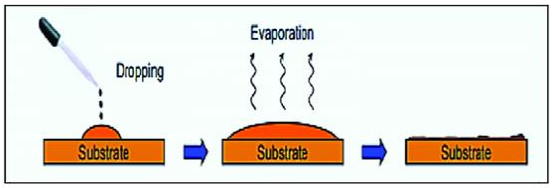

Fig. (1) Drop casting method

3. Results and Discussion

When the mixture of magnesium chloride and water is heated, the formed water crystals are lost by a series of reactions, so MgO is the final product of the drying process, and the formation of the gaseous product is reflected on the thermal scales as a loss of mass as stated in [22,23]. It is evident in Fig. (2) that the absorbance spectra of all the prepared samples peak in the region of short wavelengths, specifically at the λ (~350 nm), then begin to gradually decrease in the region of the visible spectrum and finally increase slightly in the near infrared region, where the electron transfer energy decreases as the wavelength increases. It is clear from the figure that it led to a decrease in their intensity, as exposure to laser raises the temperature of this material, and this result is consistent with previous literature, such as [18] which shows that the increase in the temperature of such samples leads to a decrease in the absorbance value. As for the peaks formed in the absorbance spectrum, they correspond to the energy gap (E_g) values of the prepared samples. That is, this increase in the temperature of the samples as a result of the increase in the exposure time to the laser led to an increase in the transmittance (T) of the material, and this is what we see in Fig. (3), which represents the transmittance spectra of MgO.

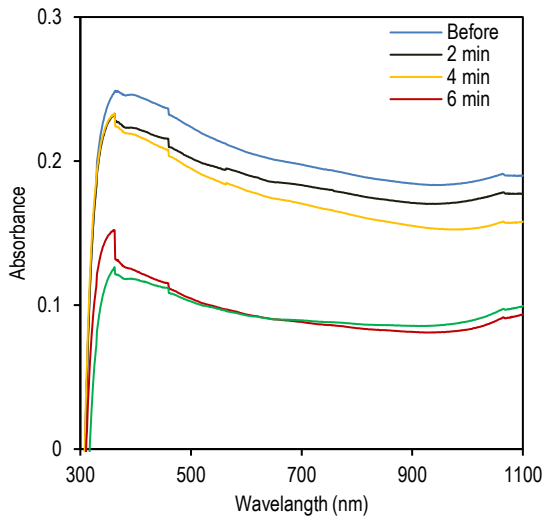

Fig. (2) Absorption spectra of the samples prepared before irradiation and after different irradiation times

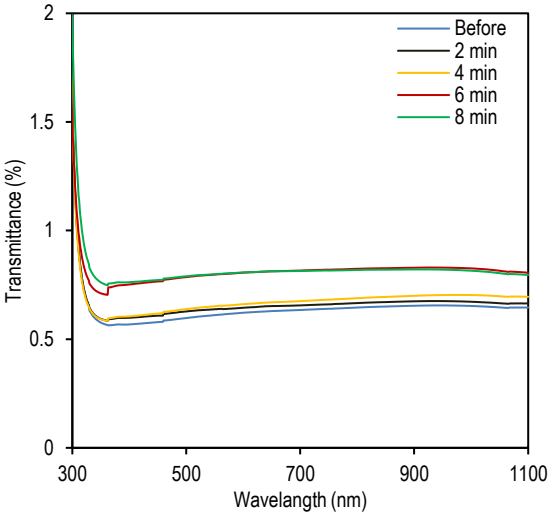

Fig. (3) Transmission spectra of the samples prepared before irradiation and after different irradiation times

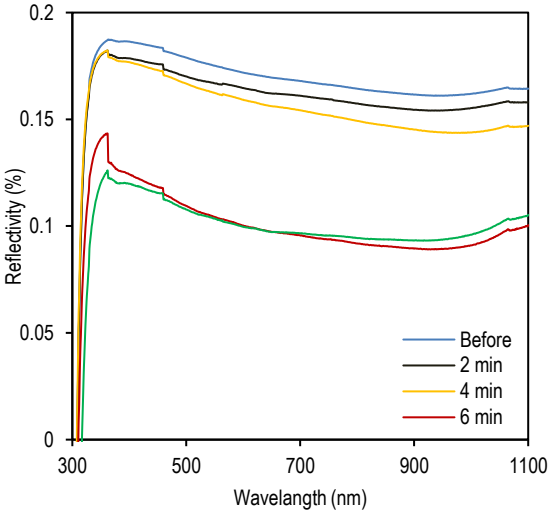

Fig. (4) Reflection spectra of the samples prepared before irradiation and after different irradiation times

The transmittance spectrum exhibits a behavior opposite to that of the absorbance spectrum. Figure (4) shows that the reflectivity (R) is high at short

 ISSN 1813-2065 (print) 2309-1673 (online)

wavelengths, then its values decrease at long wavelengths (low photonic energies). This behavior is similar to that of the absorbance (A), as the absorption is very little at energies less than E_g, and then increases with increasing energy [24]. The decrease in T is caused by an increase in the reflection from the surface of the thin film, and the increase in the laser irradiation time led to a decrease in the R in contrast to what happened to the transmission spectra.

Figures (5), (6) and (7) represent the absorption coefficient (α), extinction coefficient (K), and refractive index (n), respectively. The value of the absorption coefficient increases with the increasing photon energy, so we notice from the figure that its values decrease with increasing wavelength, i.e., with decreasing photon energy. Also, we note that it has direct electronic transitions because it has values higher than 10^4 cm^{-1}.

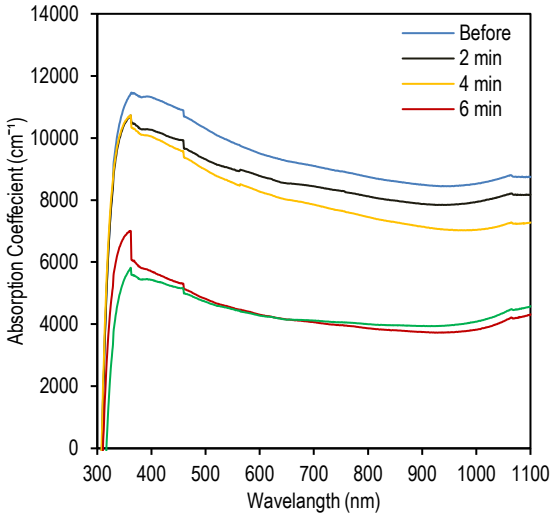

Fig. (5) Variation of absorption coefficient of the prepared samples with wavelength before irradiation and after different irradiation times

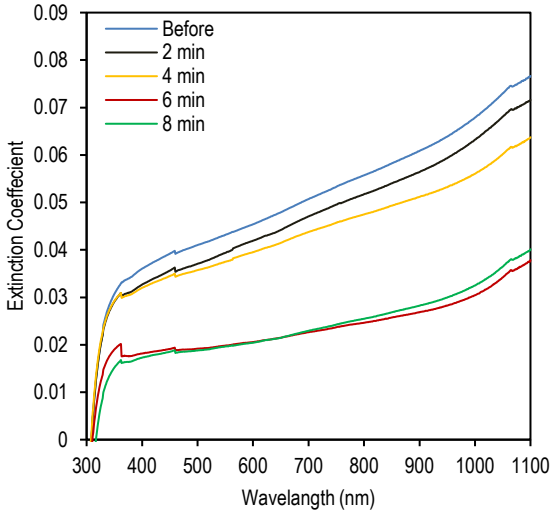

Fig. (6) Variation of extinction coefficient of the prepared samples with wavelength before irradiation and after different irradiation times

The curves of absorption coefficient are similar to those of absorbance as their values depend on the absorbance (A) as in Eq. (2), where α represents a measure of the absorption of laser beam passing through the prepared thin films of thickness t [11]:

$$\alpha = 2.303\frac{A}{t} \quad (2)$$

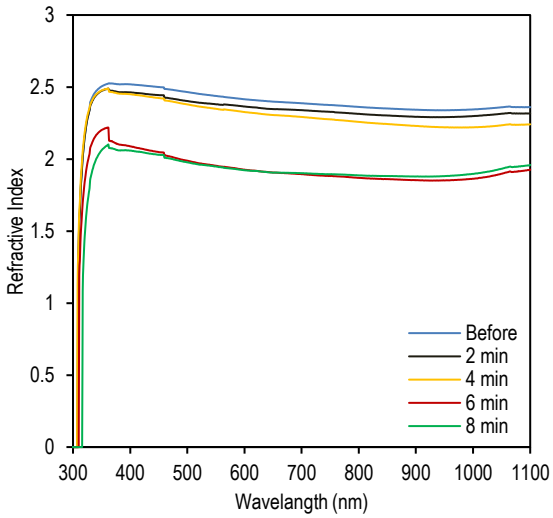

Fig. (7) Variation of refractive index of the prepared samples with wavelength before irradiation and after different irradiation times

The extinction coefficient was calculated depending on the wavelength and absorption coefficient as in Eq. (3), where K represents a property that determines the extent of the absorption or reflection strength of the MgO thin films for the laser. We note that its values increase at long wavelengths (low photon energies) as a result of the decrease in A of the material in this region. Its intensity decreases with increasing laser irradiation time. Extinction coefficient also represents the attenuation in the electromagnetic wave. It is decreasing with increasing photon energy. The laser irradiation led to a decrease in the intensity of these curves as a result of the increase in energy and thus decrease in the values of extinction coefficient [10,6]

$$K = \frac{\lambda\alpha}{4\pi} \quad (3)$$

$$n = \frac{1}{T} + (\frac{1}{T^2} - 1)^{\frac{1}{2}} \quad (4)$$

Equation (4) is used to calculate the refractive index in terms of T, where n is a measure of the curvature of the laser beam when it passes from the environment to the MgO thin films, and it is clear that its value decreases when the laser irradiation time increases. The variation of refractive index with wavelength is similar to that of reflectivity with wavelength, so, it is a function of the spectral reflectivity. Therefore, the results of the spectral reflectivity and its variation were reflected in the results of the refractive index.

The optical conductivity (σ) is used to study the electronic states of the material. It depends on α, n, and velocity of light (c) as [12]:

$$\sigma = \frac{\alpha n c}{4\pi} \quad (5)$$

Figure (8) illustrates the variation of σ with λ for the prepared thin films before and after laser irradiation. It can be seen that σ increases with increasing photon energy, where its values decrease at long wavelengths. Also, it is observed that σ is showing the same behavior of α and n. It was found to change sharply at wavelengths longer than 350 nm due to the sharp change in α, and decreases with increasing laser irradiation time. Figure (9) represents the relation between $(\alpha h\upsilon)^2$ and photon energy $(h\upsilon)$, where h represents Planck's constant and υ is the photon frequency. From this figure, we find that the values of energy band gap (E_g) range between 1.6 and 1.82 eV and increasing the irradiation time led to increase E_g, that can be calculated as [12]:

$$\alpha h\upsilon = B(h\upsilon - E_g)^{\frac{1}{2}} \quad (6)$$

where B is a constant depending on the type of material

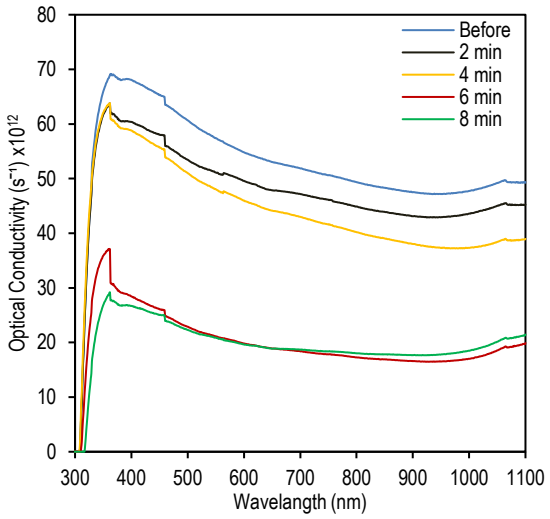

Fig. (8) Variation of optical conductivity of the prepared samples with wavelength before irradiation and after different irradiation times

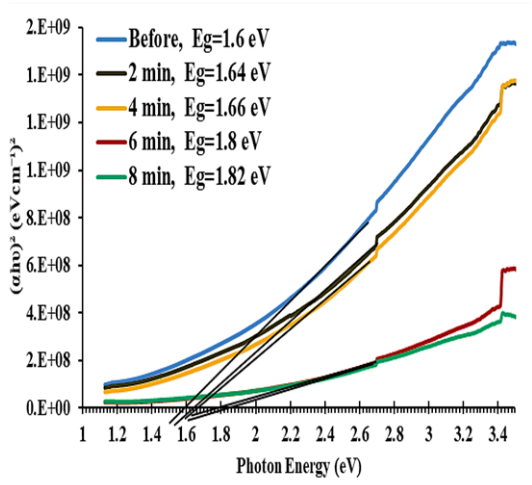

Fig. (9) Determination of energy band gap for the prepared samples before irradiation and after different irradiation times

The energy band gap (E_g) has an effect on the optical conductivity (σ) as the increase in E_g leads to a decrease in σ. The last equation is used to calculate the direct energy gap and the results of absorption coefficient showed that the material has direct electronic transitions.

According to previous literature, we find that it is possible to control the optical properties of MgO thin films by changing the thickness of the sample, concentrations, temperature, doping, etc., while in this work, we have been able to add a method to control the optical properties of MgO thin films by laser irradiation as well as its parameters. Such control may reduce both efforts and times required for the preparation of MgO thin films with specific properties.

4. Conclusion

In concluding remarks, laser irradiation of MgO thin films at long times led to a decrease in the values of absorbance, reflectivity, absorption coefficient, extinction coefficient, refractive index, as well as optical conductivity of these films, while the transmittance was increased with laser irradiation time. The energy band gap of the irradiated samples was determined to be ranging in 1.6-1.82 eV as it was increased with laser irradiation time. This work can be further developed by using other types of lasers as well as changing laser parameters to evaluate their effects on the properties of irradiated materials.

References

[1] M.E. Povarnitsyn et al., "Laser Irradiation of Thin Films: Effect of Energy Transformation", *Laser Particle Beams*, 31(4) (2013) 663-671.

[2] A.S. Jassim, S.N. Rashid and H.M. Yaseen, "Effect of CO_2 Laser Irradiation on the Topographic and Optical Properties of CdO Thin Films", *Baghdad Sci. J.*, 17(1) (2020) 318-328.

[3] M. Hasan et al., "Laser Irradiation Effects at Different Wavelengths on Phenology and Yield Components of Pretreated Maize Seed", *Appl. Sci.*, 10(3) (2020) 1189.

[4] S.M. Fayyad et al., "Studying the effect of compressing pressure and laser surface treatment on the properties of AlNiMgO", *Al-Kufa Univ. J. Biol.*, 10(1) (2018) 51-62.

[5] M.K. Rahman et al., "Laser Irradiation Effects on Gold", *Laser Phys.*, 17(12) (2007) 1382-1388.

[6] F.A. Tawil, "Study of Linear and Nonlinear Optical Properties of Fluorescein Sodium Dye", MSc thesis, University of Kerbala, Iraq (2017).

[7] A.V. Kimel, **"Laser-Matter Interaction"**, Radboud University (Netherlands, 2020).

[8] S. Krishnan and M. Mudrich, "Intense Laser Matter Interaction in Atoms, Finite Systems and Condensed Media: Recent Experiments and Theoretical Advances", *Euro. Phys. J.: Special*

 ISSN 1813-2065 (print) 2309-1673 (online)

Topics, 230 (2022) 3981-3988.

[9] O.A. Hammadi, "Using Third-Harmonic Radiation of Nd:YAG Laser to Fabricate High-Quality Microchannels for Biomedical Applications", *Optik Int. J. Light Electron Opt.*, 208 (2020) 164147.

[10] S.N. Rashid and S.M. Fayyadh, "Effect of Beta Ray on the Optical Properties of CuO Thin Films", *Diyala J. Pure Sci.*, 14(4) (2018) 40-52.

[11] K.I. Mohammed, A.S. Jasim and S.N. Rashid, "Effect of Annealing by CO_2 Laser on Structural and Optical Properties of CuO Thin Films Prepared by Sol-Gel Method", *Int. J. Phys.*, 4(3) (2016) 59-63.

[12] M.S. El-Bana and S.S. Fouad, "Opto-Electrical Characterisation of $As_{33}Se_{67}$–xSn_x Thin Films", *J. Alloys Comp.*, 695 (2017) 1532-1538.

[13] A.S. Jasim, K.I. Mohammed and S.N. Rashid, "Effect of Annealing by CO_2 Laser on Structural and Optical Properties of Zinc Oxide Thin Films Prepared by Sol-Gel Method", *Tikrit J. Pure Sci.*, 21(4) (2016) 112-121.

[14] A.S. Jasim, S.N. Rashid and A.J. Asaad, "Study the Interaction of CO_2 Laser with ZnO Thin Films and Its Effect on Its Topographic and Optical Properties", *Proc. 1st Int. 3rd Sci. Conf., College of Science, University of Tikrit*, P4 (2018) 139-146.

[15] O.A. Hamadi, "Characteristics of CdO-Si Heterostructure Produced by Plasma-Induced Bonding Technique", *Proc. IMechE, Part L, J. Mater.: Design & Appl.*, 222 (2008) 65-71.

[16] J. Alin, M. Rubino and R. Auras, "Effect of the Solvent on the Size of Clay Nanoparticles in Solution as Determined Using an Ultraviolet–Visible (UV-Vis) Spectroscopy Methodology", *Appl. Spectro.*, 69(6) (2015) 671-678.

[17] M. Tlili et al., "Synthesis and Characterization of MgO Thin Films Obtained by Spray Technique for Optoelectronic Applications", *Nanomater.*, 11 (2021) 3076.

[18] R. Aouati et al., "Structural and Optical Properties of MgO Thin Films Prepared by Dip-Coating Process: Effect of Thickness", *Semicond.*, 55(7) (2021) 583-590.

[19] J.P. Singh et al., "Approaches to Synthesize MgO Nanostructures for Diverse Applications", *Heliyon*, 6(9) (2020) e04882.

[20] A.O. Mousa, N.A. Nema and S.H. Trier, "Study of Structural and Optical Properties for MgO Films Prepared by Using Chemical Spray Pyrolysis Technique", *Mater. Sci.: An Indian J.*, 14(11) (2016) 426-434.

[21] J. Durlach et al., "Magnesium Chloride or Magnesium Sulfate: A Genuine Question", *Magnes. Res.*, 18(3) (2005) 187-192.

[22] N.J.M. Grobler, C.J. Postma and P.L. Crouse, "Reaction Kinetics of ZrF_4 Chloridation at Elevated Temperatures", *J. South. African Inst. Mining Metall.*, 117(10) (2017) 927-930.

[23] F.J. Kadhim, O.A. Hammadi and N.H. Mutesher, "Photocatalytic activity of TiO_2/SiO_2 nanocomposites synthesized by reactive magnetron sputtering technique", *J. Nanophot.*, 16(2) (2022) 026005.

[24] O.A. Hammadi, "Effects of Extraction Parameters on Particle Size of Titanium Dioxide Nanopowders Prepared by Physical Vapor Deposition Technique", *Plasmonics*, 15(6) (2020) 1747-1754.

IRAQI JOURNAL OF APPLIED PHYSICS
Volume 19, Issue 2, April-June 2023, 38-42

Proceedings of the 3rd International Scientific Conference and 5th Scientific Conference, organized by
College of Science, University of Tikrit, Tikrit, Iraq (28-29 December 2022)

Physical Properties of Biogas Produced by Anaerobic Treatment of Household Waste in Samarra City for Thermal Energy Production

Shareef F.S. Al-tikrity
Qutaiba M. H. Ali

Department of Physics,
College of Science,
Tikrit University,
Tikrit, IRAQ

In this study, an anaerobic digestion (AD) system was used to generate biogas from organic waste collected in Samarra city throughout the anaerobic digestion process. The fermentation process was performed in the form of four batches and a retention period of 25 days. The highest cumulative biogas production quantity was obtained at 60.001L for a 1:2 mixing ratio in summer and the lowest production quantity was 32.152L for a 1:4 mixing ratio in winter. This result may be attributed to the increase in production, which is related to the rise in temperature. The average temperature inside the digester was 32-43°C in winter and 45-56°C in summer. The change in the pH value and its active role in the process of decomposition of organic waste was also observed when the pH value was ranging within 7.2-7.7.

Keywords: Anaerobic digestion; Renewable energy; Biomass; Biogas production
Received: 12 October 2022; **Revised:** 14 November 2022; **Accepted:** 21 November 2022

1. introduction

Organic waste dumped at landfills is an important factor to the diffusion of toxic gases as a result of the decomposition processes that occur in it [1]. The international strategy followed in most developing countries for solid waste disposal has been landfilling. Therefore, there was a need to provide alternative waste treatment strategies such as gas capture from landfills as well as anaerobic fermentation processes for organic waste to obtain biogas [2]. We urgently need to provide clean renewable energy to maintain a healthy environment and thus provide optimal development for all sectors [3]. Biomass is an inexhaustible resource and is gaining great importance as the need for an alternative to fossil fuels increases [4]. Instead of considering food waste as a burden on municipalities, it can be used to produce biogas as well as be used as organic fertilizer [5]. Food residues from houses can be utilized by separating them from the source and benefiting from them using the processing represented by anaerobic digestion [6]. The method of burning is considered to have negative effects on the environment and is not considered a suitable option due to the high moisture content it possesses as well as the landfill method generates the emission of gases, which contributes to global warming, while anaerobic digestion is the most successful and convenient way to produce biogas and digest biomass and to take advantage of the remnants of the undigested part as organic fertilizer which is a series of chemical reactions that take place on biomass without the help of oxygen and with the help of bacteria where decomposition occurs. Organic matter is called hydrolysis and leads to the formation of biogas and the digestion of living masses [7]. The efficiency of anaerobic digestion is influenced by many factors such as temperature, pressure, humidity, pH value and retention time as well as the mixing ratios of biomasses and water. In addition, the density of organic matter and its impact on the amount of cumulative biogas production is affecting too [8]. It is necessary to carefully follow the environmental conditions to keep the parameters within the appropriate range with the activity and growth of bacteria responsible for the decomposition of biomasses and the achievement of anaerobic digestion.

2. Experiment

2.1 Materials and methods

Household waste was collected from selected areas of the city of Samarra for study. A mobile aanaerobic fermentation system was used with a capacity of one batch of 2000 liters. This system includes a mixing tank containing a cutting saw to mix organic waste with water before placing the waste in the system. The papers and plastic waste were sorted and other strange things were carefully selected and separated from the organic waste in the collected waste. They were then sorted and stirred well to divide the large blocks into small particles.

 ISSN 1813-2065 (print) 2309-1673 (online)

The quantity is placed in form of small parts in the cutting tank to be well mixed and stirred to ensure that large parts of organic waste are properly fragmented and that a homogeneous mix is achieved. The mixture is then poured into the digestion tank and properly closed from the shut-off valve to ensure a tight closure. The waste was loaded for the fermentation process over four time periods and in different mixing ratios determined by the following relationship:

$$\text{Mix Ratio} = \frac{\text{Biomass(kg)}}{\text{Water (kg)}} = \frac{70}{280} = \frac{1}{4} \qquad (1)$$

Therefore, the 1:4 ratio represents the first mixing ratio, as well as the rest of the mixing ratios as shown in table (1)

Table (1) The ratio of mixing organic waste with water

Biomass	Organic Waste Mass (kg)	Amount of Water (kg)	Mix Ratio
Winter period	70	280	1:4
Winter period	140	280	1:2
Summer period	70	280	1:4
Summer period	140	280	1:2

All mixing ratios underwent a retention period of 25 days each, with two mixing ratios during the winter and two mixing ratios during the summer. All fermentation operations carried out were subjected to ambient temperatures and none of samples were synthetically heated. The arrangements are fully prepared at the experimental site to avoid the shadow from the sun to ensure maximum solar radiation reception. Monitoring and measurement of the ambient temperature of the site as well as measurement of biogas production throughout the retention period were daily continuous. The experiments described in this study are part of a range of fermentation processes for biogas production that have been conducted and the total energy came entirely from solar radiation. The parameters analyzed were pH, temperature, humidity, and the amount of cumulative biogas produced.

3. Results and discussion

3.1 Effect of mixing ratios on amount of cumulative biogas

Figure (1) shows the cumulative biogas production (L) of various fermentation samples during the 25-day retention period during winter and summer. The amount of biogas production for the sample with mixing ratios of 1:2 and 1:4 during summer was 60.001 and 39.94 liters, respectively, while for the mixing ratio of 1:2 and 1:4 during winter, it was 45.17 and 32.152 liters, respectively, during retention time of 25 days. From this result, we can conclude that biogas generation in summer is the highest among all samples, where the highest amount of biogas production for the mixing ratios was 1:2 during summer and winter, knowing that the difference in the amount of cumulative biogas production is due to influence of the temperature and humidity in summer compared to winter. However, this ratio was better than the mixing ratios of 1:4 during winter and summer due to the mass amount of organic mass for the mixing ratio 1:2. This indicates that the amount of concentration of nutrients in the digester has a role in increasing the production of biogas. Figure (1) shows the effect of the cumulative biogas production rate with the mixing ratios of biomass with water. Biogas production was higher after 18 days of retention time and was almost minimal after 23 days of retention.

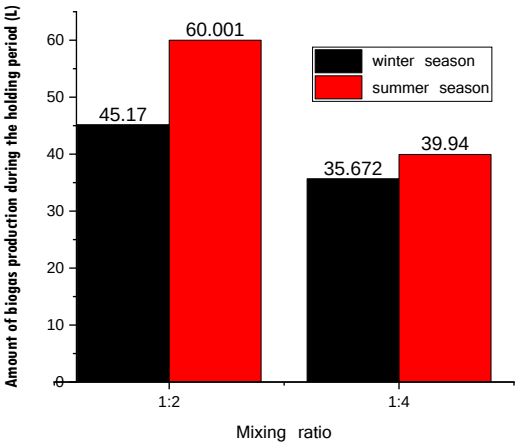

Fig. (1) Amount of cumulative biogas (L) during the retention period (days) in winter and summer for different mixing ratios

3.2 Effect of retention time on the amount of biogas generation

Biogas generation (ml/day) for fermentation processes with different mixing ratios is shown in figures (2) and (3). It can be concluded that the maximum biogas generation process observed in the fermentation process with a mixing ratio of 1:2 in summer. The fermentation process showed higher biogas production for the 1:4 mix ratio in summer, while the biogas generation was lower for the fermentation process for the 1:4 mix ratio and for the mix ratio 1:2 in winter during retention period of 13-19 days. From these figures, it can be concluded that the anaerobic digestion of water associated with food waste in biogas generation decreases slightly with decreasing temperature. As well, the highest daily production was fermentation with a 1:2 mixing ratio in summer and 3314 ml/day for the 17^{th} day, followed by a 1:4 mixing ratio fermentation for the 18^{th} day. Then the fermentation process with a mixing ratio of 1:2 and a mixing ratio of 1:4 for the 17^{th} day in winter, and the amount of gas produced for the highest daily amount was about 2685, 2675 and 1896 ml/day, respectively, during the four fermentation processes. The cumulative production of biogas differed according to the duration of stay, as shown in Fig. (1), and it can be concluded that the total generation of biogas in the summer was higher than the production of the two fermentation processes in the winter due to the difference in temperature and its effect on

increasing production when it rises. Cumulative biogas production was measured over the survival times of the four fermentation processes. For a mix ratio of 1:2 in winter, the amount of gas produced per 1 kg of food waste was about 322.44 ml/kg, while a previous study on household food waste found methane production to be 472 ml/kg [9]. In another study, methane from restaurant waste was measured at 440 ml/kg [10]. Compared to other studies, methane production in this study was lower for mix ratio of 1:4 due to the diversity in food waste across regions, while the methane production ratio was very close to these studies, especially when changing the mix ratios to a 1:2 ratio in winter.

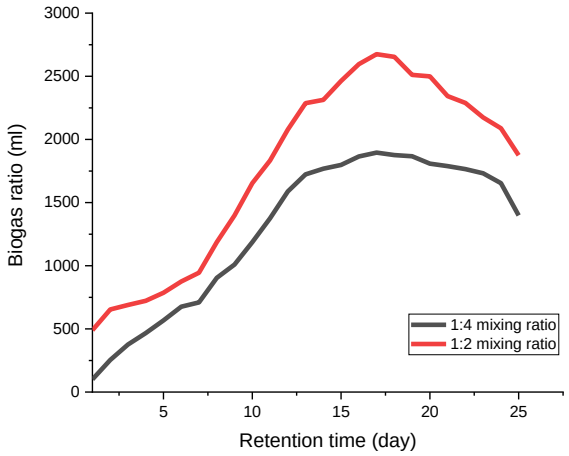

Fig. (2) Amount of biogas produced for each day of the retention time and two mixing ratios during winter (ml/day)

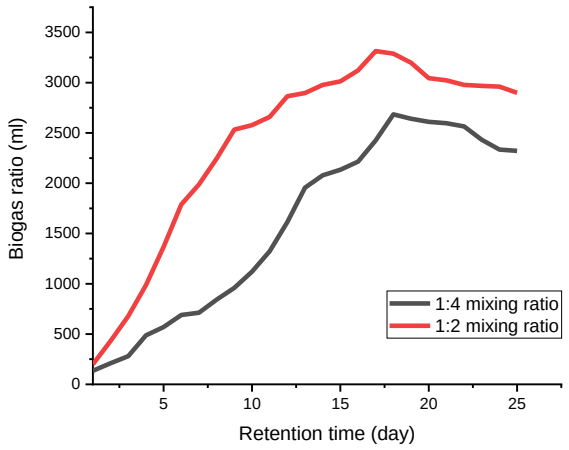

Fig. (3) Amount of biogas produced for each day of the retention time and two mixing ratios during summer (ml/day)

On the other hand, it was found that the cumulative yield of biogas for the ratio of 1:4 and 1:2 during summer was 570.57 and 428.57 ml/kg, respectively. The cumulative amount of biogas for a mix ratio of 1:4 during winter was 459.31 ml/kg during the retention period. This is considered a good amount of gas production compared to previous studies [9,10].

3.3 Effect of temperature change and pH value during storage time

The changes of temperature inside the AD tank were measured along with the time of retention of the four mixing ratios each day during the fermentation process. Figure (4) shows the daily change in temperature with the time of retention where the changes were uneven. For figures (4a,c), the temperature rates were higher because the fermentation process was in summer and the outside temperatures were high, which led to higher temperatures inside the fermentation tank and higher heat storage than in the fermentation process in winter where the temperatures were low as shown in figures (4b,d) for two fermentation processes in winter. The explanation is that the temperature inside the fermentation tank (AD) was higher than the temperature outside the digester due to the biological reaction that generates a higher temperature and also because the system is tightly closed and the fermentation tank maintains the temperature. There was a difference in temperature values, with the average temperature ranging from 22 to 43°C in winter indicating that anaerobic digestion was in the range of medium temperatures [3,4]. There is no external heat for anaerobic digestion to control the temperature but due to the climate of the city and during the retention period as temperature is one of the factors affecting the production of biogas as shown in Fig. (4), the temperature from inside the digester and from the outside was observed during the retention period for all four mixing ratios. There was an effect of external temperature on the amount of heat inside the digester, since there was an increase in the heat inside the digester because the walls of the digester are made of zinc-galvanized iron and coated with (GOOD HIM) coating that prevents heat loss. It comes into direct contact with the atmosphere as the walls of the fermentation tank for anaerobic digestion lose or absorb heat depending on the difference between the temperature inside and outside the digester and the effect of the external climate on the organic matter inside the digester. Also, there is a difference between the temperature for four mixing ratios between winter and summer in addition to a difference in the amount of biogas production. This is attributed to temperature differences where the reaction is slower during the retention time and production of biogas.

The variance in the the amount of pH is indicated by the retention time in Fig. (5) showing the relationship between the amount of pH and the retention time for four mixing ratios. As can be seen from the figure, there is a significant correlation between the retention time and pH value. It is clear that the pH recorded the lowest value at the beginning of the first day of the anaerobic digestion retention time for four mixing ratios (4.58, 3.75, 4.65, and 3.67) for the 1:2 mixing ratio in winter, 1:4 in winter, 1:2 in summer, and 1:4 in summer, respectively. The

 ISSN 1813-2065 (print) 2309-1673 (online)

reason for the low pH values is that stage of anaerobic digestion is the first stage that begins with the formation of acids and is called the stage of decomposition and disintegration. This is consistent with the explanation of the reference [16] who showed that in the first stage of the fermentation process of the organic masses, a rapid disintegration of the organic masses occurs where organic acids such as acetic acid are produced, which leads to a decrease in pH. When 1 g of NaOH per 10 liters of organic mass was added during the fermentation process, the pH value increases to make the medium suitable for bacteria growth and biogas production.

As the running time progressed and from the observation of Fig. (5) for the pH value during the retention period, it was noted that the pH value increased in the third day of the run time to be 6.22, 5.3, 6.42, and 5.14 for the 1:2 mixing ratio in winter, 1:4 in winter, 1:2 in summer, and 1:4 in summer, respectively, and these values were 7.3, 7.5, 7.5 and 7.46 for the mixing ratio 1:2 in winter, 1:4 in winter, 1:2 in summer and 1:4 in summer, respectively. Then, the high pH values were observed during the successive days of anaerobic fermentation to approach the quantitative 7.2-7.7. The values of pH were monitored during the retention days to control these values. It is also observed from Fig. (6) that the pH value is stable after this period due to the generation of methane by converting fatty acids, which leads to an increase in the pH value during anaerobic digestion.

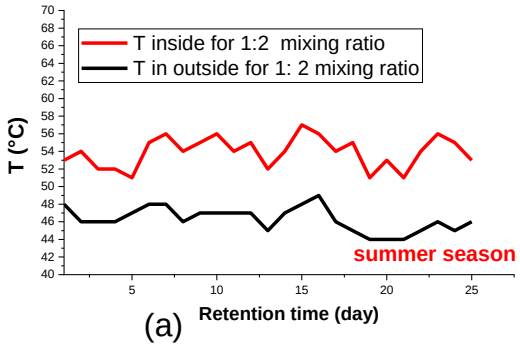

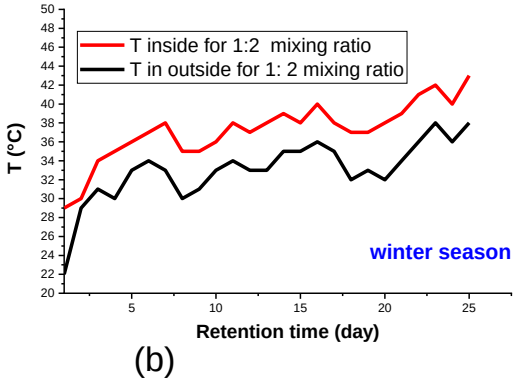

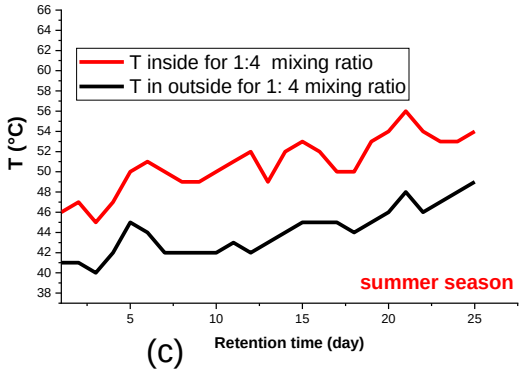

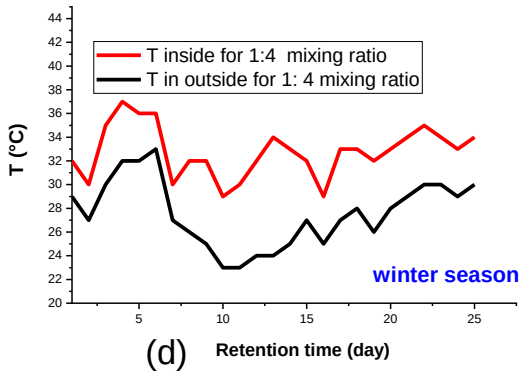

Fig. (4) Daily change in temperature with retention time for (a) 1:2 mixing ratio in summer, (b) 1:2 mixing ratio in winter, (c) 1:4 mixing ratio in summer, and (d) 1:4 mixing ratio in winter

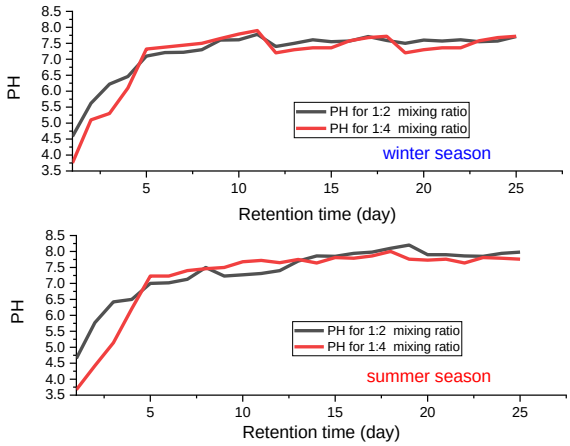

Fig. (5) Change in pH value during the retention time in winter and summer

3.4 Effect of moisture during AD process

The moisture degree as well as its differences within the anaerobic digester were observed and measured with the retention time for the four mixing ratios, as in Fig. (6). It was found that the average degree of moisture content within the system is not equal in the four mixing ratios (89.76%, 85.88%, 74.44%, and 73.9%). These values were agreeing with the optimum value of moisture inside the fermentation tank that ranging in 60-85%. As shown in Fig. (7), the degree of moisture in each fermentation process for different mixing ratio was measured. It was found that the highest degree of moisture of the anaerobic fermentation tank was

about 90% for the mixing ratio of 1:4 in summer and this is due to the effect of temperature, which has an effective role in increasing the humidity rate inside the fermentation tank as well as the mixing ratio, where moisture content is the highest at high temperature and lowest at low temperature. This could explain the differences in the results as the organic materials contain high substances of liquids and this increases the moisture content as shown in Fig. (6). Also, there was a discrepancy between the humidity levels due to the difference in fermentation times and the effect of the ambient temperature, which affects in turn the humidity rates inside the fermentation tank.

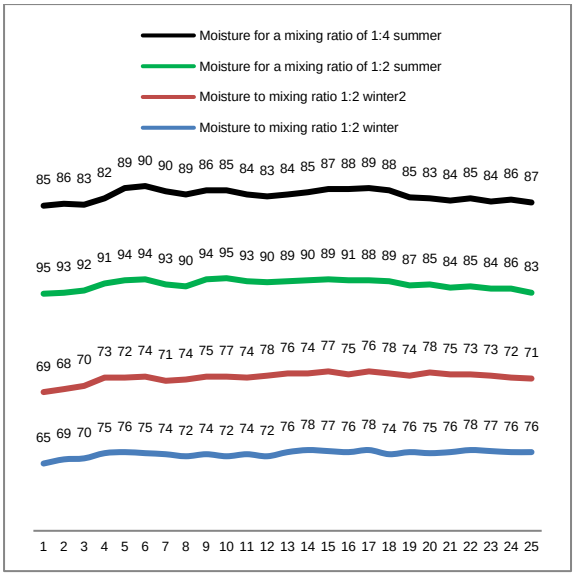

Fig. (6) Levels of moisture (%) inside the anaerobic digester for the different mixing ratios

4. Conclusion

The results obtained from this study showed the best mixing ratio for organic waste and water, where the rate of production increases with the increase of organic matter. As well, the physical factors that affect the rates of biogas production were introduced. The rise in temperature had an important role in increasing bacteria growth, which in turn helps to decompose organic waste and produce higher biogas. Also, controlling the pH value at a moderate acidity rate leads to an increase in the production of biogas. Furthermore, it was observed that the high humidity has an important role in increasing the production of biogas as it provides a favorable environment for the reproduction of bacteria to help produce methane gas. The household waste of Samarra city can be beneficial in producing biogas as an alternative to the fossil fuels and helping to preserve the environment from the effects of the accumulation of these wastes.

References

[1] B. Bharathiraja et al., "Biogas production – A review on composition, fuel properties, feedstock and principles of anaerobic digestion," *Renew. Sustain. Energy Rev.*, 90(4) (2018) 570-582.

[2] I.R. Abubakar et al., "Environmental Sustainability Impacts of Solid Waste Management Practices in the Global South," *Int. J. Environ. Res. Public Health*, 19(19) (2022) 12717.

[3] D. Liu et al., "Study on personalized microbial formulation during high-temperature aerobic fermentation of different types of food wastes," *Sci. Total Environ.*, 814 (2022) 152561.

[4] Z.A. Elum and A.S. Momodu, "Climate change mitigation and renewable energy for sustainable development in Nigeria: A discourse approach," *Renew. Sustain. Energy Rev.*, 76 (2017) 72-80.

[5] Y. Chen, J.J. Cheng and K.S. Creamer, "Inhibition of anaerobic digestion process: a review," *Bioresour. Technol.*, 99(10) (2008) 4044-4064.

[6] G. Zhang et al., "Design and analysis of a biogas production system utilizing residual energy for a hybrid CSP and biogas power plant," *Appl. Therm. Eng.*, 109 (2016) 423-431.

[7] K. Schanes, K. Dobernig and B. Gözet, "Food waste matters-A systematic review of household food waste practices and their policy implications," *J. Clean. Prod.*, 182 (2018) 978-991.

[8] A. Mudhoo and S. Kumar, "Effects of heavy metals as stress factors on anaerobic digestion processes and biogas production from biomass," *Int. J. Environ. Sci. Technol.*, 10(6) (2013) 1383-1398.

[9] J.K. Cho, S.C. Park and H.N. Chang, "Biochemical methane potential and solid-state anaerobic digestion of Korean food wastes," *Bioresour. Technol.*, 52(3) (1995) 245-253.

[10] R. Zhang et al., "Characterization of food waste as feedstock for anaerobic digestion," *Bioresour. Technol.*, 98(4) (2007) 929-935.

 ISSN 1813-2065 (print) 2309-1673 (online)

IRAQI JOURNAL OF APPLIED PHYSICS
Volume 19, Issue 2, April-June 2023, 43-47

Proceedings of the 3rd International Scientific Conference and 5th Scientific Conference, organized by
College of Science, University of Tikrit, Tikrit, Iraq (28-29 December 2022)

Photoresponse and Quasi-two-dimensional Electron Gas Transport of $Sm_2O_3/SrTiO_3$ Heterointerfaces Films Prepared by Sol-gel Method

Ali H. Mohammed[1]
Randa K. Hussain[2]
Sabri J. Mohammed[1]

[1] Department of Physics, College of Education for Pure Sciences, University of Tikrit, Tikrit, IRAQ
[2] Department of Physics, College of Science, Al-Mustansiriyah University, Baghdad, IRAQ

Applications of the forthcoming multifunctional oxide electronics heavily rely on the two-dimensional electron gas (2DEG) transport behaviors. This research prepared the Sm_2O_3/ STO heterointerfaces using the sol-gel process, the prepared films were coated on $SrTiO_3$ (STO) substrate by spin coating technique. The pulsed-laser deposition (PLD) process is used in this study to examine the 2DEG emergence at Sm_2O_3/STO heterointerfaces by annealing the sample at 650 and 700°C. On the basis of oxygen vacancies mechanism, the structural and photoresponcivity are studied. The photoresponsive qualities of $Sm_2O_3/SrTiO_3$ heterointerfaces and the impact of annealing temperatures on the crystallinity, morphology, and properties of Samarium oxide (Sm_2O_3) thin film were explored with the aid of XRD, FE-SEM, AFM, and analyses. The produced Sm_2O_3 thin film with thickness (72 nm) has better crystallinity (have crystallite size 230.6nm) and optical characteristics as a result of the higher deposition temperature 700°C. The different Oxygen (O_2) vacancies that are present at the surfaces of these materials are what give $Sm_2O_3/SrTiO_3$ heterointerfaces their photoresponsiveness.

Keywords: Samarium oxide; Pulsed-laser deposition; Electron gas; Photoresponsive
Received: 22 November 2022; **Revised:** 29 November 2022; **Accepted:** 05 December 2022

1. Introduction

To develop novel technologies that exceed the constraints of semiconductor technology for the developing field of oxide electronics and microelectronic, the transition metal oxide heterostructures have received a lot of attention [1,2]. At the interfaces of related oxides, an epitaxially growing two-dimensional gas with high mobility was produced by Ohtomo and Hwang in 2004 [3]. When two dielectric oxides come into contact, a two-dimensional electron gas (2DEG) forms, have lately received much interest due to these interfaces combine an extremely simple interface construction with a high carrier density. The heterointerfaces display a wide range of intriguing physical phenomena, involving superconductivity, coexistence of ferromagnetism [4,5]. States of the magnetic field [6,7], the phenomena of Kondo [8,9]. The photoinduced effect, on the other hand, provides a practical and dependable technique to lessen the insulator-metal transition's change in properties as an external disturbance of the heterointerfaces [10]. A common example of this phenomenon is produced at a $SrTiO_3$ single crystal substrate with a TiO_2 termination surface, a layer of $LaAlO_3$ (LAO) is formed on surface. Due to their all-titanate surfaces, and the Ti-O sub-continuity lattices across the interface, the heterojunction exhibits different behavior expressed into 2EDG. Samarium oxide (Sm_2O_3) thin film is one of the most promising candidate dielectrics due to its high dielectric constant (k=715), large energy band gap (4.33eV), high breakdown electric field (57MV/cm), low leakage current, constrained frequency dispersion, and good thermal stability [11,12]. The crystal structure of Sm_2O_3 is could transform form phase to another (phases A, B and C). The cubic C type is formed by thermal decomposition of hydroxide, oxalate or carbonate precursors [13]. The atomic positions and displacement parameters of the oxygen atoms plays key role in the Sm_2O_3 properties. Samarium oxide attributable of its potential application in nanomagnets, semiconductor glass, biochemical sensors, nanoelectronic devices, and solar cells, one of the rarest-earth oxide minerals is also one of the most expensive [14,15].

This study aims to demonstrate the effect of annealing on the structural properties of the $Sm_2O_3/SrTiO_3$ heterointerfaces prepared by spin coating method within a principle of 2EDG. The structural and morphological characteristics of the Sm_2O_3 films formed at various annealing temperatures (650 and 700°C) have been studied using x-ray diffraction (XRD), atomic force

microscopy (AFM) and field-emission scanning electron Microscope (FE-SEM). The photoresponse of Sm_2O_3/STO was also studied.

2. Experimental Part

Sol–gel spin-coating was used to deposit Sm_2O_3 thin films on to $SrTiO_3$ (100). Ethanol was used to clean the substrates, which have dimensions of 5x3x0.5 mm^3. The substrates were then placed in an ultrasonic device for 10 min. and during this time, the ethanol was replaced with deionized water. With ethanol alcohol and deionized water, the same procedure was done over the same period of time. In order to create the smooth TiO_2-terminated $SrTiO_3$, the $SrTiO_3$ substrates were first etched for 38 s in hydrofluoric acid (HF) with NH_4F buffer [17]. Samarium oxide of 1.7g was dissolved in 5ml of anhydrous N.N-Dimethlyformamide (DMF). Then 0.5g of polyvinylpyrrolidone (PVP) was added to the solution. With electron-rich oxygen atoms and electron-deficient nitrogen atoms, PVP's structure in the polar solvent N.N.-dimethylformamide (DMF) resonates with oxygen [18]. After roughly 24 hours of spinning the final solution with a magnetic stirrer at 1000 rpm, the Sm-precursor sol was produced. The metal ions are therefore evenly distributed in the PVP by polar contact or hydrogen bonding after 24 hours of stirring at 40°C. The chemical spin coating procedure was used twice, first for 60 s at a rotational speed of 9000 rpm, and the second for 20 s at 3000 rpm. To benefit from the homogeneous layers that can be produced by the rotational coating technique, the produced films were annealed twice, first at 460°C for 4 hours in air and the second at 750°C for 30 min in a high vacuum environment of $4.0x10^{-5}$ Pa. The temperature was elevated to 650-700°C for the second annealing step. Pulsed-laser deposition (PLD) consisting of 225nm KrF excimer laser, with target-substrate distance of 100 mm and laser power density of approximately 2.0 J/cm^2.pulse (pulse duration of 30 ns and repetition frequency of 5 Hz). While the Al wire was ultrasounded welded into contact with the electrodes, the resistance was measured as a function of time for 2 hours in dark. The procedure involved exposing the samples to light for 20 s, turning it off for 180 s, then repeating the procedure twice. Prior to exposure to radiation, samples were maintained at 300 K for 2 hours.

3. Results and Discussion

Figure (1) displays the XRD patterns of Sm_2O_3/$SrTiO_3$ films grown at various annealing temperatures (650 and 700 °C). It is observed how the patterns correlate to the (220), (440) and (356) preferred directions, with diffraction peaks at 22.89°, 46.47° and 72.72°, respectively, according to Bragg's law:

$$n\lambda = 2dsin\theta \quad (1)$$

where n is an integer, λ is the electron wavelength (Cu Kα X-ray radiation source λ=1.5406Å), d is the crystal lattice spacing between atomic planes and θ is the angle of incidence reflection

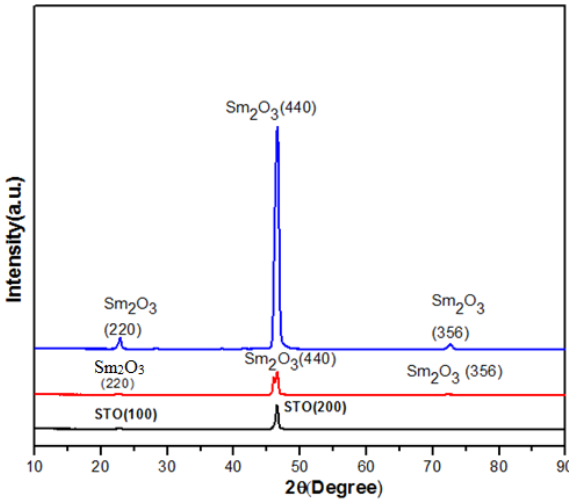

Fig. (1) XRD patterns of as-deposited Sm_2O_3 films on STO substrates (black line), annealed at 650°C (red line), and annealed at 700°C (blue line)

The crystal system shows a cubic shape of samarium made from Sm_2O_3/$SrTiO_3$, indicating that the crystallinity of Sm_2O_3 increased with the oxidation temperature. This may mean that the Sm_2O_3 thin film is well oriented normally to the substrate. It is also revealed that the (200) Bragg peak of STO becomes obviously wider when the sample annealed at 700°C because the peak of (440) plane of Sm_2O_3 is very close to the strong peak of $SrTiO_3$, implying that the Sm_2O_3 films are formed using the spin coating technique throughout annealing. The maximum of Sm_2O_3 XRD peak is nearly overlapped with peak of the $SrTiO_3$ substrate, which indicated that the Sm_2O_3 grown on $SrTiO_3$ substrate attends highly crystallinity and good out-of-plane texture with the c-axis perpendicular to the surface of the substrate. Thin film shows a single orientation without secondary phases, which was confirmed by absence of other peaks are appeared. Moreover, the diffraction intensity of Sm_2O_3 peaks becomes stronger with raising annealing temperature, and no impurity phase or other orientation was observed. Thus, the Sm_2O_3 films with crystalline phase were prepared in the temperature range from 650 to 700°C. The average crystallite size of Sm_2O_3 samples was estimated by Scherrer's formula with annealing temperature of 650 and 700 °C. The minimum value of crystallite size is 172.8 nm at 2θ=22.89° for annealing temperature of 650°C according to the (220) plane, while it increased to 247.1 nm at 2θ=22.89° for annealing temperature of 700°C in the same plane. According to Scherrer's formula, the crystallite size is inversely proportional to the full-width at half maximum (FWHM). Since the Scherrer's equation only gives a lower bound on the crystallite size and microstrain is not taken into account, the out-of-plane lattice parameter was calculated from XRD data. Relaxation processes occur during growth in a layer-by-layer mode on

 ISSN 1813-2065 (print) 2309-1673 (online)

lattice-mismatched, the strain relaxation process strongly depends on the lattice mismatch. It is clearly observed that the peak width in XRD is insensitive to the defect density, but critically depends on the residual lattice strain in Sm_2O_3/ $SrTiO_3$ films. The formation of stacking faults in the Sm_2O_3 film results in some local distortions of the (220) lattice planes and could be a possible mechanism for releasing the lattice mismatch between the Sm_2O_3 film and the $SrTiO_3$ substrate. The growth of strongly oriented cubic Sm_2O_3 on $SrTiO_3$ (100) may be understood by considering the lattice match between the two. The lattice constant of cubic Sm_2O_3 is 1.0927 nm, which matches closely with that of $SrTiO_3$, whose lattice constant is 0.3905 nm (lattice mismatch = 0.7%). The result showed that the diffraction peak of Sm_2O_3 films shifted to a small angle and the lattice mismatch of about −1.2%, which indicates a tensile strain in the Sm_2O_3 thin film. It is illustrated that the out-of-plane of Sm_2O_3 films are affected by tensile strain.

The AFM micrographs of cubic Sm_2O_3 films grown on $SrTiO_3$ at temperatures of 650-700°C, shown in figures (2a,b), demonstrate the $SrTiO_3$ substrate's uniform step, with a step width of 270nm and a step height of around 0.38nm, which corresponds to the $SrTiO_3$ substrate's lattice parameter in (100), which is attributed to the fact that the surface of the (100) $SrTiO_3$ terminated with TiO_2 was formed after chemical and thermal treatment [19]. The upper layer of Sm_2O_3 was smooth and has surface roughness and root-mean-square (RMS) of 993.892 and 1.821 nm, respectively.

The morphology of the films grown on the substrates, showing the faceted grains, indicates that the films are well crystallized, and the preferred orientation is displayed. The surface roughness was increased according to the fundamentals of grain filling and film texture following high-temperature annealing. This corresponds to the XRD method, where the peak corresponding to the reflection is (220) cubic Sm_2O_3.

In the FE-SEM images, the film thickness measurement at the Sm_2O_3/ $SrTiO_3$ heterointerfaces is displayed. With a magnification of 250kx times, the SEM investigation for the films formed on $SrTiO_3$ reveals that the film surface is extremely smooth (Fig. 3a). The Sm_2O_3/$SrTiO_3$ has constant grained morphology, crystallinity and structural characteristics. Figure (3b) exhibits the FE-SEM image taken for a 37.24nm-thick Sm_2O_3 film produced by PLD on a $SrTiO_3$ substrate at annealing temperature of 650°C. This image further demonstrates the film's crystallinity correlating with the results of AFM and XRD. The SEM image of the Sm_2O_3 film produced by PLD at 700 °C on a $SrTiO_3$ substrate terminated, shown in Fig. (3c), illustrates that the films exhibit a very fine-grained morphology when the growth temperature is increased.

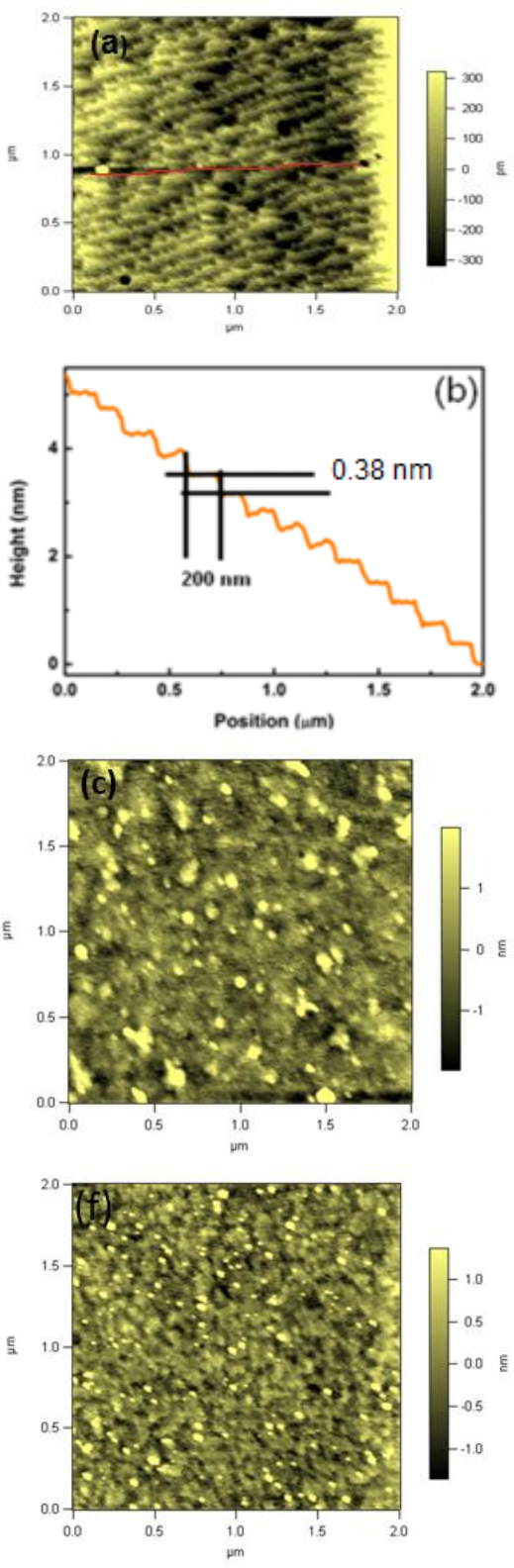

Fig. (2) (a) AFM micrograph of a TiO_2-terminated STO (100) after chemical and thermal treatment, (b) Scan profile of STO substrate taken at the yellow line in (a). (c) AFM micrograph for the Sm_2O_3/STO samples annealed at 650°C, and (f) AFM micrograph for the Sm_2O_3/STO samples annealed at 700°C

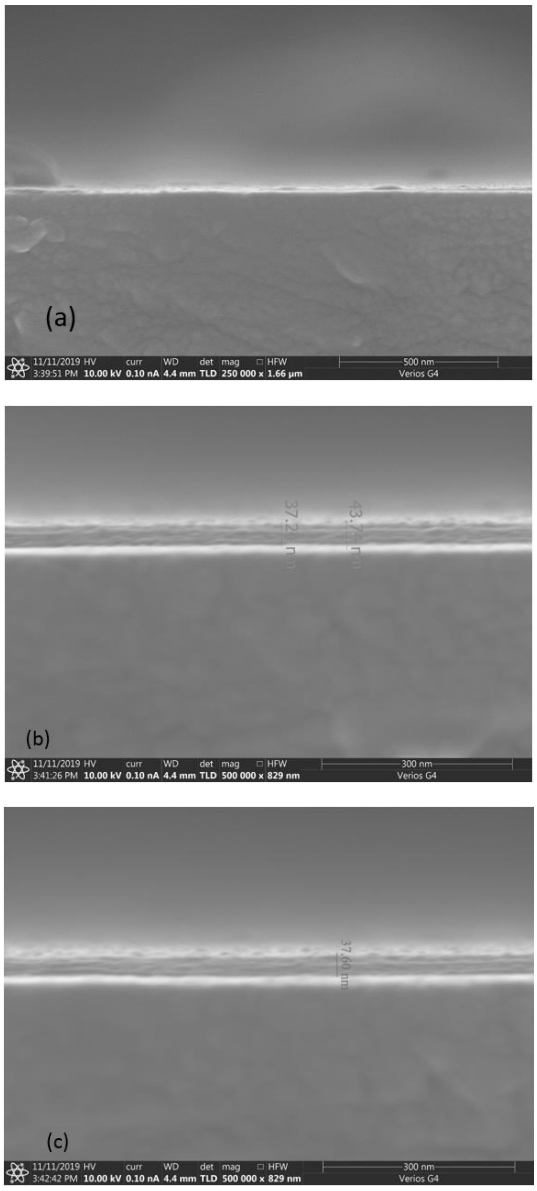

Fig. (3) FE-SEM images of (a) the films in STO, (b) 37.24nm-thick Sm_2O_3 on TiO_2-terminated STO grown by PLD at 650°C, and (c) 37.60nm-thick Sm_2O_3 on TiO_2-terminated STO by PLD at 700°C

Time-dependent photocurrent of the synthesized device was used to assess how annealing temperature influences as the stability of the photodetector was measured under a 360 nm laser irradiation with a 1.89 mW/mm^2 power density for 20s performed at different temperatures, ON and OFF, repeatedly. These experiments focused on the resistance of $Sm_2O_3/SrTiO_3$ heterointerfaces, according to Fig. (4). When the laser irradiates the surface, the photoexcited electrons and holes are produced in the $SrTiO_3$ substrate, additional electrons are induced at the two-dimensional electron interface. On the other side, electron traps are formed by the remaining oxygen vacancies. The $SrTiO_3$ band gap has these traps [20-22]. More electrons are carried by photon production at the two-dimensional electron interface excited as a result of the positively charged layer at the interface, there are electrons and holes in the $SrTiO_3$ substrate of a TiO_2-substrate of terminated $SrTiO_3$ and the region of negative electronic space charge that produces the two-dimensional electron interface. By tunneling at the surface, the nanoparticles absorb holes, which causes the photoconductivity to grow. The macroscopic potential barrier spatially separates the photoexcited electron from the parent donor defects after a free electron is created by the absorption of a photon. As a result, irradiation-induced resistance of heterointerface diminishes at different temperatures and is not reversible. The current drops quickly to the initial value when the light is switched OFF. The response and decay times are both reduced as the annealing temperature is increased, which also enhances the film quality and lowers flaws in the film.

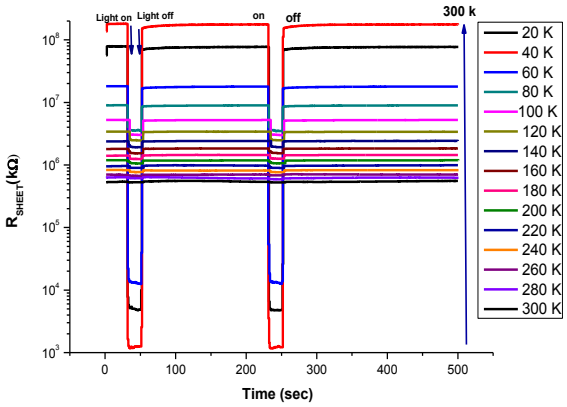

Fig. (4) Time evolution of the resistance at Sm_2O_3/STO interface

4. Conclusions

In conclusion, it was shown that Sm_2O_3 may grow on $SrTiO_3$ utilizing PLD, producing high-quality 2DEG materials via spin coating. Here, the ON/OFF ratio and responsiveness are improved due to the interface effect of $SrTiO_3$ substrates. Utilizing photoelectric devices made of all oxides is made possible by the tunable photoresponsive characteristics at $Sm_2O_3/SrTiO_3$ interfaces. Studying the fleeting photoresponsive behavior could help to elucidate the important mechanism. Additionally, the polarity of spin has a desirable nature, particularly in 2DEG systems, which is advantageous to the spintronics of all oxide devices. The electrons in a 2DEG currently have disordered spin directions. In the interim, it is anticipated that novel magnetic-optical-electric response devices will use the photoresponse in combination with ferromagnetism in a two 2DEG. Finally, more works will be required to realize the actual application of 2DEG system-based oxide optoelectronics.

References

[1] P. Zubko et al., "Interface physics in complex oxide heterostructures", *Annu. Rev. Cond. Matt. Phys.*, 2 (2011) 141-165.

 ISSN 1813-2065 (print) 2309-1673 (online)

[2] C. Cen et al., "Oxide Nanoelectronics on Demand", *Science*, 323 (2009) 1026-1030.
[3] A. Ohtomo and H.Y. Hwang, "A high-mobility electron gas at the $LaAlO_3/SrTiO_3$ heterointerface", *Nature*, 427 (2004) 6973.
[4] N. Reyren et al., "Superconducting interfaces between insulating oxides", *Science*, 317 (2007) 1196-1199.
[5] K. Ueno et al., "Electric-field-induced superconductivity in an insulator", *Nat. Mater.*, 7 (2008) 855-858.
[6] P. Moetakef et al., "Carrier-controlled ferromagnetism in $SrTiO_3$", *Phys. Rev. X*, 2 (2012) 021014.
[7] K. Michaeli, A.C. Potter and P.A. Lee, "Superconducting and ferromagnetic phases in $SrTiO_3/LaAlO_3$ oxide interface structures: possibility of finite momentum pairing", *Phys. Rev. Lett.*, 108 (2012) 117003.
[8] L. Li et al., "Coexistence of magnetic order and two-dimensional superconductivity at $LaAlO_3/SrTiO_3$ interfaces", *Nat. Phys.*, 7 (2011) 762-766.
[9] X. Wang et al., "Magnetoresistance of two-dimensional and three-dimensional electron gas in $LaAlO_3/SrTiO_3$ heterostructures: influence of magnetic ordering, interface scattering, and dimensionality", *Phys. Rev. B*, 84 (2011) 075312.
[10] H.X. Liang et al., "Giant photovoltaic effects driven by residual polar field within unit-cell-scale $LaAlO_3$ films on $SrTiO_3$", *Sci. Rep.*, 3 (2013) 1975.
[11] T. Atou et al., "Reversible B-type–A-type transition of Sm_2O_3 under high pressure", *Mater. Res. Bull.*, 24 (1989) 1171.
[12] G. Brauer and R. Müller, Anorg, "Beiträge zur Polymorphie der Sesquioxide der Seltenen Erden", *J. Inorg. Gen. Chem.*, 321(5-6) (1963) 234-245.
[13] A.A. Zav'yalova et al., "Crystal Structure of Sm_2O_3", *Sov. Phys. Crystallogr.*, 21 (1976) 727-729.
[14] A. Bartos et al., "Refinement of atomic positions in bixbyite oxides using perturbed angular correlation spectroscopy", *Acta Crystallogr. B*, 49(2) (1993) 165-169.
[15] M. Mitric et al., "Magnetic properties of trivalent Sm ions in $Sm_xY_{2-x}O_3$", *J. Alloys Compd.*, 485(1-2) (2009) 473-477.
[16] T.-M. Pan et al., "Effects of CF4 Plasma Treatment on the Electrical Characteristics of Poly-Silicon TFTs Using a Tb_2O_3 Gate Dielectric", *IEEE Trans. Electron Dev.*, 57(7) (2010) 1519-1526.
[17] L. Eyring, in **"Handbook on the Physics and Chemistry of Rare Earths"**, vol. 3 (Eds.: K.A. Gschneidner Jr., L. Eyring), North-Holland Publishing Co. (Amsterdam, 1979), Ch. 27, p. 337.
[18] T. Liu et al., "Synthesis and characteristics of Sm_2O_3 and Nd_2O_3 nanoparticles", *Langmuir*, 19(18) (2003) 7569-7572.
[19] V.A Rozhkov, A.Yu Trusova and I.G Berezhnoy, "Silicon MIS structures using samarium oxide films", *Thin Solid Films*, 325(1-2) (1998) 151-155.
[20] H. Yan et al., "Modulated Transport Behavior of Two-Dimensional Electron Gas at Ni-Doped $LaAlO_3/SrTiO_3$ Heterointerfaces", *ACS Appl. Mater. Interfaces*, 9(44) (2017) 39011-39017.
[21] W. Siemons et al., "Origin of Charge Density at $LaAlO_3$ on $SrTiO_3$ Heterointerfaces: Possibility of Intrinsic Doping", *Phys. Rev. Lett.*, 98(19) (2007) 196802.
[22] J. Carrasco et al., "First-principles calculations of the atomic and electronic structure of F centers in the bulk and on the (001) surface of $SrTiO_3$", *Phys. Rev. B*, 73(6) (2006) 064106.

IRAQI JOURNAL OF APPLIED PHYSICS
Volume 19, Issue 2, April-June 2023, 48-52

Proceedings of the 3rd International Scientific Conference and 5th Scientific Conference, organized by College of Science, University of Tikrit, Tikrit, Iraq (28-29 December 2022)

Optical Quality of Copper Oxide Nanoparticles Prepared by Plasma Jet Electrolysis Technique

Saif Aldeen M. Hanfoosh[1]
Khalid H. Razeg[1]
Kadhim A. Aadim[2]

[1] *Department of Physics, College of Education for Pure Sciences, University of Tikrit, Tikrit, IRAQ*
[2] *Department of Physics, College of Science, University of Baghdad, Baghdad, IRAQ*

In this paper, we synthesized copper nanoparticles using atmospheric pressure plasma jet in electrolysis system at different times 3, 5, 7 and 9 minutes. The electrode (cathode) was made of atmospheric pressure plasma, while the (anode) was made of copper tape. This review summarizes the progress made in copper oxide nanoparticle-based devices. X-ray diffraction (XRD), scanning electron microscopy (FESEM), and UV-visible spectroscopy were used to confirm the characterization of the core-core CuO nanoparticles. XRD analysis confirmed that there are other peaks associated with the secondary CuO phases, and it may be due to the increase in time and the effect of high voltage (16 kV). For the most part. The UV-visible spectra of the copper oxide nanoparticles show a blue shift. The shape of the copper oxide nanocrystals revealed by this method is affected by the electrolysis media and preparation time. The appearance of copper oxides increases with time gradually, indicating an increase in solution concentration. The copper oxide particles are homogeneous and have different particle sizes around 18, 37, 42 and 59 nm, respectively. These results support the preparation of these nanostructures for use in gas sensing applications.

Keywords: Copper oxide; Plasma jet; Reaction time; Nanoparticles
Received: 23 November 2022; **Revised:** 3 December 2022; **Accepted:** 10 December 2022

1. Introduction

Metal oxide nanostructures have intrigued scientists because of their size and shape-dependent properties, which can be created in a variety of ways. Due to their high surface-to-volume ratio, they are great candidates for a variety of sensing applications such as gas sensors, optical sensors, humidity sensors, and biosensors [1]. Plasma electrodes (atmospheric plasma jetting electrolysis technology) are used as cathodes to fabricate copper oxide nanoparticles and the anode is a strip of copper in a gas-liquid medium. Plasma is used to perform liquid transitions, and the electrolytic media system is illustrated as a vacuum device. The plasma electrode connects the electrolytic system with both electrons and ions, and many interactions can be seen during electrolysis as the color of the liquid changes over time, which also uses electrodes from different metals as electrodes in the ionic electrolyte [2]. First, explain the method of copper oxide nanocrystals generated using CuO metal for time [3,5,7,9] min, which has not been seen before. Nanoparticles have recently attracted attention due to their uses and properties. Copper oxide is an important material with uses in solar energy conversion [3,7], sensors, as well as catalysts [4,5,6,8,9]. Plasma jet technology has many benefits and advantages, such as environmental compatibility, low cost, and no need for expensive equipment [10]. Potential applications include visible-light-induced photodegradation of organic pollutants [11]. Second, the optical properties of these nanoparticles generated by the plasma jets were also investigated, with the initial phase including the generation of CuONPs, and the crystal structure and phase purity of the copper nanoparticles generated by the atmospheric pressure plasma jets were confirmed by x-ray diffraction (XRD) and obtained with orthorhombic structures. FESEM images showed that the resulting particles were collected into nanoparticles and showed spherical shapes and other stems densely covered with copper oxide nanocrystals. Moreover, copper oxide is inexpensive, low-toxic, and environmentally acceptable [12–14], and they are excellent choices for a wide range of sensing applications, including future gas sensors.

2. Preparation Method

An atmospheric plasma jet was used to produce copper oxide nanoparticles. appearance. Figure (1a) shows a schematic diagram of the experimental procedure as well as the discharge image in Fig. (b). The method consists of a stainless steel tube serving as a cathode (inner circumference 2.5 mm, length 5 cm). It was three centimeters from the anode. The

copper compound was prepared using a copper tape (1 cm wide, 6 cm long) as an anode that was immersed in a liquid and sprayed with jet plasma at different times (3, 5, 7 and 9 minutes), we obtained copper oxide particles and the length between the liquid's surface and the ends of the needle was 1 cm . Argon was utilised as the drain gas, and it was connected to the syringe through a glass flowmeter at a rate of 3 ml/min. The response took place in a calculated (10) ml glass beaker, and the beaker was filled with distilled water to (7) ml. (2.5 cm wide and 3.5 cm long). The copper electrode was polished before being rinsed with distilled water. The copper ribbon was then submerged in the electrolysis system using pure water. The discharge was ignited using a DC power source and a strong voltage of 16 kV at 50 kHz. The electrolyte system was exposed to different times (3, 5, 7 and 9 min), and the electrolyte changed color as shown in Fig. (2a). It was dried for 1 hour at 51 °C as shown in Fig. (2b).

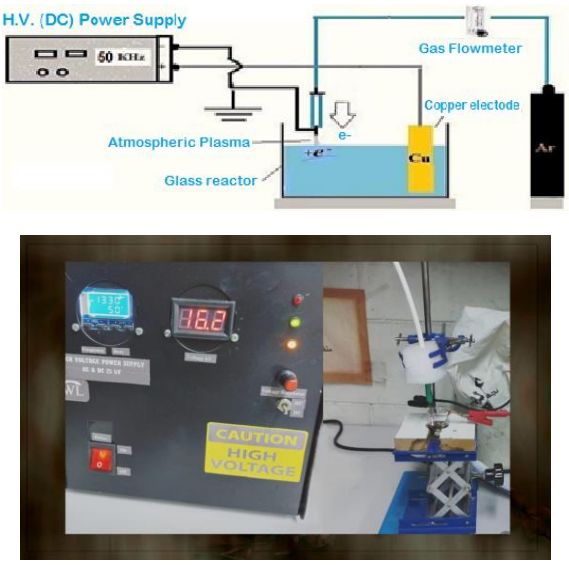

Fig. (1a) Schematic diagram of the experimental design, (b) electrolysis discharge images of air plasma jets to produce copper oxide nanocomposites

3. Results and discussion

An X-ray diffraction (XRD) assay validated the crystal structure and phase purity of CuO nanoparticles produced using the atmospheric pressure plasma jetting (APJs) method and determined by comparing the diffraction angles of CuO with the ICDS tag number in the literature. And the study will only be for common peaks. The XRD pattern of CuO nanoparticles was captured in the 2θ angle range from 10 to 80, as shown in Fig. (3). The XRD pattern of CuO nanoparticles showed diffraction peaks at 32.901° and 38.295°, which correspond to the structure of CuO and were Correlated to Miller indices (024) and (111), respectively, at a time of (3) minutes. This is consistent with Skeleton and Monoclinic (ICDS No. 98-008-5080), the main peaks were detected at diffraction angles of 28.7234° and 32.1311° to correlate with the (004) and (110) crystal planes of CuO respectively at (5) min, and the diffraction peaks at 28.712° and 32.18° to correspond to the (004) and (110) crystal planes of CuO respectively at (7) minutes are in good agreement with the crystal structure of orthorhombic no. (ICSD 98 -008-5080) and monoclinic number (ICSD 98-004-3181), diffraction peaks at angles 28.712° and 31.759° associated with the (004) and (040) crystal planes that correspond to the orthorhombic crystal structure (ICSD 98-008-5080) in a time of 9 minutes, respectively, that were studied on the common peaks, where it was taken for comparison with the rest of the peaks, where all monoclinic and rhombic structures were found, it may be due to the high voltage 16 kV and the high temperature of the solution that led to the appearance of secondary peaks as shown in Table (1).

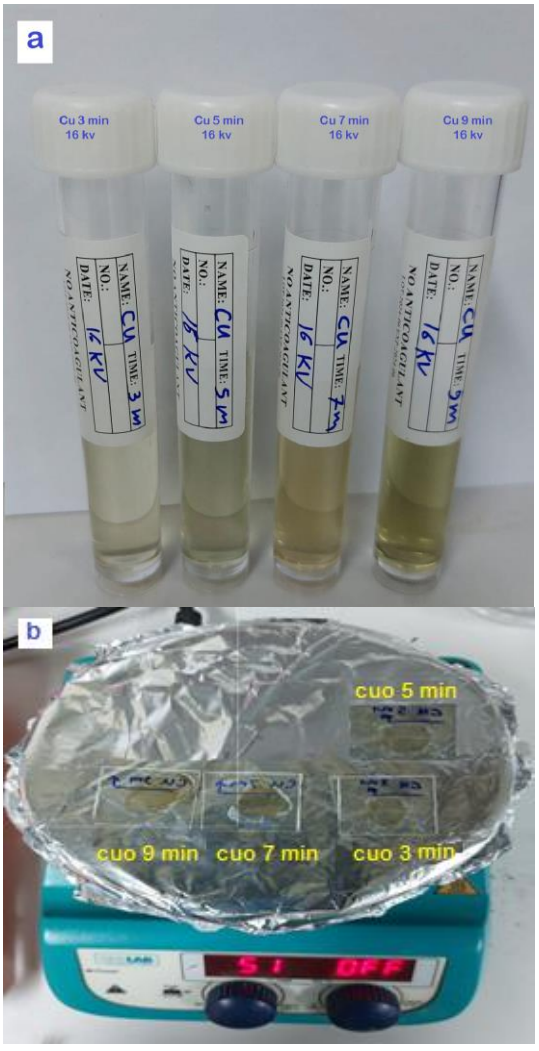

Fig. (2a) The drying of samples for an hour at 51°C, (b) the color change Copper oxide nanostructures solution with different times (3, 5, 7 and 9 min)

As a result, the presence of nanoparticles indicates the formation of pure nanoparticles. Moreover, slight changes in the diffraction pattern of CuO nanocrystals

 ISSN 1813-2065 (print) 2309-1673 (online)

compared with the normal data indicated that the characteristic peaks of CuO had changed. A characteristic line broadening at the diffraction peaks was verified from nm particle generation [15,16], indicating the successful synthesis of CuONPs. The Debye-Scherer formula (1) was used. Calculation of the diameters of CuO nanoparticle crystals [17].

$$D\ (Å) = k\lambda/\beta\cos\theta \qquad (1)$$

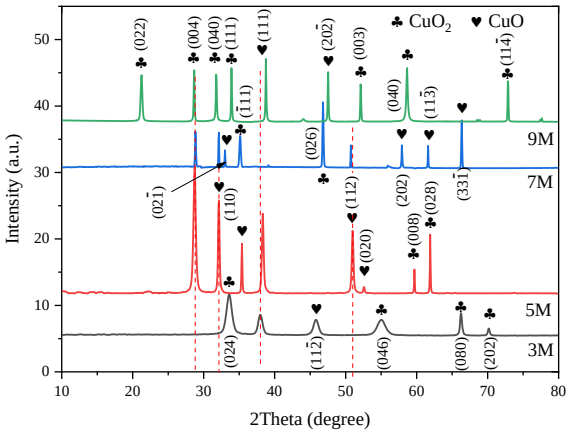

Fig. (3) The XRD patterns of the plasma with atmospheric pressure jet Electrodeposition created in various compositions

Table (1) Results obtained by XRD measurements made on copper oxide with different timings of exposure to plasma jet

No	Time (min)	Std. Pos. (deg)	FWHM Left (deg)	hkl	Crystallite Size (nm)	Chemical formula	Reference code
1	3	32.901 38.295	0.877 0.705	024 111	9.6 12.1	CuO_2 CuO	ICDS 98-008-5080 ICDS 98-004-3181
2	5	28.712 32.18	0.3864 0.2264	004 110	21.7 37.9	CuO_2 CuO	ICDS 98-008-5080 ICDS 98-004-3181
3	7	28.712 32.18	0.152 0.107	004 110	56.9 83.3	CuO_2 CuO	ICSD 98-008-5080 ICSD 98-004-3181
4	9	28.712 31.77	0.12(8) 0.1(1)	004 040	72 78.1	CuO_2 CuO_2	ICSD 98-008-5080 ICSD 98-008-5080

In the formula, D denotes the size of k is the Scherer's constants (k = 0.9) for the crystallite, λ denotes the XRD wavelength (1.540Å), and β denotes the peak's full width at half maximum (FWHM) at the refracting angled from the Bragg's angle location, the result shows that the mean crystallite size of CuO films increases with increase of time.

The optical characteristics of nanoparticles produced by jet plasma were investigated using UV-visible spectroscopy. Copper oxide nanomaterials' UV-visible spectroscopy demonstrate because as the wavelength rises, the absorptivity decreases. This phenomenon is common in many semiconducting substances as well as may be caused by a variety of factors, including internal electric fields inside the crystal and deformation of the lattice. The UV-visible spectra of copper oxide nanoparticles display a blue shift when compared to the bulk, which is attributable to the enhanced quantum confinement effect generated by the nanoparticles' smaller size. The absorption spectra were used to compute the bandgap energy, The TAUC law is utilised to compute the energy bandgap of CuO nanostructures, which is done by computing the band gaps based on the diagrams between (hv)2 and h. (eV) [18].

$$\alpha h\upsilon = K\,(h\upsilon - E_g)^n \qquad (2)$$

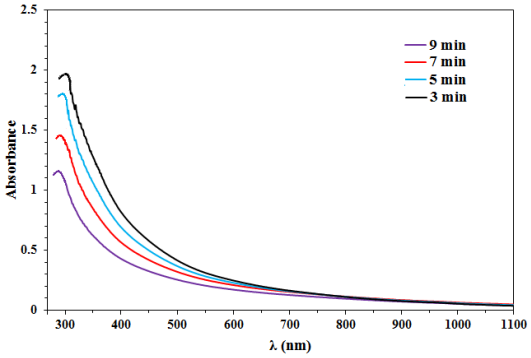

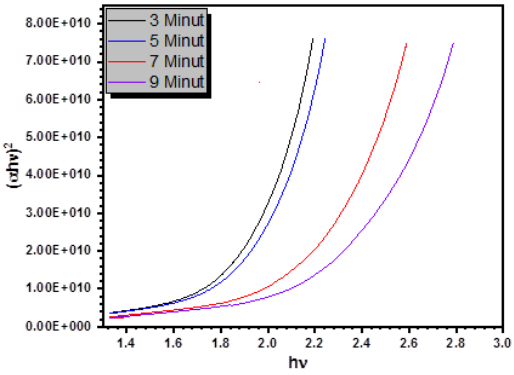

Fig. (4) UV-visible spectra of plasma-jet-synthesized copper oxide nanoparticles

In where, α = absorption rate K= proportionality constant, hυ = incoming photon energy, and E_g = energy band gap , while, n= ½ for indirect the bandgap energy & n=2 for direct band gap, as shown in Table (2). Because of their high surface-to-volume ratio, copper oxide nanoparticles have a high density of surface flaws. The quantum confinement effect causes resulting from the decrease in the dimensional structure and the size of the nanoparticles, where the small size of nanoparticles is responsible for different properties, such as optical, electronic, and electrical [19]. A blue shift in the time (9) minutes in the direct bandgap. It is significant to note that the visible absorption spectra for as-synthesized CuO nanoparticles reduces with time, as shown in (Fig. 4), having a single, high point of absorption at timing (9) min being around 294 mm, which is the typical range for CuO [20]. Many findings in the literature on the production copper oxide nanoparticles using assorted procedures have often brought about a combination

of CuO and Cu_2O nanocrystals [21-23]. In the current condition, the data clearly show the creation of the CuO phase.

Table (2) Results obtained for the energy gap by UV-visible spectra of CuO nanoparticles with nanoparticle size measurements for both concentrations and exposure time by plasma jet

Bombardment time (min)	Energy gap (eV)	Particle size (nm)
3	1.9	59.34
5	2.0	42.19
7	2.2	34.43
9	2.3	18.22

Morphology CuO scanning electron microscopy (FESEM) images were used to examine the nanoparticles generated by the plasma jets. SEM images prove that the manufactured particles are formed in the form of nanoparticles and possess the appropriate nature and shape to be considered nanoparticles as shown in Figure 4, in the image A, the stems are densely covered with copper oxide crystals for (9) minutes, CuO NPs at a timing of (7) minutes in the image B is made by plasma jets that have almost spherical shapes that vary in diameter from a few nanometers to 59.12 nanometers, image C has lumps in some areas and this is due to the presence of an attractive force between them as shown in the figure for timing (5) minutes, where image D shows spherical shapes at a timing of (3) minutes as shown in Table 2. The increase of surface area and surface energy of CuONPs may lead to some oversized grains and agglomeration of Cuo [24]. Nanoparticles agglomerate due to attractive physical forces due to their larger surface area to volume ratio, and they work well as potential gas sensors and other detection uses.

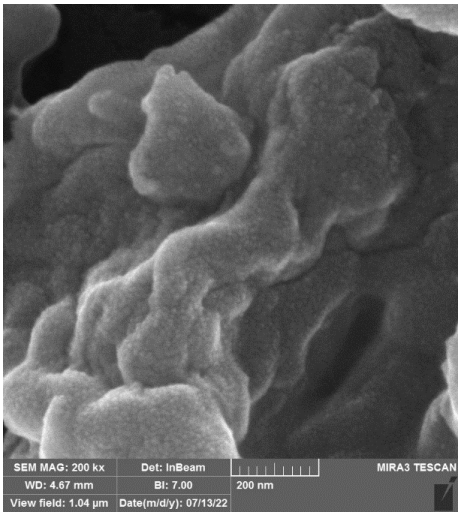

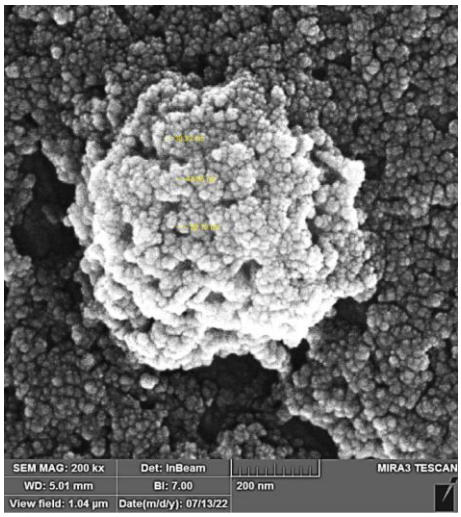

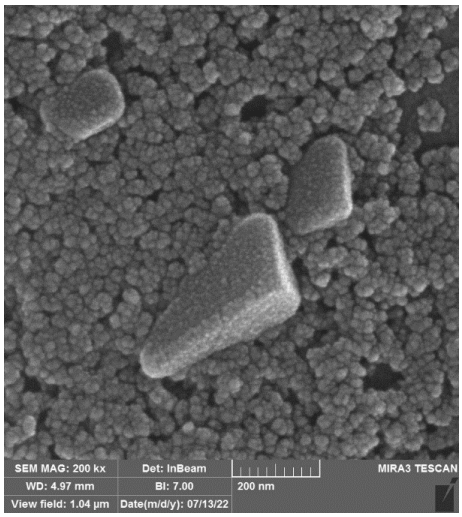

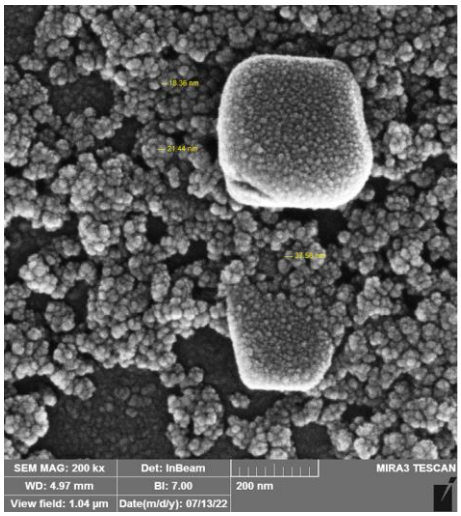

Fig. (5) FESEM images of CuO NPs synthesized by plasma jet technology at different magnifications

 ISSN 1813-2065 (print) 2309-1673 (online)

4. Conclusions

The cold-jet plasma approach was used to create copper oxide nanoparticles in this study. This approach proved the development of copper oxide for durations (3,5,7,9) min, and the absorption peaks at (304, 300, ٢٩٨, 294) nm were revealed accordingly by UV-Vis, indicating the creation of copper oxide. XRD analysis revealed that the produced nanoparticles had an orthogonal and monoclinic crystal structure with typical grain sizes ranging from 18 to 59 nm. The composite particles have a roughly spherical form, according to the SEM picture. This research also shows that copper oxide nanoparticles may be manufactured utilising a variety of ways. Because of its convenience, quickness, cheap cost, and environmental friendliness as compared to other ways, this approach is deemed ecologically benign and practical.

References

[1] D. Nunes et al., "Metal oxide nanostructures for sensor applications", *Semicond. Sci. Technol.*, 34 (2019) 043001.
[2] F. Tochikubo et al., "Chemical reactions in liquid induced by atmospheric-pressure dc glow discharge in contact with liquid", *Japanese J. Appl. Phys.*, 53 (2014) 126201.
[3] W.Z. Wang et al., "Synthesis and Characterization of Cu_2O Nanowires by a Novel Reduction Route", *Adv. Mater.*, 14 (2002) 67-69.
[4] S. Deng et al., "Reduced Graphene Oxide Conjugated Cu_2O Nanowire Mesocrystals for High-Performance NO_2 Gas Sensor", *J. Am. Chem. Soc.*, 134 (2012) 4905-4917.
[5] B. White et al., "Complete CO Oxidation over Cu_2O Nanoparticles Supported on Silica Gel', *Nano Lett.*, 6 (2006) 2095-2098.
[6] J.Y. Kim et al., "Cu_2O Nanocube-Catalyzed Cross-Coupling of Aryl Halides with Phenols via Ullmann Coupling", *Euro. J. Org. Chem.*, 28 (2009) 4219-4223.
[7] W. Zhao et al., "Shape-controlled synthesis of Cu_2O microcrystals by electrochemical method", *Appl. Surf. Sci.*, 256 (2010) 2269-2275.
[8] P.E. de Jongh, D. Vanmaekelbergh and J.J. Kelly, "Cu_2O: a catalyst for the photochemical decomposition of water", *Chem. Commun.*, 12 (1999) 1069-1070.
[9] C.-H. Kuo and M.H. Huang, "Synthesis of Cu_2O Nanocrystals with Systematic Shape Evolution from Cubic to Octahedral Structures", *J. Phys. Chem. C*, 112 (2008) 18355-18360.
[10] M. Sajjad et al., "Structural and optical properties of pure and copper doped zinc oxide nanoparticles", *Results Phys.*, 9 (2018) 1301-1309.
[11] G. Yuan et al., "Shape-Controlled Synthesis of Cuprous Oxide Nanocrystals via the Electrochemical Route with H_2O-Polyol Mix-Solvent and Their Behaviors of Adsorption", *J. Nanosci. Nanotechnol.*, 10 (2010) 5258-5264.
[12] R. Liu et al. "Epitaxial electrodeposition of high-aspect-ratio Cu_2O(110) nanostructures on InP(111)", *Chem. Mater.*, 17 (2005) 725-729.
[13] J. Li et al., "Patterning of Nanostructured Cuprous Oxide by Surfactant-Assisted Electrochemical Deposition", *Cryst. Growth Des.*, 8 (2008) 2652-2659.
[14] H. Bao et al., "Shape-Dependent Reducibility of Cuprous Oxide Nanocrystals", *J. Phys. Chem. C*, 114 (2010) 6676-6680.
[15] P. Mahajan, A. Singh and S. Arya, "Improved performance of solution processed organic solar cells with an additive layer of sol-gel synthesized ZnO/CuO core/shell nanoparticles", *J. Alloys Compd.*, 814 (2020) 152292.
[16] O.A. Fahad and A.S. Mohammed, "Thin films of tungsten oxide based on NH_3 and NO_2 gas sensors", *Materials Today: Proc.*, 42 (2021) 2405–2409.
[17] A.M. Ali, A.S. Mohammed and S.M. Hanfoosh, "The spectral responsivity enhancement for gallium-doped CdO/PS heterojunction for UV detector", *J. Ovonic Res.*, 17(3) (2021) 239-245.
[18] A.S. Mohammed and O.A. Fahad, "Sensitivity enhancement for NO_2 gas sensor based on Alq_3:TiO_2", *AIP Conf. Proc.*, 2372 (2021) 040008.
[19] I.M. Ibrahim, A.S. Mohammed and A. Ramizy, "Energy Band Diagram of NiO:Lu_2O_3/n-Si heterojunction", *Iraqi J. Sci.*, 59(1B) (2018) 287-293.
[20] R. Valls et al., "Linear diterpene with antimitotic activity from the brown alga Bifurcaria bifurcate", *Phytochem.*, 34(6) (1993) 1585-1588.
[21] Y. Abboud et al., "Biosynthesis, characterization and antimicrobial activity of copper oxide nanoparticles (CONPs) produced using brown alga extract (Bifurcaria bifurcata)", *Appl. Nanosci.*, 4(5) (2014) 571-576.
[22] A. Rahman et al., "Synthesis of copper oxide nanoparticles by using Phormidium cyanobacterium", *Indonesian J. Chem.*, 9(3) (2010) 355-360.
[23] M. Yin et al., "Copper oxide nanocrystals", *J. Am. Chem. Soc.*, 127(26) (2005) 9506-9511.
[24] P. Mahajan, A. Singh and S. Arya, "Improved performance of solution processed organic solar cells with an additive layer of sol-gel synthesized ZnO/CuO core/shell nanoparticles", *J. Alloys Compd.*, 814 (2020) 152292.

IRAQI JOURNAL OF APPLIED PHYSICS
Volume 19, Issue 2, April-June 2023, 53-55

Proceedings of the 3rd International Scientific Conference and 5th Scientific Conference, organized by
College of Science, University of Tikrit, Tikrit, Iraq (28-29 December 2022)

Design and Simulation of Rectangular Microstrip Patch Antenna Using a Computer Simulation Technology Operating at 4.5 GHz

Saad N. Ali
Faris S. Atallah
Abdullah H. Muhammad

Department of Physics,
College of Science,
Tikrit University,
Tikrit, IRAQ

The demand for mobile phones with contemporary services like Bluetooth, wireless local area network (WLAN), and interoperability has recently increased. This has led to significant growth in mobile wireless communication system networks for WiMAX microwave access exist everywhere. A model of microstrip antennas for WiMAX/WLAN applications is included in this study. The suggested model was created and analyzed using the 2019 Computer Simulation Tool (CST), which has created and sold high performance 3D electromagnetic simulation tools to simulate electromagnetic fields across all frequency bands. A set of mathematical relationships used to design the micro-band antenna was used to get the design with overall dimensions of 49x41.9 mm^3 to enhance antenna performance and the radiator plate has a rectangular shape. It has a bandwidth suitable for network services, operates at resonant frequencies, has overall dimensions of 23x17.5 mm^3, and has a very low radiation loss of -20.2 dB, making it suitable for WiMAX/WLAN network services. The values of gain, return loss, percentage of stopping voltage, bandwidth, and current distribution were acceptable.

Keywords: Rectangular patch microstrip antenna; VSWR; Return loss; Bandwidth
Received: 3 November 2022; **Revised:** 10 November 2022; **Accepted:** 16 November 2022

1. Introduction

One of the most crucial antenna parts for a variety of microwave and millimeter wave communications applications is now thought to be the tiny microstrip patch antenna. A large number of variants of the modest film receiving wire might be intended to supply Flexible utilitarian ways of behaving to satisfy our diverse needs by altering the layered boundaries and dielectric materials and using multi-facet isolators. RFID, mobile phones, and cordless telephones are a few examples of varied applications. Phones, remote broadband connections using WLAN and WiFi networks, WiMax, GPS trackers, and highlight point connections through mm-wave applications. Another essential aspect of the microstrip antenna is its ability to readily change its specific bandwidth by changing the form, thickness, or use of a multi-layered substrate [1].

There are various possible patch forms for the thin patch antenna, including the rectangular microstrip patch antenna (RMSA) and the oblong patch (CMSA). The only factor that must be considered while constructing a circular patch is its radius; nevertheless, when it comes to the rectangular patch (RMSA), certain layout formulae must be followed. These equations are necessary for the RMSA's design and operation at a specific frequency. The patch antenna and the ground plane are both affected by the electric field produced by the feed line. It is possible to shield the patch antenna once more. Chamber with top and bottom sides that conduct electricity and magnetism. These spurious layers are caused by the fact that the side walls are not a perfect conductor [2] and that the power lines are not exactly perpendicular to the top and bottom layers at the side wall locations. Radiation leaves the cavity due to fields. This type of microstrip patch antenna consists of ground level, a core layer, and patch conductors [3].

One of the downsides of the thin chip antenna is that it has a limited bandwidth; nevertheless, a lot of research has been done recently to increase and improve the bandwidth [4]. One of the downsides of the thin chip antenna is that it has a limited bandwidth; nevertheless, a lot of research has been done recently to increase and improve the bandwidth [4 including using thick substrates with low dielectric constants and metal patch cracks. However, as the length of the feeding line is expanded, thick substrates exhibit limited success because they significantly increase inductance [5].

2. Antenna Design

The design of the patch antenna for the microstrip is based on the "transmission line model" [6]. Here, a rectangular A microstrip antenna of W and h dimensions is spaced longitude apart. The ground level, the insulating substrate, and the mineral patch make up the three layers. Where t is the wavelength of the wave traveling in the vacuum and t is the thickness of the conducting material, the length of the rectangular patch spans from 0.5 to L>0.3333 [7]. Typically, a very small patch is chosen (>>t). The relative dielectric constant, r, of the dielectric material (substrate), is within the range 1.2-2.2, and the dielectric material's height is within the bounds.

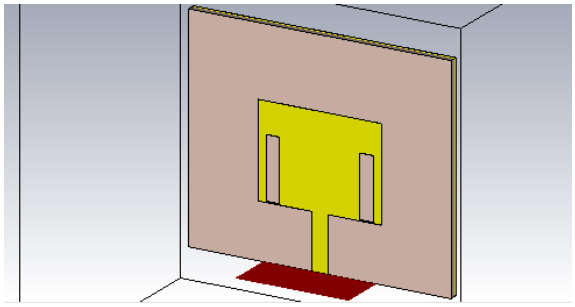

Fig. (1) General structure of the antenna rectangular designer

Table (1) Design parameters of the proposed exact method patch antenna

Parameter	Value
Substrate dielectric constant (ε_r)	4.3
Width of the patch (w_p)	23 mm
Length of the patch (L_p)	17.5 mm
Length of the microstrip line (L_f)	10.5 mm
Width of the microstrip line (W_f)	3.1 mm
Thickness of the microstrip patch (M_t)	0.035 mm
Gap between transmission line and patch (G_{pf})	1
Length of the actual ground (L_g)	41 mm
Width of the actual ground (W_g)	49 mm

Width of the Patch Calculation

The size of the patch affects how well the microstrip antenna performs. This article discusses the equations needed to build a rectangular microstrip patch antenna (RMSA). The calculations below [8] were used to determine the dimensions below for the antenna design.

$$W = \frac{1}{2f_\circ\sqrt{\mu_\circ\varepsilon_\circ}}\sqrt{\frac{2}{\varepsilon_r+1}} = \frac{c}{2f_\circ}\sqrt{\frac{2}{\varepsilon_r+1}} \qquad (1)$$

where c is the velocity of light in free space, f_r is the resonating frequency and ε_r is the dielectric constant of substrate

The actual length of the patch (L) is given by:

$$L = L_{eff} - 2\Delta L = \text{Length Extension } \Delta L \qquad (2)$$

$$\frac{\Delta L}{h} = 0.412\,\frac{(\varepsilon_{reff}+0.3)(\frac{W}{h}+0.264)}{(\varepsilon_{reff}-0.258)(\frac{W}{h}+0.8)} \qquad (3)$$

The length of ground is given by L_g=6h+L, while the width of ground is given by W_g=6h+w.

Stripe line feeding design

Given the impedance characteristics z_0 and the dielectric constant [9], the relationship between the width of the feed line and the thickness of the insulating material, h=1.6, of the insulating layer is given by [9]:

$$Z_\circ = \frac{120\,\pi}{\sqrt{\varepsilon_{reff}}\left(1.393+\frac{W}{h}+\frac{2}{3}\ln\left(\frac{W}{h}+1.444\right)\right)} \qquad (4)$$

where Z is the specific impedance of the antenna, ε_{reff} represents the effective relative dielectric constant of the substrate, h represents the height of the substrate, and W represents the width of the radioactive patch

3. Results and Discussion

Consider some of the fundamental technical features that make the designed antenna unique to create an antenna with good technical characteristics.

A. Return loss

This antenna shows that the return loss is -24.596 dB at the frequency of 1.666 GHz which is shown in the figure, the antenna radiates maximum power.

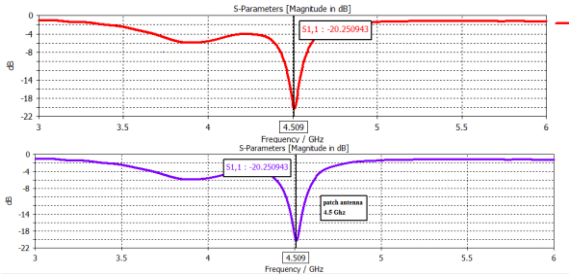

Fig. (2) Return Loss – Rectangular

B. VSWR

Because of the higher power received by the antenna, the value of VSWR is true and positive, and the smaller its value, the better the match between the transmitting line impedance and the antenna impedance. The VSWR's smallest value, one, represents an ideal situation with no reflex power. Most of the supplied power will be radiated from the antenna because the total power received to the antenna (VSWR) for this designed antenna (VSWR) is equal to 1.2 at the frequency (f=4.509 GHz).

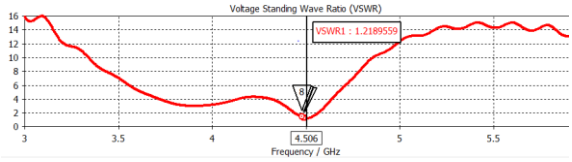

Fig. (3) Standing-Wave Ratio of Voltage

C. Current Distributions

The designed 4.5 GHz microstrip antenna shows surface current distribution and measures 194.126 A/m. Figure (4) displays the electron field strength and movement inside the antenna, as well as the current density scale.

 ISSN 1813-2065 (print) 2309-1673 (online)

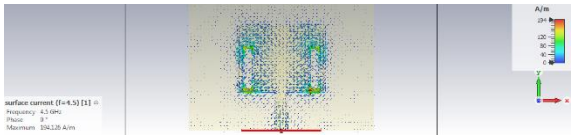

Fig. (4) The patch and the distribution of the current at ground level

D. Far-Field Region

The antenna's angle and far-field radiation are displayed in a 3D far-field pattern. The red far field antenna in the illustration transmits radiation at predetermined angles and with great power. It is pictured as yellow and radiates every week in different directions. It looks blue and has no special abilities. The pattern in the far field is depicted in Fig. (4). The 4.5 GHz antenna emits a maximum radiation of 5.41 dBi.

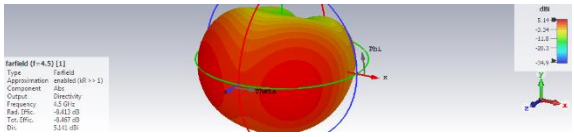

Fig. (5) The far-field diagram of the antenna

Conclusion

This study presents a 4.5GHz tiny rectangular patch antenna internal feeding design processes for WiMAX/WLAN services applications. The distribution of surface currents, stop-wave voltage ratio (VSWR), return loss (S11), and field areas of the radiation patterns was among the important factors that were examined and found to agree with the measurement results. This antenna utilizes the entire 4.5GHz spectrum and is suitable for WiMAX/WLAN applications. The resonant frequency of the proposed antenna is occurred at 4.5 GHz and also stop-wave voltage ratio (VSWR) is 1.2152 which is lower than 2.

References

[1] M. Noureddine, A. Hocini, and T. A. Denidni, "Performance Enhancement of a Compact Patch Antenna Using an Optimized EBG Structure", Chinese J. Phys., 69 (2021) 219-29.

[2] J. Merbin, B. Manoj, and S. Rodrigues, "Design of Slotted Rectangular Microstrip Patch Antenna Operated in ISM Band Using RT-Duroid Substrate", in 2016 Int. Conf. on Electr. Electron. Optim. Techn. (ICEEOT), 3076-80.

[3] M. Karg et al., "Analysis of Rectangular and Triangular Microstrip Antenna Arrays Using HFSS", in 13th Int. Conf. on Electromag. Interf. Compatib. (INCEMIC) (2015), 25-31.

[4] E.A. Alharbi and M.S Alzaidi, "Design and Optimization of Miniaturized Microstrip Patch Antennas Using a Genetic Algorithm", Electronics, 11(14) (2022) 2123.

[5] X. Zhen-Hua et al., "Optimization Design and Development of UHF Antenna for PD Detection in Substation", J. Phys.: Conf. Ser., (2022) 12011.

[6] S. Mbye, D.B. Konditi and P.K. Langat, "A Compact High-Gain Microstrip Patch Antenna with Improved Bandwidth for 5G Applications", IJEER, 10(2) (2022) 196-201.

[7] B.S. Yunusa and S.A. Babale, "Design and Analysis of a Rectangular Microstrip Patch Antenna Using Different Dielectric Materials for Sub-6GHz 5G Applications", Nigerian J. Eng., 28(2) (2021) ???-???.

[8] S. Angana, K. Sarmah and K.K. Sarma, "Low Return Loss Slotted Rectangular Microstrip Patch Antenna at 2.4 GHz", 2nd Int. Conf. on Sig. Process. Integ. Net. (SPIN) (2015), 35-39.

[9] D.F. Moná et al., "Mechanical tension effects on cylinderical truncated-corner microstrip antennas", in 2019 Int. Symp. on Antennas Propag. USNC-URSI Radio Sci. Meeting, 1929-1930.

IRAQI JOURNAL OF APPLIED PHYSICS
Volume 19, Issue 2, April-June 2023, 56-58

Proceedings of the 3rd International Scientific Conference and 5th Scientific Conference, organized by College of Science, University of Tikrit, Tikrit, Iraq (28-29 December 2022)

Asia H. Al-Mashhadani[1]
Awatif S. Jassim[2]
Hammad R. Humud[1]
Munner S. Hamed[2]

[1] *Department of Physics, College of Science, University of Baghdad, Baghdad, IRAQ*
[2] *Department of Physics, College of Science, University of Tikrit, Tikrit, IRAQ*

Effective Treatment Method for Skin Wounds Using Cold Plasma

In this study, the effect of non-thermal plasma and antibiotics (penicillin) on skin wounds was studied. Four groups of rats were used in this study. The first group represented a group of healthy rats for control, and the second group included a group of rats had wounds that were not treated in any way. As for the third group, the wound has treated with cold plasma with different exposure time (2, 4, 6, 8, 10 and 12 min) and the gas flow rate of 2.5 slm. The fourth group was wounded had treated using the antibiotic (penicillin). The results of the research showed that the application of cold plasma to the wounds increases the speed of the wound healing process in shorter times than the normal condition.

Keywords: Cold plasma; Skin wounds; Antibiotics; Biophysics
Received: 22 November 2022; **Revised:** 30 November 2022; **Accepted:** 07 December 2022

1. Introduction

Plasma is defined as the fourth state of material [1]. It is also described as an ionized gas that contains free charge carriers (electrons and ions). Plasma constitutes 99% of the universe [2]. It can also get to know the basis a semi- a neutral gas of electrons, ions, charged particles and neutral atoms, which behave collectively, as these particles generate internal electric and magnetic fields [3]. Irving Langmuir is the first one who called the state of "ionized gas" by plasma. It is a Greek word that originally meant "shapeable substance" or "gel" [4, 5]. The examples of plasma in nature are stars and lightning, as they all exist in a state of plasma (natural plasma) and plasma can be produced in the laboratory (industrial plasma). As well as plasma enters into many fields such as medical and industrial fields [6,7]. Non-thermal plasmas have in recent years revolutionized technology in biomedical applications because they operate at atmospheric pressure and low temperatures as well as not causing thermal damage to nearby objects. Non-thermal plasmas are now used in healthcare to "treat" medical instruments and living tissues. The advantage of non-thermal plasma tissue therapy is non-destructive surgery, high control, and high-precision removal of patient sections. In addition, non-thermal (cold) plasma plays an important role in inhibiting bacteria, which makes it suitable for disinfection of surgical instruments and topical sterilization of tissues [8]. Also this method was used to treat the wound of skin in the diabetics' wounds where the wounds of diabetes people are slow to heal by traditional methods but after applying of cold plasma to the wounds of diabetic rats increases the healing process of the wound at a shorter time than control [9].

2. Experimental Work

In this study, argon gas is used to produce plasma jet system. This system works to produce non-thermal plasma at normal atmospheric pressure and the gas flow range was 2.5 liters/min (constant). As the plasma jet was used to treat the rat's wounds immediately after the wound was completed. The treatment was used twice a day, for four days. After performed the treatment, tissues were taken from the four groups: the control group, the untreated wound group, the wounds group treated with plasma, and the penicillin-treated group for the purpose of microscopic imaging and observation of changes.

3. Results and Discussion

Figures (1-4) show the histological section of the skin of rat with Hematoxylin and eosin stain, with a magnification power of (10X), where figure (1), for first group, figure (2) for the second group, and figure (3) for the third group, which treated wounds using an argon plasma jet with a stable gas flow rate of 2.5 slm with a change in treatment time (2.4,6,8,10 and 12min), and figure (4) for treated wounds using penicillin.

The results showed that the wound healing process is proportional to the cold plasma exposure time as shown in Fig. (3), therefore the exposure for 12 min is the best treatment by cold plasm method, while there are many factors that affect the delay or non-healing of wounds, including the presence of antibiotic-resistant bacteria that affect the body's ability to heal wounds naturally. This specialist relies on modern plasma technology to help patients suffering from this disease, as it has been shown, that

plasma consisting of ionized particles can kill all types of bacteria, especially antibiotic resistance.

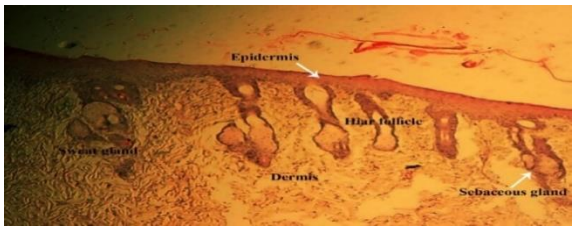

Fig. (1) A histological section of the skin of a healthy rat with Hematoxylin and eosin stain

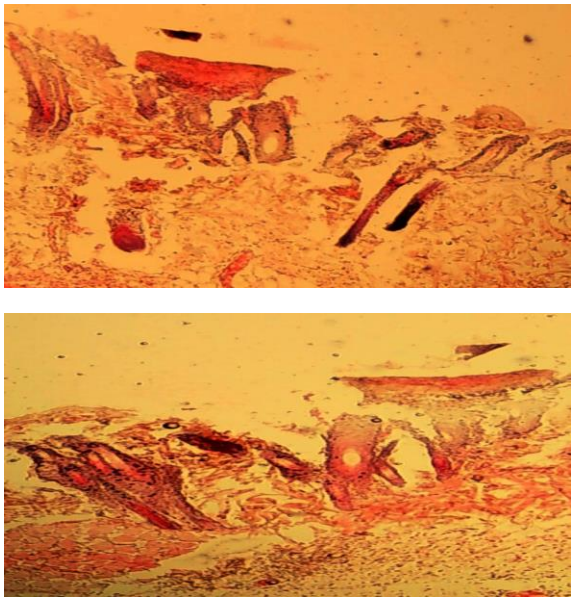

Fig. (2) Histological sections of damaged and untreated rat skin stained with hematoxylin-eosin

The results also showed that treatment of wounds with cold plasma is better than treatment with penicillin. The bacteria became resistant to penicillin [10] and convert the effective antibiotic into a weakly effective form and have no effect on the bacteria. Bacteria acquire resistance through their ability to perform several mechanisms that help them resists.

It was found that the gas temperature (the temperature of the flame of the plasma jet) increases with the increase of the gas flow exposure time. It was found the temperature of plasma jet devise equal to room temperature were recorded and begin to rise gradually with the increase the exposure time to gas flow, as it is clear from the gas temperature that the system can be used to treat burns and wounds on the surface of the skin without causing any harm or adverse results.

This method represents hope for people with wounds, which may be caused by damage to blood vessels in the event of diabetes. Or the damage caused by the failure of the immune system in people with cancer, or even the slowdown in cell division in the elderly.

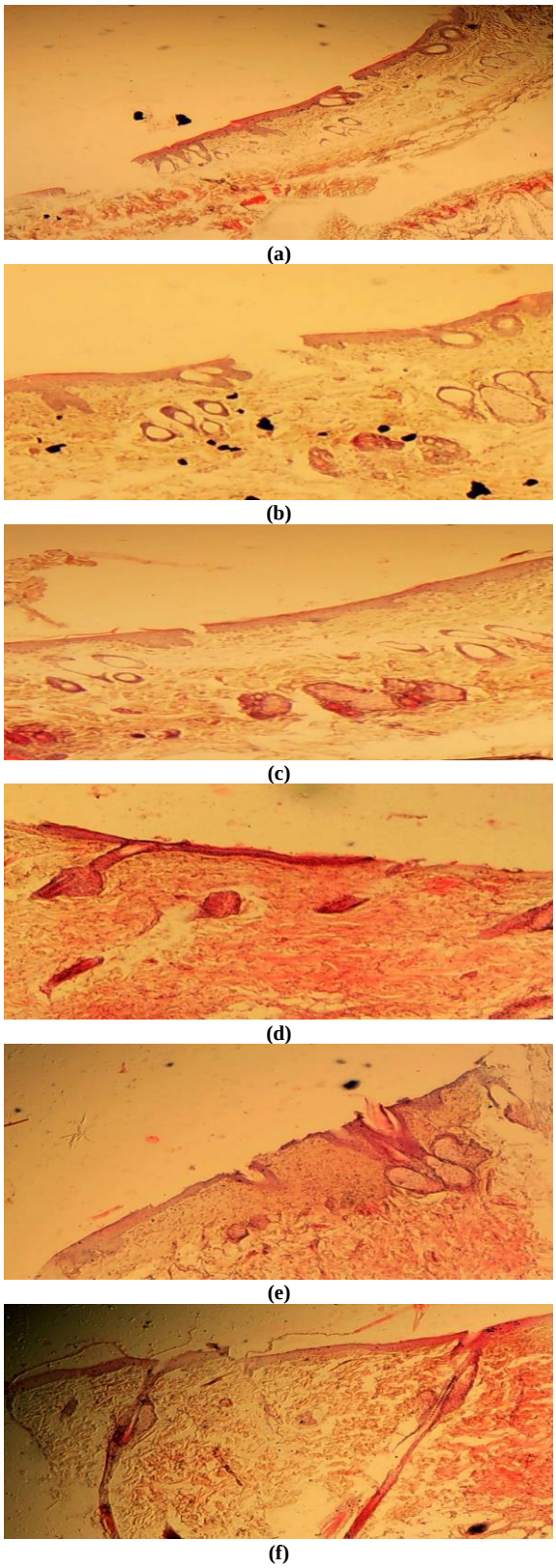

(a) **(b)** **(c)** **(d)** **(e)** **(f)**

Fig. (3) Effect of cold plasma exposure time with constant gas flow rate of 2.5 slm on treated skin wounds of rats stained with hematoxylin-eosin dye: (a) 2 min, (b) 4 min, (c) 6 min, (d) 8 min, (e) 10 min and (f) 12 min

Perhaps the most important characteristic of the plasma treatment technique is the possibility of treating intractable wounds that are difficult to treat with ointments. The reason for this, the plasma is in a

 ISSN 1813-2065 (print) 2309-1673 (online)

gaseous state, and thus it can reach much smaller areas than the areas that reach with liquids and ointments, for example, that is, we can enter areas too small for bacteria to settle in.

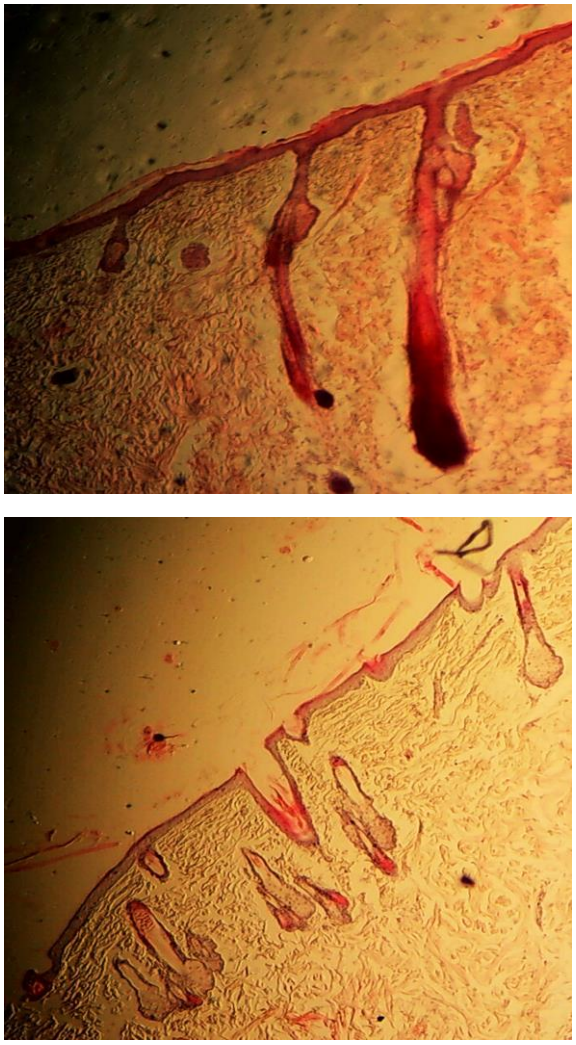

Fig. (4) Tissue sections of rat skin treated with penicillin

4. Conclusions

The results showed that the application of "cold" plasma to the wounds increases the wound healing process in shorter times than the normal condition. Cold plasma has the ability to coagulate blood directly. In this research, the wound was exposed to cold plasma immediately after conducted wound, and it has observed occularly and histologically. It explained that the recovery time depends on the increase in the used dose which means that the longer the treatment exposure time, the faster the recovery. In wound treatment, plasma showed rapid susceptibility compared to penicillin.

References

[1] V. Arora, V. Nikhi, N.K. Suri and P. Arora, Cold Atmospheric Plasma (CAP) in Dentistry, Dentistry, vol.4, 189, (2014).
[2] Jan.van. Dijk, Plasma technology prospects for biomedical applications, Eindhoven University of Technology Department of Applied Physics, CAUSA symposium, (2012)
[3] R. Dams, Plasma deposition of conjugated polymers at atmospheric pressure, Ph.D. thesis, Hasselt University, Material Center (2007).
[4] R. J. Goldston and P. H. Rutherford, "Introduction to plasma physics", Princeton pub. Institute of physics publishing, pp.1–3 (1995).
[5] R. Fitzpatrick, "Plasma Physics" University of Texas at Austin, Education, vol. 221, pp.1–210 (2006).
[6] E. P. van der Laan, E.Stoffels, and M. Steinbuch, Development of a smart positioning sensor for the plasma needle, Institute of Physics Publishing, vol. 15, p 582, 2006
[7] R. E. J. Sladek, Plasma needle non-thermal atmospheric plasmas in dentistry, Ph.D. thesis Technische Universiteit Eindhoven, Netherlands Organization for Scientific Research (NWO). (2006)
[8]I. Efieft, Plasma needle: exploring biomedical applications of Non– thermal plasmas. Technische Universiteit Eindhoven, 2005.
[9] A.S. Jassim et al., "The cold plasma effect on the speed of recovery of a skin wound in diabetics", AIP Conf. Proc., 2372 (2021) 130010.
[10] E. B. Robert, Heggers, P. J. and Davis, J. G., "Efficacy of Silver- Coated Dressing as Bacterial Barriers in A Rodent Burn Sepsis Model". Wounds J., **11**(4), 64-71, 1999.

IRAQI JOURNAL OF APPLIED PHYSICS
EDITORIAL BOARD

COPYRIGHT RELEASE FORM
IRAQI JOURNAL OF APPLIED PHYSICS (IJAP)

We, the undersigned, the author/authors of the article titled

……
……
……
……
……
……
……

that is submitted to the Iraqi Journal of Applied Physics (IJAP) for publication, declare that we have neither taken part or full text from any published work by others, nor presented or published it elsewhere in any other journal. We also declare transferring copyrights and conduct of this article to the Iraqi Journal of Applied Physics (IJAP) after accepting it for publication.

The authors will keep the following rights:

1. Possession of the article such as patent rights.
2. Free of charge use of the article or part of it in any future work by the authors such as books and lecture notes after informing IJAP editorial board.
3. Republishing the article for any personal purposes of the authors after taking journal permission.

To be signed by all authors:

Signature:……..date: ……
Printed name: ……

Signature:……..date: ……
Printed name: ……

Signature:……..date: ……
Printed name: ……

Correspondence author:……..……...……...
……
Address:……..……
……
Telephone:……..……..email: ……

Note: Complete and sign this form and mail it to the below address with your finally revised manuscript

The Iraqi Journal of Applied Physics
P. O. Box 88052, Baghdad 12631, IRAQ
www.iraqiphysicsjournal.com
Email: info@iraqiphysicsjournal.com
Email: editor_ijap@yahoo.co.uk
Email: ijap.editor@gmail.com

IRAQI JOURNAL OF APPLIED PHYSICS

Volume (19) Issue (2) April-June 2023

CONTENTS